UCLouvain

epl

École polytechnique de Louvain

Increasing HCCI power density through thermal stratification

Impact of water direct injection

Authors: **Thomas Collette, Anthony Gatin**
Supervisor: **Hervé Jeanmart**
Readers: **Tony Arts, Francesco Contino, Maxime Pochet**
Academic year 2018–2019
Master [120] in Electro-mechanical Engineering

Abstract

In the path towards a 100% renewable electricity production, long-term storage is needed to match the energy production and consumption. Power-to-Fuel is one of the most promising systems able to accomplish this role. To restitute electricity from various fuels, the *Homogeneous Charge Compression Ignition* engine is an interesting candidate.

HCCI combustion is a Low Temperature Combustion mode which enables low nitrogen oxides and particulate matter emissions while at the same time showing Diesel-like efficiencies. However, the very high pressure rise rates associated with HCCI combustion imposes the use of lean mixtures. This is why these types of engines are characterized by a relatively low power density.

For HCCI engines to reach viability at global scale, it is crucial to increase their power density. In this thesis is explored a technique which could allow to burn richer mixtures and therefore produce more mechanical work : Water Direct Injection. The local evaporation of a water spray, by creating thermal gradients inside the cylinder, could allow to stagger the combustion, hence reducing the pressure rise rate. The objectives of this work can be divided in two steps.

The first step of this thesis has been to design and calibrate a reliable injection system. After the mounting of the injection system onto the HCCI monocylinder test bench of the UCLouvain, the second step of this work has been carried out. This step consists in realizing the experiments on the engine test bench.

Even if Water Direct Injection still needs further investigations, this technique has shown very encouraging results. Indeed, the fuel-air equivalence ratio could be increased from 0.2 to 0.5, leading to a 215% boost of the power density.

Acknowledgements

First of all, we would like to sincerely thank our supervisors, Prof. Hervé Jeanmart and Maxime Pochet for their continuous guidance throughout the year. None of this work would have been possible without their availability and their patience.

We also would like to thank Prof. Tony Arts and Prof. Francesco Contino for kindly accepting the role of readers and becoming part of the jury.

We would like to express our most sincere gratitude to the iMMC technical staff and especially to Lily, Arnaud, Axel, Frank, Julien, Luc and Thierry for their adaptability towards our numerous requests.

Finally, we would like to thank our family and friends for their continuous support throughout the realization of this thesis.

Contents

Nomenclature

Abbreviations

BDC	Bottom dead center
BMEP	Brake mean effective pressure
CA05	Crank angle where 5% of the combustion heat has been released
CA10	Crank angle where 10% of the combustion heat has been released
CA50	Crank angle where 50% of the combustion heat has been released
CA90	Crank angle where 90% of the combustion heat has been released
$CA_{75\text{-}05}$	Combustion duration, = CA75 - CA05
$CA_{90\text{-}10}$	Combustion duration, = CA90 - CA10
CAD	Crank angle degree
CI	Compression ignition
CR	Compression ratio
ECU	Electronic control unit
EGR	Exhaust gas recirculation
EVC	Exhaust valve closing
EVO	Exhaust valve opening
EXMEP	Exhaust losses mean effective pressure
FMEP	Friction mean effective pressure
FPGA	Field programmable gate array
FTM	Fast thermal management
FuelMEP	Fuel mean effective pressure
HCCI	Homogeneous charge compression ignition
HRR	Heat release rate
HTMEP	Heat transfer losses mean effective pressure

ICE	Internal combustion engine
$IMEP_g$	Gross indicated mean effective pressure
$IMEP_n$	Net indicated mean effective pressure
IVC	Intake valve closing
IVO	Intake valve opening
LHV	Lower heating value
LTC	Low temperature combustion
MBF	Mass burn fraction
MEP	Mean effective pressure
MFC	Mass flow controller
MPRR	Maximum pressure rise rate
NOx	Nitrogen oxide
P&ID	Piping and instrumentation diagram
PLIF	Planar laser-induced fluorescence
PM	Particulate matter
PMEP	Pumping mean effective pressure
PRR	Pressure rise rate
PWM	Pulse width modulation
QMEP	Released heat mean effective pressure
RE	Renewable energy
SCR	Selective catalyst reduction
SI	Spark ignition
SOI	Start of injection
TDC	Top dead center
TW	Thermal width
UHC	Unburned hydrocarbons
VCR	Variable compression ratio
VVA	Variable valve actuation
WDI	Water direct injection

Symbols

c_p	Constant pressure specific heat
c_v	Constant volume specific heat
h	Convective heat coefficient
L	Connecting rod length
m_a	Air mass
m_f	Fuel mass
m_{H2O}	Injected mass of water
p_{in}	Intake pressure
p_{out}	Exhaust pressure
Q_{gross}	Heat released by combustion
Q_{loss}	Heat transfer losses
Q_{net}	Net heat release
R	Universal gas constant
r	Crank radius
S_p	Piston speed
T_1	Pick-up time
T_2	Holding time
T_{in}	Intake temperature
V_d	Displacement volume
ΔH_{compr}	Variation of the mixture enthalpy during compression phase
ΔH_{vap}	Water enthalpy of vaporization
Δp	Injection pressure
η_b	Brake efficiency
η_{comb}	Combustion efficiency
η_{mec}	Mechanical efficiency
η_{th}	Theoritical efficiency
η_{ti}	Thermodynamic efficiency
γ	Heat capacity ratio, $= C_p/C_v$

ω	Angular speed
ϕ	Equivalence ratio
τ	Compression ratio
θ	Crank angle
θ_{SOE}	Crank angle of end of injection
θ_{SOI}	Crank angle of start of injection

Introduction

In the context of limiting global warming and decontaminating the air that we breathe, Internal Combustion (IC) engines manufacturers tend to reduce fuel consumption and pollutants emissions. The *Homogeneous Charge Compression Ignition* (HCCI) engine is an interesting candidate for this purpose. A homogeneous mixture, as in Spark Ignition (SI) engines, is compressed to the point of auto-ignition, as in Compression Ignition (CI) engines. HCCI combines the advantages of these two technologies : the high efficiency of the CI engine, and the low NOx and soot emissions of the SI engine.

HCCI combustion process being totally driven by chemical kinetics, it has no means of direct ignition control. Unlike SI engines which involve spark plugs and CI engines which operate on the basis of fuel injection timing, combustion timing control in HCCI engines is a major concern because of its spontaneity. However, many techniques are being developed to overcome this, such as variable compression ratio, variable valve timing, hot exhaust gas recirculation (EGR) and intake mixture heating.

On the other hand, as all the fuel ignites at the same time in HCCI engines without any flame propagation, the combustion is very fast. Therefore, working with a high equivalence ratio would imply dangerously high pressure rise rates. This limitation on the fuel proportion leads to a low power density. Several solutions like turbocharging and EGR have been investigated at the UCLouvain in previous research works, but in the frame of this master thesis, an innovating technique is considered : thermal stratification by Water Direct Injection (WDI). The local vaporization of a water spray would have the effect of creating a temperature gradient in the cylinder and accordingly reducing the simultaneity of the combustion, while maintaining the mixture composition homogeneity that enables low pollutants levels.

To carry out this task, a WDI system has been designed, calibrated and mounted into the cylinder head of the UCLouvain monocylinder HCCI test bench. It was then possible to realize the experiments which could allow to evaluate the thermal stratification effects on power density.

The first chapter of this master thesis presents how HCCI engines can play a key role in the energy transition. The idea behind thermal stratification is also detailed. In the second chapter, the experimental setup and the design of the WDI system are described. The third chapter details the results of the injector calibration. Finally, the results of the experiments on the engine are discussed in the fourth chapter. The influence of several injection parameters and intake conditions are analyzed, with the aim of validating the effect of water direct injection on the power density of HCCI engines.

Chapter 1

General context

This chapter is divided in three sections. The first presents the HCCI engine and the role it could play in the context of the energy transition, especially in the "Power to Fuel to Power" process. Then, the challenges linked with HCCI combustion are detailed, as well as the already existing techniques used to mitigate them. Finally, the notion of thermal stratification is explained, and the objectives of this work are presented. Throughout this chapter, the necessary concepts have been introduced when needed.

1.1 HCCI advantages in the frame of energy transition

In the purpose of facing the challenge of global warming, carbon-based energy sources are progressively being replaced by renewable sources. This change in the state of the energy system is commonly referred as energy transition. The production of electricity will thus be more and more dependant on uncontrolled parameters such as the weather, and therefore will not match the real-time consumption. In this context, the need for energy storage is essential to avoid blackouts and to ensure a continuous supply. A large range of storing energy systems exists, going from batteries for short-term applications, to "Power to Fuel" for long-term applications. This solution ensures a high volumetric density but implies a low efficiency, as shown in Figure 1.1.

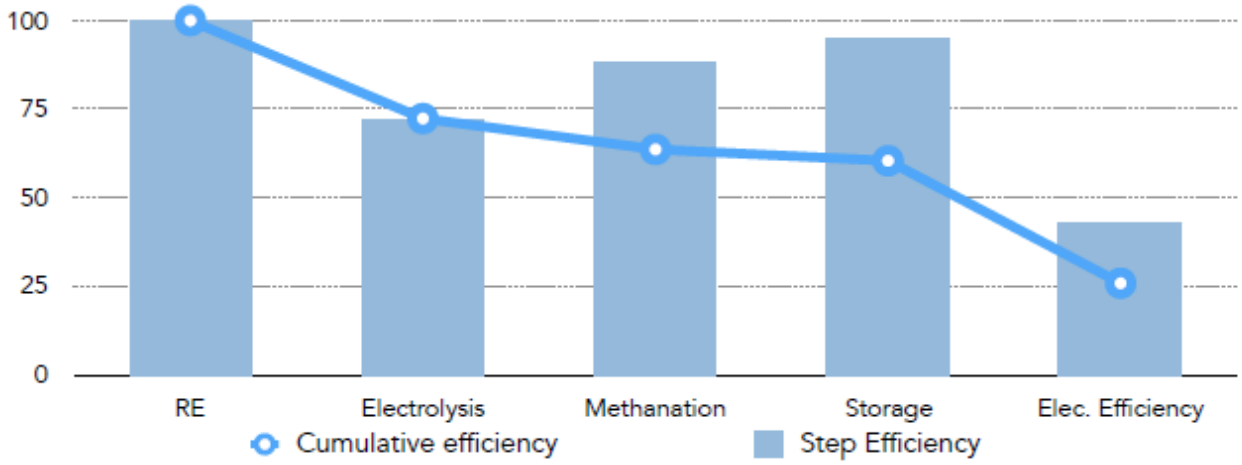

FIGURE 1.1: Efficiencies of the "Power to Fuel to Power" process. Case of methane [1].

This picture indicates the successive efficiencies of each phase of the "Power to Fuel to Power" process. It starts from the renewable energy production (RE) to the restitution of electricity after storage. It is shown that the major conversion losses happen during the restitution phase, i.e. in the IC engine. After electrolysis, hydrogen can either be used as such, or used as a reagent in chemical processes to obtain various gaseous fuels like ammonia, methane or methanol. The following approach is to focus on the weakest link of the chain. The classical IC engine able to work with gaseous fuels is the SI engine. By replacing it by a HCCI engine, the global efficiency is improved and the restored amount of energy becomes larger. One can also observe that the need for a multifuel engine is legitimate. The HCCI engine meets this criteria. Among the advantages that will be discussed below, namely the high efficiency and low pollutants emissions, this benefit is clearly non-negligible.

The HCCI engine

In HCCI engines, for *Homogeneous Charge Compression Ignition* engines, the combustion is characterized by the auto-ignition of a homogeneous mixture of fuel and air. HCCI engines therefore combine the features of SI engines and CI engines. Indeed, in SI engines, the homogeneous fuel-air mixture is compressed and its ignition happens at a predetermined position thanks to a spark plug. On the other hand, in CI engines, air is compressed to high temperatures and the injection of fuel leads to the spontaneous auto-ignition of the non-homogeneous charge (see Figure 1.2). Hence, HCCI engines indeed combine working principles of SI and CI engines.

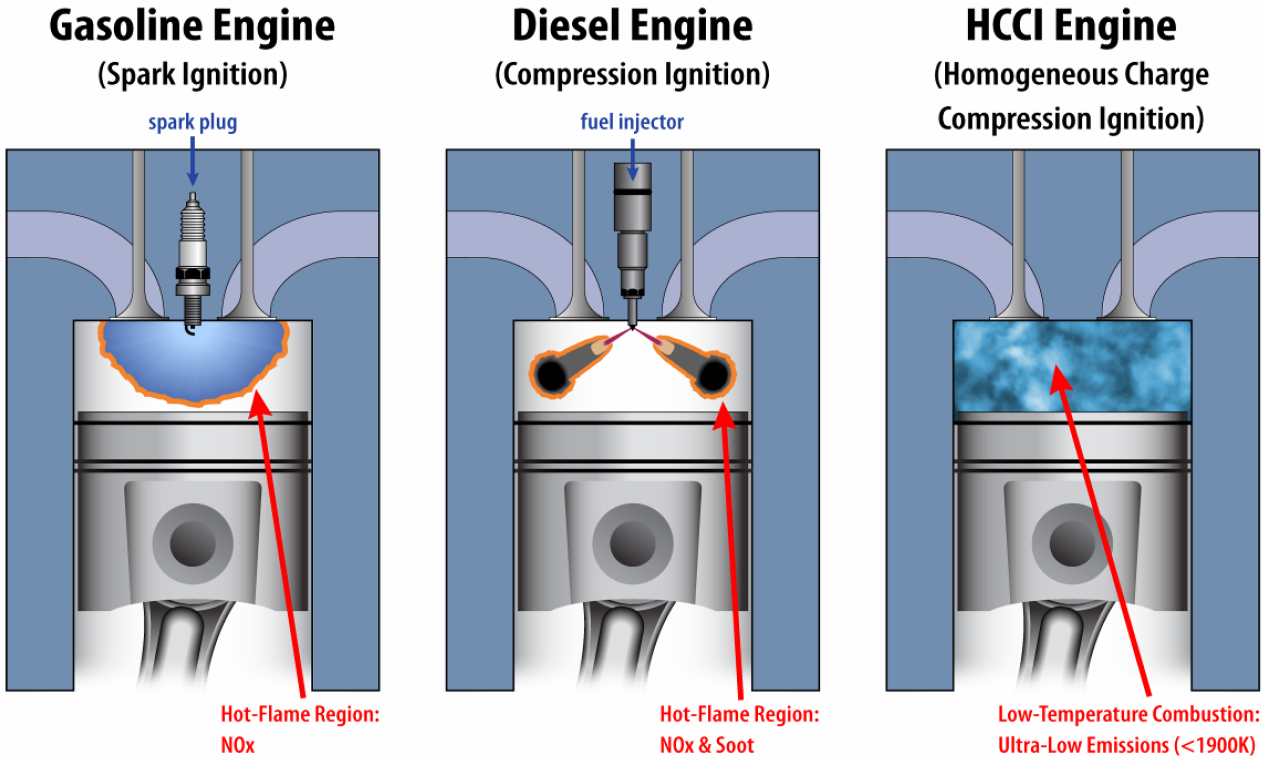

FIGURE 1.2: Comparison between SI, CI and HCCI engines. [1]

[1] http://csyoo.unist.ac.kr/research/hcci-combustion/

HCCI combustion is probably the Low Temperature Combustion (LTC) mode which accomplishes the best trade-off between SI and CI : the low Nitrogen Oxides (NOx) and soot emissions of SI engines and the low fuel consumption and CO_2 emissions of CI engines. This is why HCCI engines generate increasing interest in the context of the energy transition.

The short summary on HCCI combustion presented here is inspired by the Master thesis of Boveroux and Gramme [2].

HCCI combustion starts when the auto-ignition conditions are fulfilled. A combustion phasing occurring when the piston is around top dead center (TDC) is desired, since it is the position where the highest mechanical work can be extracted. As pressure, temperature and charge composition are relatively uniform in the cylinder, these auto-ignition conditions are reached at many points simultaneously. This results in a fast pressure increase whereas in SI and CI engines, combustion speed is limited by flame propagation and diffusion, respectively. One of the main challenges in HCCI engines is therefore the control of the start and the rate of combustion. Here, no spark plug nor fuel injector can trigger the combustion. Chemical-kinetics is what governs HCCI combustion. Several parameters influence the kinetics, such as charge temperature and pressure, the type of fuel used, fuel concentration, cylinder wall temperature, etc. Temperature is the most critical parameter, as stated by the Swedish scientist Svante Arrhenius.

1.1.1 High efficiency

As mentioned before, the HCCI high efficiency is mainly due to the high compression ratio (CR) needed to auto-ignite the mixture by reaching its temperature of self-ignition. The theoretical efficiency of an engine, which is defined as the ratio between the work performed on the piston and the heat released during the combustion, is linked to the compression ratio by the following expression [3] :

$$\eta_{th} = 1 - \frac{1}{\tau^{\gamma-1}} \tag{1.1}$$

where γ is the ratio of the specific heats c_p/c_v. As γ value is typically around 1.4, an increase in compression ratio will lead to an increase in efficiency, as depicted in Figure 1.3.

HCCI engines reaching diesel-like efficiencies, in the order of $40-45\%$, stems from the compression ignition mechanism. As a comparison, gasoline engines usually have a $30-35\%$ efficiency. A high thermal efficiency means a lower fuel consumption and therefore, lower CO_2 emissions.

1.1.2 Low pollutants emissions

The exhaust gases of HCCI engines contain ultra low levels of pollutants. NOx and particulate matter (PM) are the main polluting gases under consideration. This section describes their formation mechanisms and how the HCCI functioning principle allows insignificant emissions.

NOx are responsible of acid rains and are at the origin of the formation of ground-level ozone. While the stratospheric ozone layer protects the Earth from ultraviolet radiation, ground-level ozone participates in global warming. It absorbs infrared radiations and act as a greenhouse

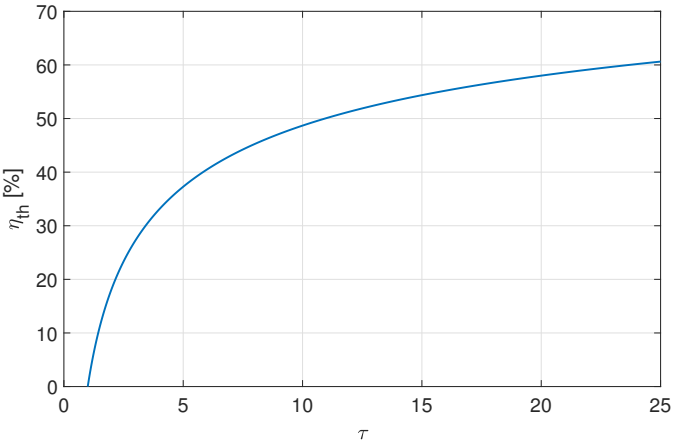

FIGURE 1.3: Influence of the compression ratio on the theoretical efficiency.

gas. Moreover, NOx and ozone are the major components of Smog, which has a harmful impact on human health.

Soot, often referred as PM, is considered carcinogenic by the International Agency for Research on Cancer. These particulates are the most lethal form of air pollution due to their ability to penetrate deeply into the respiratory and cardiovascular systems. A strong exposure to these pollutants can lead to heart attacks and lung cancers. Black Carbon, one of the soot constituents, also plays a role in climate change since it has a significant radiative-forcing effect.

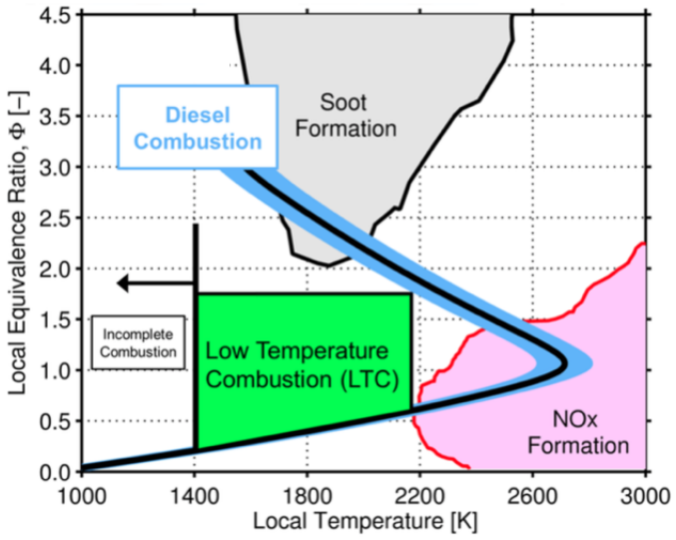

FIGURE 1.4: Regions of NOx and soot formation in a ϕ-T diagram. [2]

The diagram in Figure 1.4 represents the local in-cylinder conditions where NOx and soot formation rates are high. These regions were obtained by Kitamura *et al.* [5], based on chemical simulations of n-heptane at a pressure of 60 bar and a 2 ms injection duration. NOx are formed when temperatures reach at least 1800-1900 K and when there is enough oxygen available. This physically happens at the periphery of the diffusion flames in CI engines, as shown by the

[2] Adapted from [4]

green line in Figure 1.5. For SI engines, the combustion mode is a premixed flame, with the functioning points typically situated at the extreme right of the blue curve of Figure 1.4. This means that in both SI and CI engines, NOx formation rates are high. However, in SI engines, emissions fall to near zero after treatment by the three-way catalyst, which is not the case in diesel engines because of the abundance of O_2. Indeed, in these conditions, the performances of the catalytic converter are lowered. Three-way catalysts require that the engine is operated at nearly stoechiometric conditions. Therefore, in CI engines, another technique is used to convert NOx, the Selective Catalyst Reduction (SCR). These types of converters face several limitations and NOx emissions in CI engines remain non-negligible even after treatment.

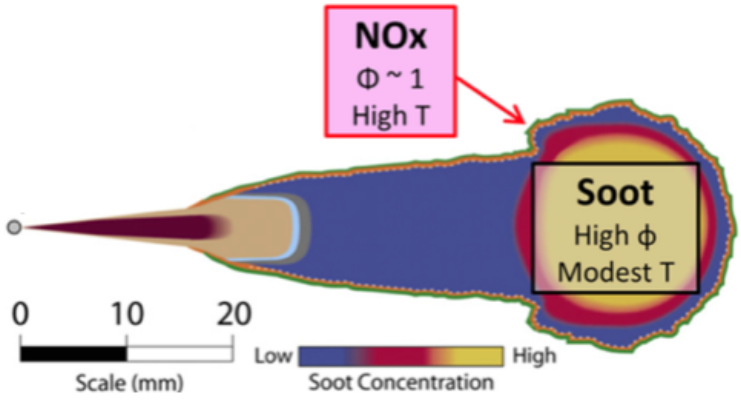

FIGURE 1.5: Conceptual model of a reacting diesel spray. [3]

Soot is formed in locally rich regions, i.e. where fuel is in excess. The equivalence ratio (or fuel-air equivalence ratio) ϕ is defined as the ratio between the real fuel-to-air ratio, and the fuel-to-air ratio leading to a stoichiometric combustion :

$$\phi = \frac{m_f/m_a}{(m_f/m_a)_{st}} \tag{1.2}$$

A fuel-air mixture is said rich when $\phi > 1$ and lean when $\phi < 1$. In SI engines, there is no production of soot since the charge is homogeneous and stoichiometric. In diesel engines however, fuel injection leads to a non-uniform composition of the mixture throughout the cylinder. In the core of the jet (see Figure 1.5), local equivalence ratios reach high values and soot emissions are formed. It can be noted that the majority of the PM production happens during the early phase of the combustion, called the ignition delay period, and that PM can be oxidized afterwards if temperature is sufficient. This is why the temperature range of soot formation is a bit narrow in Figure 1.4.

HCCI engines use homogeneous and very diluted mixtures, so the peak temperature stays low and none of these conditions are met. NOx and soot emissions are therefore insignificant.

[3] Adapted from [4]

1.2 HCCI limitations and ways to overcome them

HCCI engines also present drawbacks which need to be solved for future large-scale deployment. First the mixture combustion might be incomplete. Low temperature combustion modes such as HCCI can quench near the cylinder walls, resulting in unburned hydrocarbons (UHC) and CO emissions. Indeed, the cylinder temperatures being typically between 1400 K and 1900 K, CO may not have been oxidized in CO2. The residual intrinsic enthalpy of carbon monoxide and the unburned hydrocarbons is thus lost and the combustion efficiency decreases to approximately 95 % whereas it reaches values close to 100 % in CI engines. However, it has to be noted that these partial combustion products can be removed with oxidation catalysts used in gasoline and diesel engines [6]. Therefore this does not consist in a strict barrier to the global deployment of HCCI engines, but only in a pure loss of efficiency. Other challenges linked with HCCI combustion appear and are more crucial, namely the control of the ignition timing and the limitation on power density.

1.2.1 Combustion timing control

Arising from the nature of HCCI combustion, there is no direct control of the start and rate of the heat release. Indeed, to trigger the combustion, gasoline engines use a spark plug and diesel engines rely on fuel injection timing. In HCCI engines, the initiation and the rate of combustion are only driven by the thermodynamic state of the charge and by the chemical kinetics.

If the combustion occurs too early during the compression stroke of the cycle, cylinder temperature and pressure will reach excessive values, resulting in NOx emissions and in severe cases, destructive effects to the engine. If the combustion starts too late, it might be quenched during the expansion stroke resulting in probable misfires and increased fuel consumption, and UHC and CO emissions. The engine could also enter a vicious circle with one misfire and the following cycle being characterized by a very high Heat Release Rate due to the fuel-rich residuals, followed by another misfire (because the mixture becomes poor) and so on. There is thus a crank angle window where the combustion has to happen [7]. The challenge of the combustion control in HCCI engines makes their use in the automotive industry quite premature. When the engine speed and load are subject to permanent changes, it becomes very challenging to regulate in real time all the parameters that influence combustion kinetics to keep the optimum auto-ignition timing. Different strategies can be used to help control the combustion timing: variable valve actuation (VVA), variable compression ratio (VCR), exhaust gas recirculation (EGR), fast thermal management (FTM) and fuel modification. All of these techniques have been explored by researchers but their feasibility can differ.

VVA consists in modulating the inlet valve opening (IVO) and the exhaust valve closing (EVC) to modify the amount of residual gas trapped inside the cylinder and the effective compression ratio. These parameters both have a strong influence on combustion timing. VVA being already operated in gasoline engines, it is one of the major candidates for large-scale production.

VCR also shows a potential in combustion control. Indeed, decreasing the compression ratio will delay the auto-ignition and increasing it enables to maintain the maximum brake torque for lower intake temperatures. So in the path towards multifuel engines, it makes sense to consider the VCR approach.

EGR is also a currently existing technology in production engines which has several effects on the combustion, leading to changes in efficiency and emissions. When used at high levels at the intake, hot EGR will tend to advance the combustion timing while cold EGR retards it due to the higher heat capacities of the recirculated gases [8].

FTM is an advanced version of intake temperature control developed by Haraldsson *et al.* [9]. Indeed, intake air heating can be used to adjust auto-ignition timing, but its practical implementation is difficult because of the thermal inertia of the heating element. In FTM, a hot source and a cold source are used and the temperature of the mixed airflow is regulated with throttle valves.

Finally, fuel composition can be diversified to act on the auto-ignition conditions of the charge. The most common solution is to use a fuel with a low ignition temperature and another with a high ignition temperature. By dynamically varying the ratio of each fuel in the blend, it is possible to control the combustion timing over a wide range of conditions. [7]

However, in the frame of this thesis, combustion timing control relative to variations of engine rpm is not the main challenge under consideration. Indeed, the HCCI engine of the Stevin laboratory is connected to a three-phase generator which is set at a constant speed of 1500 RPM. A PID controller allows to maintain a constant engine rpm by applying a brake torque to the engine shaft.

1.2.2 Low power density

When one speak about the operating range or load limits of an engine, it refers to the different values of IMEP or BMEP that the engine can reach as a function of its engine speed. Here the influence of engine speed will not be studied since the experimental HCCI engine is stationary, but its power output range is of great interest.
Before proceeding with the restrictions linked with the operation of an HCCI engine, a brief reminder might be useful to correctly manipulate the typical physical quantities relating to IC engines.

Definition of the MEP and efficiencies

In order to be able to discuss the performances of an engine regardless of its size, the amount of energy present at each step is normalized by the displacement volume of the engine. These ratios are called Mean Effective Pressures (MEP) and are expressed in bars. In Figure 1.6 are depicted the successive MEPs and associated efficiencies.
First, the internal chemical energy of the fuel is computed from its Lower Heating Value (LHV) and the consumed fuel mass per engine cycle, m_f. By dividing by the displacement volume V_d,

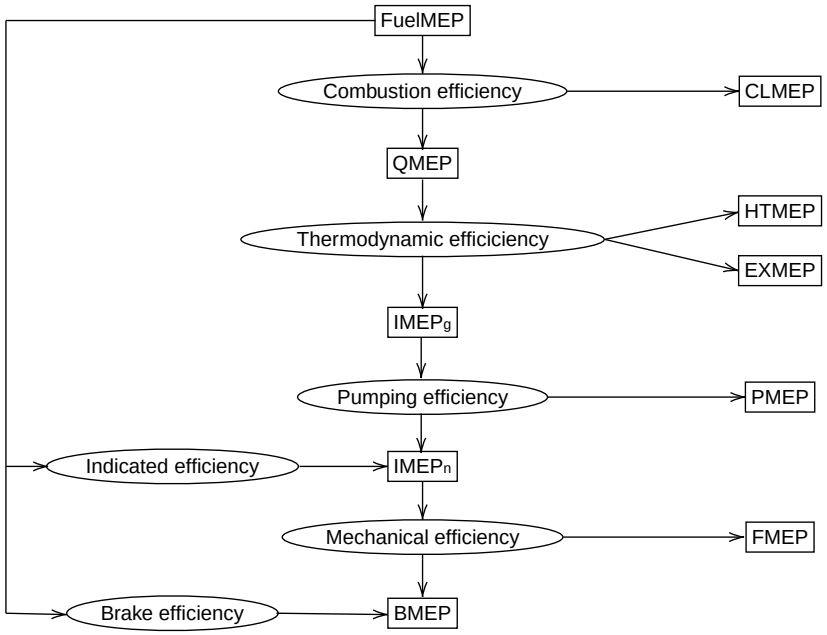

FIGURE 1.6: Energy conversion diagram of the engine cycle.

one obtains the expression of FuelMEP :

$$\text{FuelMEP} = \frac{m_f \cdot \text{LHV}}{V_d} \tag{1.3}$$

The effective value of the heat released by the combustion, normalized by V_d, is defined as QMEP. The combustion efficiency η_{comb} is thus the ratio between QMEP and FuelMEP.

IMEP_g (Indicated MEP gross) is the internal work on the piston and is the result of the conversion of the heat input QMEP by the power cycle. Heat losses occurring during the cycle can be divided in two parts. Wall losses by heat transfer, HTMEP, and exhaust losses, EXMEP, are thus deduced from QMEP to obtain IMEP_g. The thermodynamic efficiency, η_{ti}, characterizes this transformation :

$$\eta_{ti} = \frac{\text{IMEP}_\text{g}}{\text{QMEP}} = 1 - \frac{\text{HTMEP}}{\text{QMEP}} - \frac{\text{EXMEP}}{\text{QMEP}} \tag{1.4}$$

At this point, the breathing phase of the cycle has to be taken into account. Head losses during the intake stroke and a pressure increase during the exhaust represent a certain work consumption. This is the pumping work and can be expressed as follows:

$$W_p = (p_{out} - p_{in}) \cdot V_d = \text{PMEP} \cdot V_d \tag{1.5}$$

where p_{out} and p_{in} are the mean cylinder pressures during the exhaust and intake strokes, respectively. The net work on the piston during the whole cycle is thus the difference between IMEP_g and the pumping work PMEP :

$$\mathrm{IMEP_n} = \mathrm{IMEP_g} - \mathrm{PMEP} = \frac{\oint p \cdot dV}{V_d} \tag{1.6}$$

For the HCCI engine under consideration, pumping losses are very low. Indeed, due to the absence of a throttle valve, there is no significant pressure drop at the intake. The theoretical efficiency mentioned in section 1.2.1 can be viewed as the ratio between $\mathrm{IMEP_n}$ and QMEP. In the particular case of the ideal Otto cycle, it reduced to $\eta_{th} = 1 - \frac{1}{\tau^x}$. In reality, deducing the successive losses will be the followed approach rather than computing this efficiency, since the losses can be derived from measured data.
The last step is to consider the mechanical friction losses FMEP (Friction MEP). The mechanical work available at the crankshaft, called the brake work, BMEP, is then obtained and the mechanical efficiency η_{mec} can be computed :

$$\eta_{mec} = \frac{\mathrm{BMEP}}{\mathrm{IMEP_n}} = 1 - \frac{\mathrm{FMEP}}{\mathrm{IMEP_n}} \tag{1.7}$$

Finally, the brake efficiency η_b describes the global conversion of the fuel energy content to useful work :

$$\eta_b = \frac{\mathrm{BMEP}}{\mathrm{FuelMEP}} \tag{1.8}$$

HCCI load limits

At low load, HCCI combustion can become unstable because auto-ignition of very lean mixtures is difficult. The chance of misfires increases and large cycle-to-cycle variations of the output torque can happen. The high load limit is characterized by the maximum pressure rise rate (MPRR) associated with the combustion. As it can be seen in Figure 1.2, classical IC engines burn their fuel gradually, resulting in a smooth rate of heat release and a low pressure rise rate. In HCCI engines, all the fuel is burning at the same time which leads to a dangerously fast pressure increase as shown in Figure 1.7. In order to avoid damages to the engine, a lean mixture is imperatively used and the power density is therefore very limited.

When the equivalence ratio of the charge is increased, the pressure rise rate could exceed acceptable limits and pressure oscillations may appear. This phenomenon is called *ringing* and is quite similar to *knocking* in SI engines. These pressure waves are perceived as a loud combustion noise by human ear, but also subject the engine to high mechanical stresses, which can end up with destructive effects. MPRR values leading to the usual ringing limit typically lie between 10 and 20 bars/CAD.

The ringing correlation developed by Eng [11] quantifies the knock intensity :

$$RI \approx \frac{1}{2\gamma} \cdot \frac{(\Delta p)^2}{p_{max}} \cdot \sqrt{\gamma R T_{max}} \tag{1.9}$$

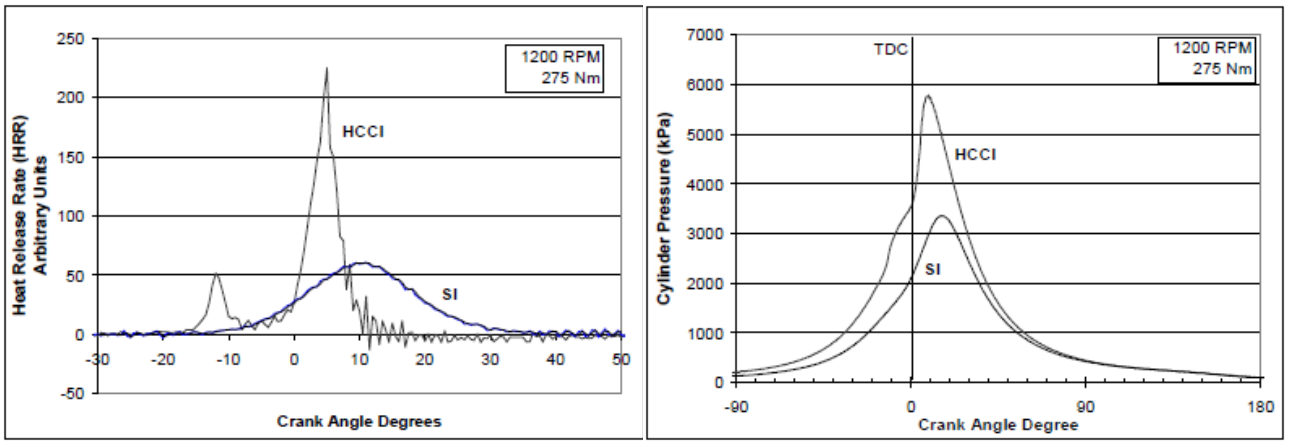

(A) Heat Release Rate. (B) Cylinder Pressure.

FIGURE 1.7: Comparison of Heat Release Rate and in-cylinder pressure of HCCI and SI engines under the same brake torque and same rotation speed. [10]

where $\sqrt{\gamma RT_{max}}$ is the local speed of sound, and Δp is the amplitude of the pressure oscillations happening between 8 and 25 kHz. The ringing intensity is expressed in MW/m^2. Best practice recommends to keep it below 5 MW/m^2.

To enhance HCCI power density, that is, to reach higher values of IMEP, the fueling rate has to be increased. One of the possibilities to achieve this goal would be to use different fuels in order to introduce different auto-ignition timings and thus, a longer combustion. Another way would be to reduce the temperature rise during the compression with EGR, causing a delay in the auto-ignition and a damping of the combustion process. Or finally, by thermally stratifying the charge, the combustion duration can be strongly extended, allowing to reach much lower pressure rise rates. This is what will be investigated in this work.

1.3 Thermal stratification for reducing HCCI pressure rise rates

Combustion chemistry is a complicated network of reactions. The start and the progression of combustion depends on the balance between chain-branching and chain-terminating reactions. As the reactive radicals population increases, reactions accelerate and these two phenomena combine to lead to an explosive rise in radical concentration, reaction rates, and system pressure. These oxidation reactions release heat, and their rates themselves depend on the temperature and the pressure. Combustion kinetics can therefore be seen as an open loop with a self-accelerating behaviour. Based on this chemical kinetics model, the pressure rise related to the combustion of a thermally uniform charge of fuel and air would result in an excessively harsh operation.

However, in reality, combustion is not as instantaneous as expected. In recent years, the community gained a deeper understanding of HCCI heat release thanks to optical chemiluminescence and planar laser-induced fluorescence (PLIF) imaging. In Figure 1.8 are represented two-dimensional temperature maps obtained with PLIF imaging. The successive images show

the temperature distribution of the bulk gas at the mid plane between the cylinder head and TDC, as the piston is moving upwards to TDC. The colors indicate the deviation of the bulk gas temperature relative to the mean temperature for each piston position.

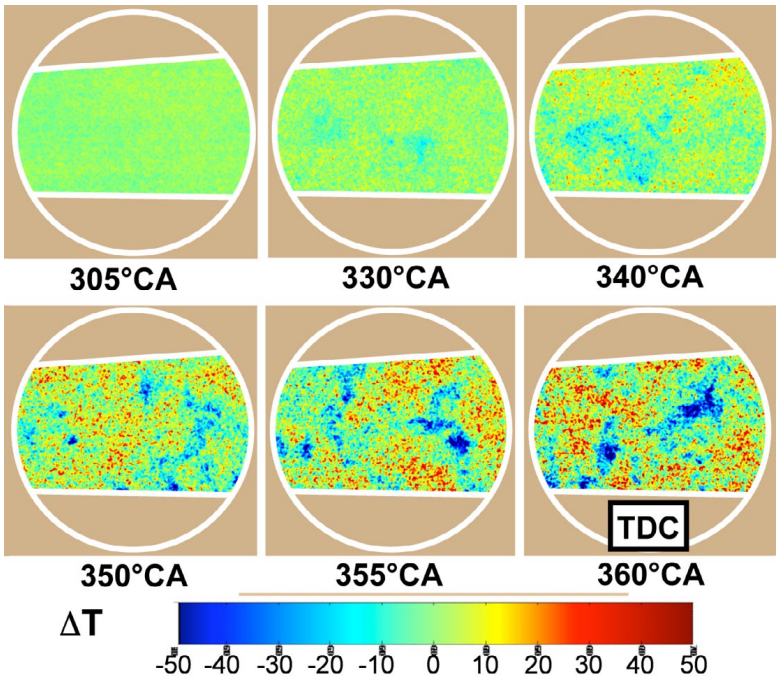

FIGURE 1.8: PLIF thermometry images for various piston positions. [4]

Initially, the temperature distribution of the charge is nearly homogeneous, but it can be observed that in the late part of the compression stroke, some thermal non-uniformities appear. The temperature difference between the hot regions and the colder pockets will widen during the remainder of the compression. Starting from a given thermal width at BDC (i.e. the difference between the maximum and minimum temperature of the charge at BDC), the evolution can be characterized by the following equation :

$$\mathrm{TW}_{\mathrm{tdc}} = \mathrm{TW}_{\mathrm{bdc}} \cdot \tau^{\gamma-1} \tag{1.10}$$

where γ is the average ratio of the charge specific heats during compression. It therefore depends on the compression ratio, CR, and the type of charge dilution, i.e. fresh air or EGR [12].

This naturally occurring thermal stratification stems from several sources such as incomplete fuel/air mixing, incomplete mixing of the fresh charge and the burnt gases from the previous cycle resulting in hot residuals pockets, turbulent flow during the induction stroke and heat transfer from the charge to the cylinder walls during compression. Thermal stratification can play a key role in the aim of achieving reasonable rates of heat release, and consequently reducing the global pressure rise rate associated with HCCI combustion.

At this point it is necessary to introduce the relationship between the rate at which heat is released during the combustion and the cylinder pressure evolution. The following reasoning

[4] https://crf.sandia.gov/characterizing-the-development-of-thermal-stratification-in-hcci-engines/

therefore applies for a closed system, that is, between IVC and EVO. The crank angle differential form of the First Law of Thermodynamics can be written as [13]:

$$nC_v \frac{dT}{d\theta} = \frac{dQ}{d\theta} - p\frac{dV}{d\theta} \tag{1.11}$$

The ideal gas relation, $pV = nRT$, in its differential form, is expressed as:

$$nR\frac{dT}{d\theta} = p\frac{dV}{d\theta} + V\frac{dp}{d\theta} \tag{1.12}$$

Substituting Eq. (1.12) in Eq. (1.11) gives :

$$\frac{dQ}{d\theta} = \frac{\gamma}{\gamma - 1} \cdot p \cdot \frac{dV}{d\theta} + \frac{1}{\gamma - 1} \cdot V \cdot \frac{dp}{d\theta} \tag{1.13}$$

The variable Q here refers to the heat that is actually available for the bulk gas, it is by now denominated as Q_{net}. The heat released by the combustion of the fuel, Q_{gross}, is thus :

$$Q_{gross} = Q_{net} + Q_{loss} \tag{1.14}$$

where Q_{loss} represents the heat losses to the cylinder walls in the form of convective heat transfer. The total heat released by combustion is finally expressed as :

$$\frac{dQ_{gross}}{d\theta} = \frac{\gamma}{\gamma - 1} \cdot p \cdot \frac{dV}{d\theta} + \frac{1}{\gamma - 1} \cdot V \cdot \frac{dp}{d\theta} + \frac{dQ_{loss}}{d\theta} \tag{1.15}$$

This formulation allows to analyze HCCI combustion based on measurable data, such as gas pressure and volume, and wall temperature. The heat release evolution, $Q_{gross}(\theta)$, is the result of integration of Eq. (1.15) over a crank angle window where combustion happens. A typical heat release rate profile (HRR or RoHR for rate of heat release) and its cumulative form are shown in Figure 1.9.

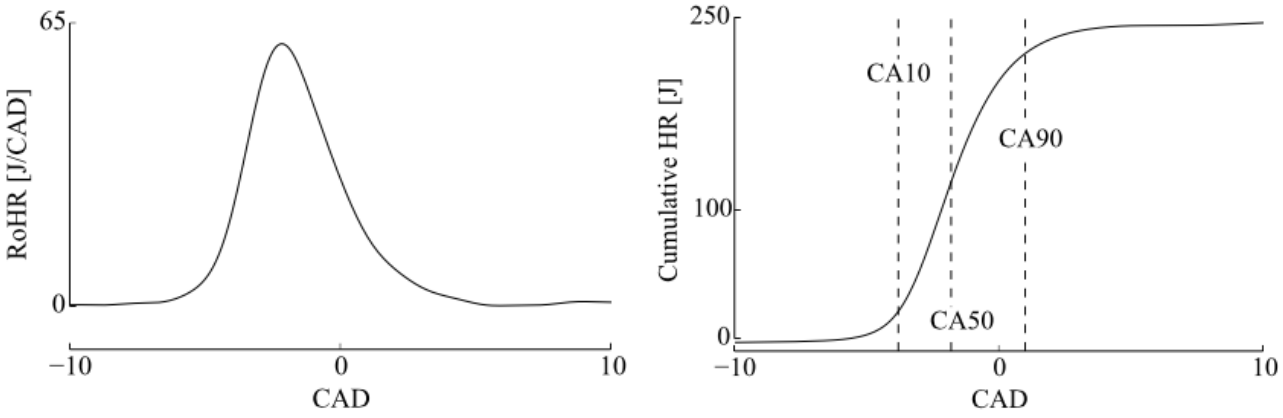

FIGURE 1.9: Typical HCCI HRR and $Q_{gross}(\theta)$ profiles [13].

The commonly used parameters such as CA10, CA50 and CA90 correspond to the crank angle positions where 10, 50 and 90% of fuel has been burned. To evaluate the combustion duration, the reference parameter is the difference between CA90 and CA10, called CA_{90-10}. These tools will be extensively used to discuss the experimental results of this work, in Chapter 3.

Eq. (1.15) highlights that in order to control the pressure rise rate, combustion duration has to be extended. Based on this idea and the remarkable results of Figure 1.8, researchers of the Sandia National Laboratories developed a multi-zone version of the CHEMKIN-III kinetics-rate code to study the effects of in-cylinder thermal stratification [14] [15]. Basically, the single-zone version of the code models a thermally uniform charge, while the five-zone version (used to obtain the following figures) models the thermal stratification of the charge.

Previous experiments show that burn duration increases rapidly with combustion retard. This combustion retard is controlled by adjusting intake temperature : when the initial temperature of the charge is decreased, auto-ignition points are reached later.

Figure 1.10 confirms these results with the 5-zone model, that is, for a thermally stratified charge. The thermal width of the charge at BDC, TW_{bdc}, was set at 20 K to match the experimental pressure curves of the engine. The stair-step appearance of the curves is the result of representing a continuous thermal distribution with only 5 zones. As the mean intake temperature is decreased, the PRR is lowered. Indeed, the chain reaction of burning regions that causes the subsequent autoignition of the cooler zones is delayed by the chamber expansion.

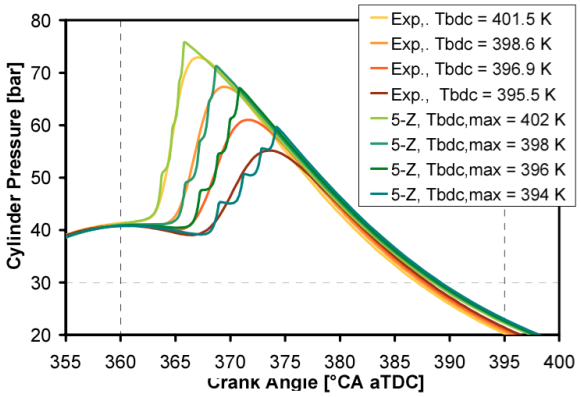

FIGURE 1.10: Combustion phasing sweeps for the experiments and the model. $\phi = 0.367$. $TW_{bdc} = 20$ K for the 5-zone model [12].

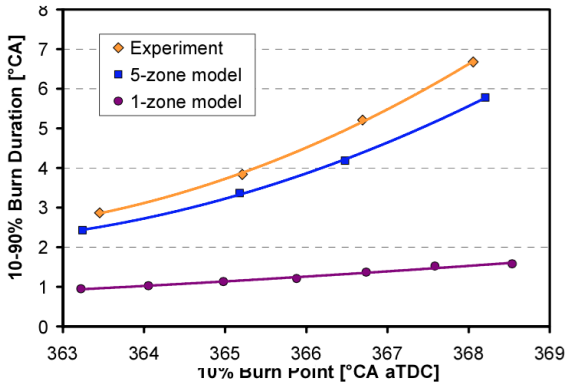

FIGURE 1.11: Influence of combustion phasing on combustion duration. $\phi = 0.367$. $TW_{bdc} = 20$ K for the 5-zone model [12].

For a theoretical homogeneous thermal distribution, the single-zone model (i.e. the purple curve) in Figure 1.11 demonstrates that the slowing due to the combustion retard is weak. Indeed, for a thermally homogeneous charge, the PRR is governed by the chemical-kinetics alone. Thermal stratification amplifies the benefit on the PRR of a given combustion retard, as shown by the five-zone model and the experimental curve, with a natural thermal stratification. The sensitivity of the pressure rise rate to changes of thermal stratification is depicted in Figure 1.12.

As the charge is stratified, several zones at different temperatures are present. Therefore in each zone, the kinetic rates are different. In this case, the global PRR is driven by the thermal width

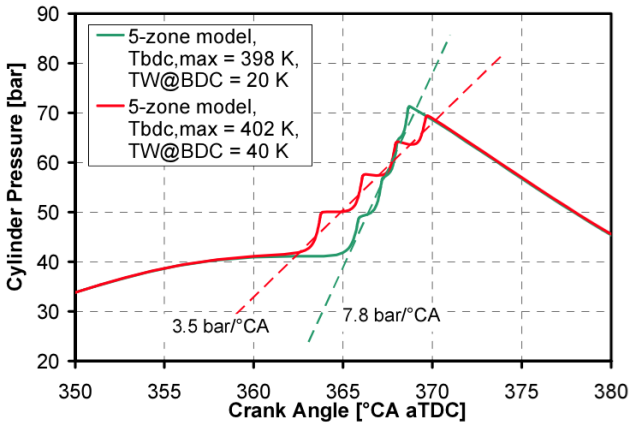

FIGURE 1.12: Influence of the thermal width on the pressure rise rate for $\phi = 0.367$ [12].

rather than the kinetic rates which dominates within a single zone.

Thermal stratification can thus be seen as a phenomenon that enables to slow down HCCI combustion without shifting too much the start of combustion, therefore without losing control.

1.3.1 Direct injection for thermal stratification

It could be possible to enhance the naturally occurring thermal stratification by forcing convective heat transfer. Modifying the piston head to create a higher air swirl is a feasible solution, but the cooling effect mainly happens in the boundary layer near the cylinder walls, while stratification in the core of the charge has a greater impact.

Most of the techniques employed in LTC modes that try to provide control on the start and the rate of heat release are based on a direct fuel injection event to introduce a stratification of equivalence ratio and chemical reactivity [16].

These approaches have shown successful results but the principle of HCCI combustion is kind of given away. Indeed, the intentional fuel-air mixture stratification presents a risk of higher soot emissions due to the locally rich regions (as shown in Figure 1.4).

The goal is therefore to create thermal gradients inside the cylinder without altering fuel-air homogeneity. Direct injection of water is a novel technique which potentially complies these requirements. Latent heat of vaporization of the spray could affect the mean temperature of the charge, which offers control on the start of combustion, while at the same time forming a wider temperature distribution, which slows down the combustion rate.

Figure 1.13 shows the expected effect of thermal stratification obtained through WDI on combustion duration. Increasing the equivalence ratio results in higher rates of heat release, leading to higher total values of Q_{gross}. Water injection then slows down the heat release and decreases the associated PRR, therefore allowing richer mixtures and higher power densities. Nonetheless, it has to be noted that Figure 1.13 represents fictive HRR curves, and that combustion retard is not taken into account.

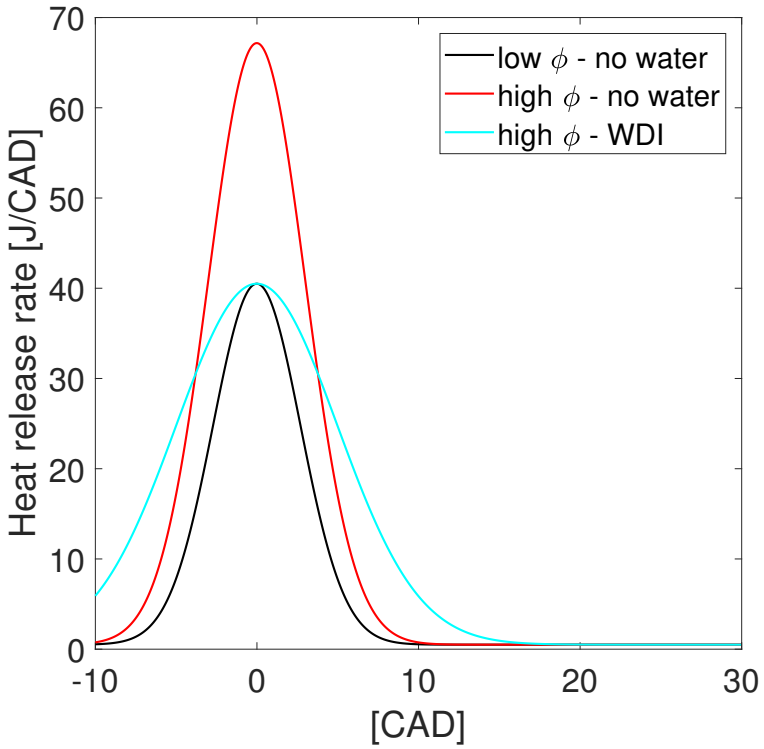

FIGURE 1.13: Qualitative representation of the effect of thermal stratification on the HRR.

Throughout this work, the aim will be to slow down the heat release without involving too much combustion retard. Combustion phasing near TDC is optimal since it provides maximum thermodynamic work and is less sensitive to fluctuations of the charge temperature. The injection parameters that will be studied are injection pressure, water mass and injection timing. These results will be displayed in Chapter 3.

Chapter 2

Experimental setup

To achieve the goal of this thesis, i.e. to study the impact of WDI on the engine, two main tasks have been accomplished : the calibration of the injector and the experimental tests on the engine. This chapter is therefore divided in two main sections. The first one details the calibration setup and methodology, while the second section is focused on the HCCI test bench and its modifications. An additional section recalls the methodology used to compute the heat release.

2.1 Calibration test bench

This section describes the approach followed to perform the calibration of the injector and the different elements of the calibration setup. The goal here is to measure with a sufficient accuracy the water mass per injection for different opening times and injection pressures, before mounting the injector in the cylinder head. Indeed, once the injector is coupled with the engine, there is no more access to the information of the injected mass. Furthermore, as mentioned below, a gasoline injector was used to spray water. Therefore, no theoretical model corresponds to the experiments of this thesis.

2.1.1 Water injector

The injector used in the following experiments is a classical solenoid-operated gasoline direct injector sold by Bosch Motorsport, see Figure 2.1a. To spray liquids in the combustion chamber, a high current is needed in order to generate a strong magnetic field needed to open the injector in a brief time. This magnetic field generated by the current flowing in the coil lifts the valve needle, and therefore allows the highly pressurized fuel to reach the combustion chamber. When the current is switched off, the spring pushes the needle back and thus stops the flow of fuel. A cross-sectional view of the injector is depicted in Figure 2.1b.

The energizing current must follow a precise pattern, shown in Figure 2.2. First, a high voltage is applied to the coil to generate a high current slope needed to quickly reach high current values. This is called the boost phase. Then, during the pick-up phase, the needle is totally pulled. Finally, a small "holding" current is flowing to keep the injector open.

As mentioned above, this injector was designed to spray gasoline and not water, therefore the major concern was about premature wear of the injection valve. Indeed, the difference in

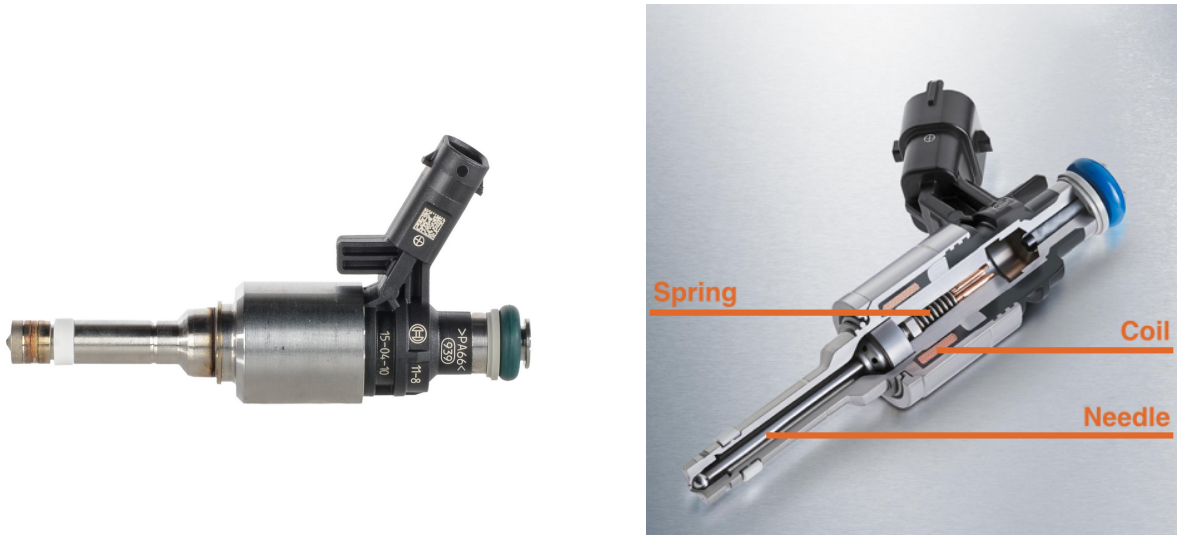

(A) (B)

FIGURE 2.1: Bosch HP Injection Valve HDEV 5.2.

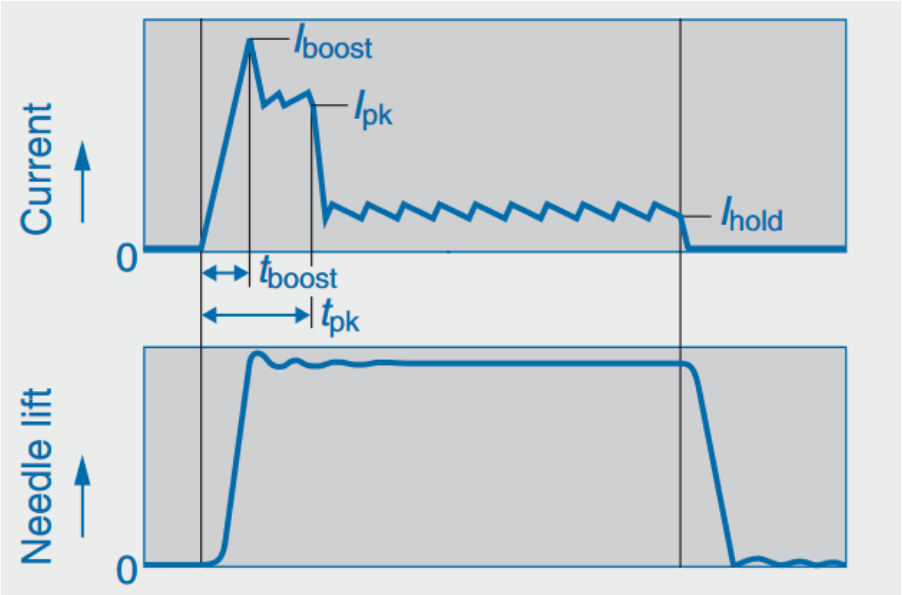

FIGURE 2.2: Actuation of the HP injection valve HDEV 5.2. [1]

physical properties between water and gasoline may jam the injector. A first step to avoid the clogging of the injector was to use demineralized water. In addition, a cleaning process had to be designed. This is explained in section 2.1.3.

2.1.2 Power electronics

In car engines, fuel injectors are directly controlled by the engine ECU. This Electronic Control Unit collects data from sensors located into the engine bay in order to optimize the engine performances. The HCCI test bench was already equipped in this way but something was

[1] Adapted from [17]

needed to deliver a high current in a small amount of time to open the injector, as explained in section 2.1.1. Since the engine test bench is controlled by LabView, the solution had to be compatible with this software. The developer of LabView, National Instruments (NI), proposes a straightforward solution to the injector control, the NI-9751, a direct injector driver module. This solution offers an easy way to open the injection valve, which costs around 2400 €. This high price is explained by the fact that this module includes a boost converter to increase the typical 12 V voltage power supply from the car battery to a higher voltage in order to increase the current flowing in the injector coil up to a significant value. This boost voltage is between 65 V and 90 V for the injection valve presented above, but the NI-9751 module can deliver voltages up to 190 V.

Unlike car embedded applications, the laboratory test bench can use external power sources. Therefore, the boost converter is not needed anymore. The idea is to control the coil current through the applied voltage. To regulate the voltage, an electronic gate is connected between the injector and a 60 V power supply. Figure 2.3 is a schematic representation of this gate. The 15 V source feeds the gate, while the 60 V power supply delivers the high currents needed to open the injector. The information about the injection, i.e. the pick-up time (T1) and the holding time (T2), are entered by the user and sent by LabView to the MyRio. The role of this device within this context is to convert the injection parameters into a Pulse Width Modulation (PWM).

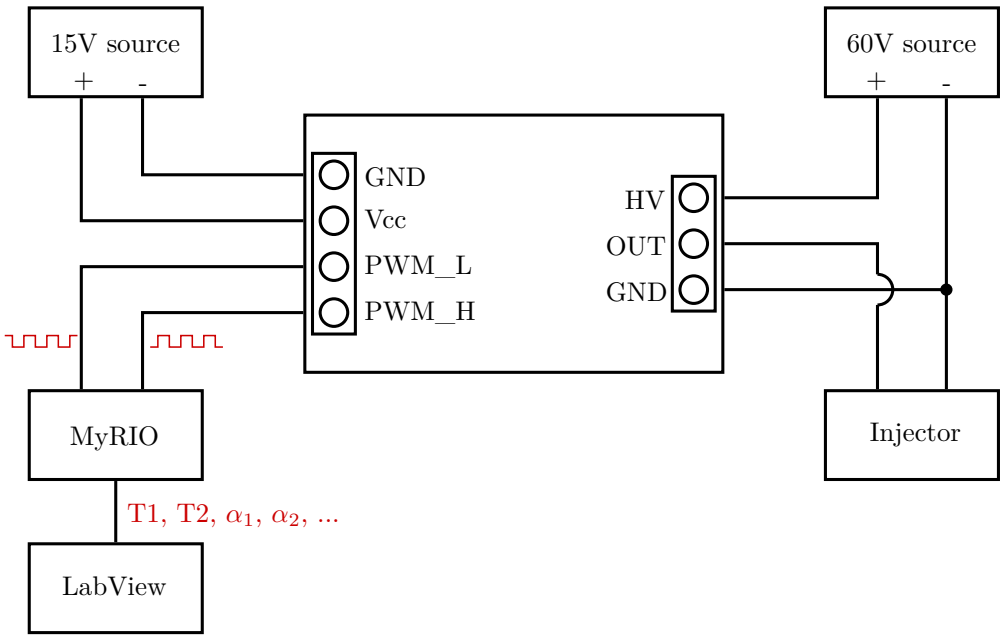

FIGURE 2.3: Electronic circuit controlling the injector.

Actually, it can be seen in Figure 2.3 that the gate is driven by two different PWM signals. A simplified schematic of this gate is depicted in Figure 2.4. The first PWM signal, called the ON signal, is used to open the connection between the injector and the 60 V voltage. The second one is used to connect the injector to the ground. It is called the OFF signal. One can easily guess that these two signals are actually the opposite of each other. However, there is a small gap between the ON and OFF signal to ensure that no short-circuit can occur between the 60 V source terminals.

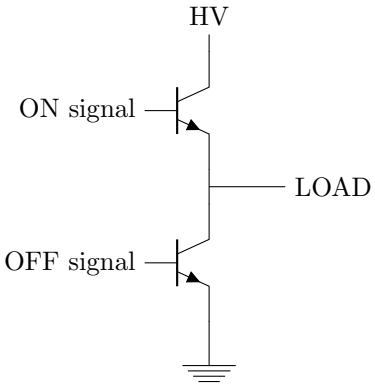

FIGURE 2.4: Simplified half-bridge gate.

This device controls the current flowing in the coil by changing the voltage applied to it. This is made possible by the PWM signal. This signal has a period of 10 μs and is composed of two different parts. The first one is for the pick-up phase, and its duty cycle is 80%, meaning that the PWM is high during 8 μs and low during the remaining 2 μs. The second one, for the holding phase, has a duty cycle of only 30%. Finally, the effective mean voltage applied to the injector during the pick-up phase is 48 V and 18 V for the holding phase. Since the coil current in steady-state is directly given by the Ohm's law, the higher the voltage, the higher the current will be. The Figure 2.5 depicts the pattern followed by the current during the two phases. One can observe that when the PWM is high, the current is increasing and then decreasing when the PWM is low. However, it keeps oscillating around a mean value, which is only depending on the PWM duty cycle.

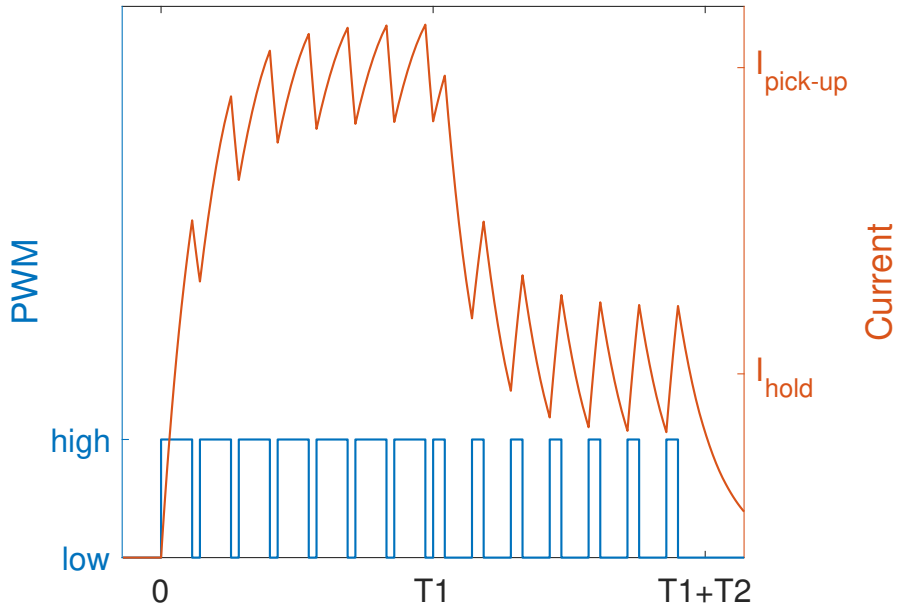

FIGURE 2.5: Actuation of the injector.

2.1.3 Pressure rise system

The water needs to be highly pressurized as the aim is to spray water directly into the cylinder. Nonetheless, the injection pressure has to be modifiable within a wide range from 20 to around 200 bars in order to study its impact on thermal stratification. The lower limit corresponds to a case where the water is injected early during the compression phase and therefore in a near atmospheric pressure environment. Moreover, a safety margin of 20 bars is arbitrarily designated to avoid any back-flow through the injector. On the other side, the upper limit is a classical order of magnitude for direct injection with a gasoline injector according to Bosch GmbH [18].

To reach those various pressures, several solutions are possible candidates. The first is based on a water pump, the second is made of two hydraulic cylinders facing each other (one driven by hydraulic oil while the other is filled with water), and the third solution involves to use a nitrogen gas cylinder with a pressure regulator to set the water pressure through the applied nitrogen pressure.

The solution consisting of a water pump provides the cost advantage since the pump can be recovered from an old high-pressure washer. Furthermore, there is no restriction on the pressurized water quantity unlike other solutions which can only compress a limited amount of water. On the other hand, this setup is not adapted for small flow rates unless by using a suitable pump. This would increase the cost and therefore the main advantage of this solution would be lost. As an order of magnitude, the water flow is varying between 225 and 900 ml/h for an injected mass going from 5 to 20 mg/cycle. Besides that, the pump provides a continuous flow rate while the injection valve opens periodically, which can create some pressure fluctuations. Finally, the pressure output is non adjustable since those pumps are usually designed to deliver a constant output pressure.

The second solution, made of two face-to-face mounted hydraulic cylinders, uses oil pressure in the first cylinder to pressurize the water in the second cylinder. This much more costly solution offers a smoother operation than the previous one due to the buffer tank effect of the hydraulic cylinders. Contrary to the previous solution, this one implies a limited pressurized water quantity equivalent to the volume of the second cylinder.

Finally, the third solution is inspired from the second one, but uses compressed nitrogen to pressurize water. Therefore, the water quantity is still limited. On the other hand, due to the absence of moving parts, the cost is drastically reduced. Moreover, this solution offers an additional benefit since the injector may be cleaned with nitrogen. Given that there is no physical separation between water and nitrogen, one may be worried by the nitrogen content of water because of the biphasic environment, but according to Richard P. Kennan and Gerald L. Pollack [19], the solubility of nitrogen in water is only $1.7 g_{N2}/l_{H2O}$ at 200 bars, and decreases with pressure.

Given the rather high prices of the first two solutions with respect to their limitations, the third solution has been chosen. It provides easily adjustable pressures and a simple way to clean the injector at a lower price. This solution requires a tank to store water, a nitrogen bottle, a pressure regulator and several ball valves. The correct handling of these valves allows an easy filling of the tank and a simple way to bypass the tank to clean the injector. All of these components must be able to withstand a 200 bars pressure and must be corrosion-resistant.

Therefore, all the installation is made out of stainless steel. These requirements result in a high price, although not quite to the same extent as the first two solutions.

The installation can be observed in Figure 2.6, along with the calibration test bench. The pressure rise system itself is composed of seven valves. Nitrogen is supplied via valve 2, which is connected in series with the pressure regulator. Water is leaving the tank via valve 6, which is directly connected to the injector. Under normal operation, valves 2, 5 and 6 are open while the others are closed. For the injector cleaning, valves 2, 3 and 7 are open and the others are closed. This bypasses the water tank and therefore the injector is supplied with nitrogen. Valves 1 and 4 are used for filling the tank.

(A) Setup used for the calibration measurements. (B) Zoom on the pressure rise system.

FIGURE 2.6: Overview of the calibration test bench.

2.1.4 Methodology

Before proceeding with the measurements, a range of suitable water masses had to be explored. In the research work of Lawler *et al.* [16], the engine is a 2.0 liters gasoline engine with three out of the four cylinders disabled. The displacement volume is therefore 500 ml. The monocylinder engine used in this thesis having a displacement of 435 ml, this is a good indication of the order of magnitude of the targeted water masses per engine cycle.

The volume capacity of the tank also has to be taken into account not to run short of water too quickly. The calibration has then been performed for water masses going from 0 to around 20 mg/cycle. As depicted in Figure 2.6a, the calibration is taking place out of the engine. In addition to the pressure rise system, a precision balance and some temporary clamping parts have been used to complete this task. The clamping parts are steel components used to hold the injector in place and ensure the sealing of the installation.

The first step of the calibration is to fill in the tank. The progressive opening of valve 4 depressurizes the system, and water is injected through valve 1 with the help of a syringe. Once the tank is full of water, only valves 2, 5 and 6 are opened. The system is then pressurized and ready to use. In order not to clog the injector with impurities, demineralized water has been given the preference. This reasoning is also valid for WDI in the engine.

Pick-up and holding times are entered through a customized LabView interface and the injection pressure is adjusted thanks to the pressure regulator. The precision balance used is a Sartorius Practum 2102-1S, which has a readability to 0.01 g. A small flexible plastic tube connects the injector tip to a container placed on the weighing platform. To have an accurate measure of the injected mass, sequences of 2000 identical injections have been fixed and the total measured mass is thus divided by 2000 to obtain the water mass per injection. This operating procedure is repeated two times for each different point, and the mean value is encoded. As the engine will run at 1500 rpm, the period between two injections is 80 ms. Due to the important number of different injections to calibrate, the calibration period is set to 40 ms. A comparison has been made to ensure that this increase in injection frequency has no impact on the proper functioning of the injector.

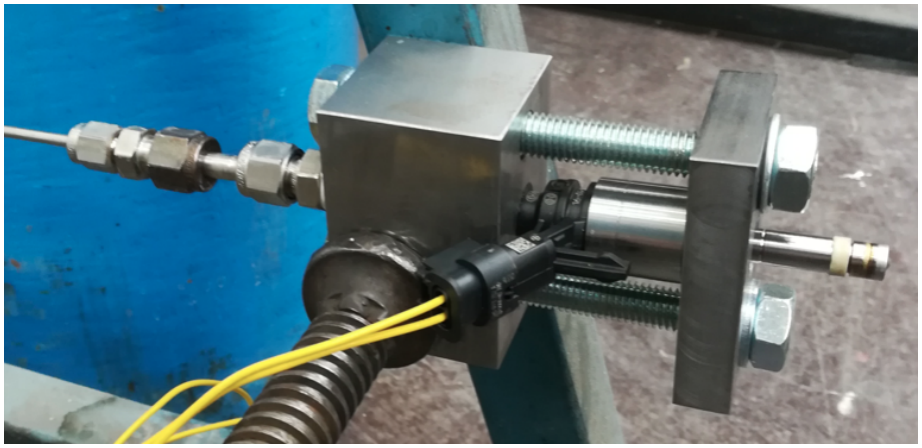

FIGURE 2.7: Zoom on the clamping parts used for the calibration.

Finally, multiple efforts were made not to jam the injector. Indeed, the first injector that was meant to be used as part of this master thesis jammed before calibration could be performed. Even though it was second-hand, there are several hypotheses to explain this : the use of tap water, rust due to incomplete drying after use, dirt initially present in the piping and a piece of damaged o-ring which could have obstructed the injector. As shown in Figure 2.7, the injector is clamped in a block of steel. Therefore, after each use, it was cleaned with high pressure nitrogen (by properly configuring the valves, as explained in section 2.1.3) and then carefully pulled out of the clamping parts to ensure its drying to prevent the formation of rust.

2.2 HCCI test bench

This section describes the HCCI test bench, from the engine block to the instrumentation. The successive modifications of the original engine are listed. The intake and exhaust systems of the bench are detailed. Then the new cylinder head with its features is presented. This section is concluded by a quick word on the data acquisition and control system, which has been slightly modified to integrate the injection parameters.

2.2.1 Engine specifications

The base engine used for the experimental tests of this work is a four-stroke monocylinder Diesel engine, the Yanmar L100V. It is shown in its original version from the supplier in Figure 2.8. This engine, intended for industrial use, has a relatively simple architecture thanks to its air-cooled and monocylinder configuration. It therefore offers ease of machining and instrumentation. For the sake of continuity, the successive modifications performed on the engine are detailed below.

FIGURE 2.8: The original Yanmar L100V monocylinder engine. [2]

Yanmar L100V	
Engine type	Air-cooled Monocylinder 4-stroke, Diesel
Displacement	435 ml
Original Compression Ratio	19
Modified Compression Ratio	23.5
Intake valve closure (ICV)	127° aTDC
Exhaust valve opening (EVO)	127° bTDC
Cylinder bore (B)	86 mm
Piston stroke (S)	75 mm
Connecting rod length (L)	120.5 mm
Crank radius (r)	37.5 mm
Rotation speed	1500 rpm

TABLE 2.1: Engine specifications.

The CI engine was first transformed into a HCCI engine as part of the thesis of Bhaduri [13]. The direct fuel injector was replaced by a spark plug whose role was solely to seal the cylinder head. The fuel tank and the injection pump were removed, as well as the standard recoil starter. The apparent engine fan was then equipped with a variable opening cover. As the HCCI engine had to be able to operate with syngas, the original deep bowl piston was modified into a low turbulence shallow bowl shape, reducing the compression ratio to 12, based on the design study of F. Contino [20].

[2] https://www.yanmarindustrial.eu/Products/Diesel-Air-cooled-industrial-engines/L100V-75/

Afterwards, the compression ratio has been changed to 23.5 with a flat piston crown for the research works of Pochet on hydrogen-ammonia blends. This arises from a trade-off between a high CR, around 40, needed to promote ammonia combustion, and a lower CR needed to prevent hydrogen combustion from ringing [21]. In this work, only hydrogen is used as fuel so this latest configuration has been used. The cylinder head will be modified as described in section 2.2.3 but the geometrical specifications of the engine remain unchanged with respect to Table 2.1.

2.2.2 Test bench components

This section describes the major components of the monocylinder HCCI test bench. The vast majority of the current bench was already present as part of the thesis of Bhaduri [13]. Therefore the choice of the components and the conception of the bench will not be explained here, since this work has already been done by Bhaduri. An overview of the test bench as used during this master thesis is presented in Figure 2.9.

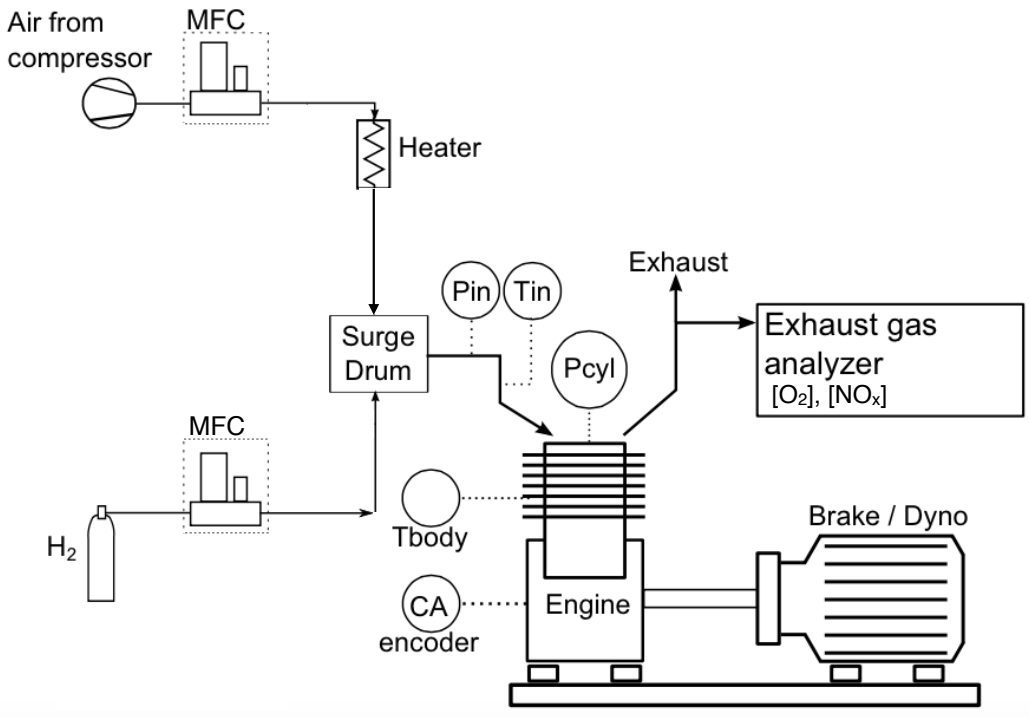

FIGURE 2.9: Schematic representation of the HCCI test bench. [3]

It has to be noted that this schematic does not include the WDI system, it is however represented in the test bench P&ID (see Appendix A). For the experiments performed in this work, the intake mixture was only composed of air and hydrogen. Air from the compressed air network of the Stevin laboratory and hydrogen from the bottle are supplied to the intake system through

[3] Adapted from [13]

their respective Mass Flow Controller (MFC). The hydrogen mass flow is entered as an input to its MFC according to the desired equivalence ratio. The air flow is then adapted to keep a constant intake charge flow, maintaining the intake pressure slightly above 1 bar. A MFC is a device constituted of a pipe in which two stainless steel probes are placed : an upstream heating probe and a downstream temperature probe. The power needed to maintain a constant temperature difference between these two probes allows the computation of the exact mass flow, since the specific heat of the fluid is known beforehand. MFCs are therefore control and sensing units at the same time.

FIGURE 2.10: HCCI test bench, view from the intake side : (1) electric heater, (2) gas mixer, (3) surge drum, (4) nitrogen bottle, green arrows represent the hydrogen flow, blue arrows represent the air flow.

The air flow then passes through a 15 kW electric heater. In fact, as can be seen in Figure 2.10, it previously passes through an electronically controlled 3-way splitting valve, but this function has not been used and air only follows the path shown by the blue arrows. The desired intake temperature is entered by the user and a PID control adapts the heater temperature depending on the measured temperature. The hydrogen path coming from its MFC is shown by the green arrows. It passes through an evaporator, which has not been used during the experiments. The hydrogen flow is then mixed with the hot air flow and the charge enters a 10 liters surge drum. The role of this component, which is insulated as much as possible, is to create the homogeneous mixture of air and hydrogen and to absorb the temperature oscillations of the intake charge. Figure 2.10 also shows the nitrogen bottle used to pressurize the water tank.

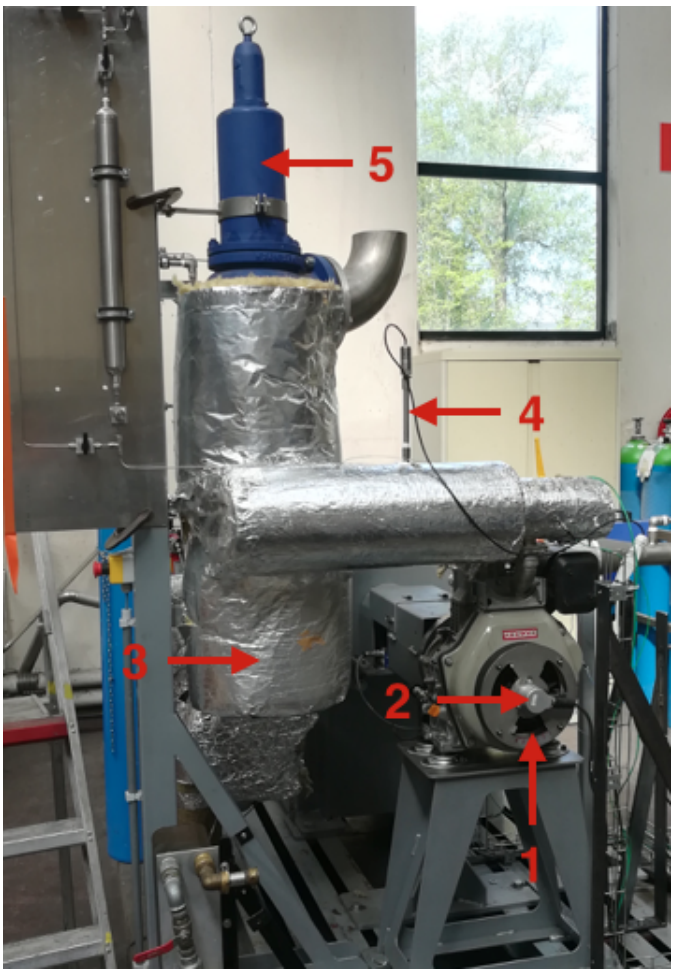

FIGURE 2.11: A front view of the HCCI test bench : (1) manually-operated air cooling system, (2) rotary encoder, (3) surge drum, (4) intake pressure sensor, (5) safety valve.

As shown in Figure 2.11, a large safety valve is mounted on top of the surge drum. Its role is to evacuate the excessive pressure towards the high ceiling of the Stevin laboratory if the absolute pressure inside the drum exceeds 2 bars. Indeed, back-flows from the engine to the intake can happen if the intake pressure is below 1 bar, and too high fuel mass flows can be mistakenly entered by the user.

The intake pressure sensor can be seen between the surge drum and the intake valve of the engine. The intake temperature sensor, for its part, cannot be seen on this picture since it is located very close to the intake valve. As mentioned in Chapter 1, HCCI combustion is very sensitive to the charge temperature. Yet, charge temperature evolution itself depends on the cylinder wall temperature. In order to have a good consistency between the different measurements, wall temperature has to stay as constant as possible. The only control that can be implemented on the wall temperature is the manual variable opening of the engine cover. To preheat the engine before combustion takes place, the cover is generally closed. On the other hand, when combustion occurs, wall temperature can rapidly increase and the cover is therefore opened. The only sensor allowing to monitor the cylinder wall temperature is the T_{body} sensor, which is situated on the outside of the engine block. Thermal inertia strongly comes into play,

so with a bit of practice, the cover is handled with anticipation. Finally, the rotary encoder mounted on the crankshaft is also shown in Figure 2.11. It measures the angular position of the crankshaft with a 0.1 CAD resolution.

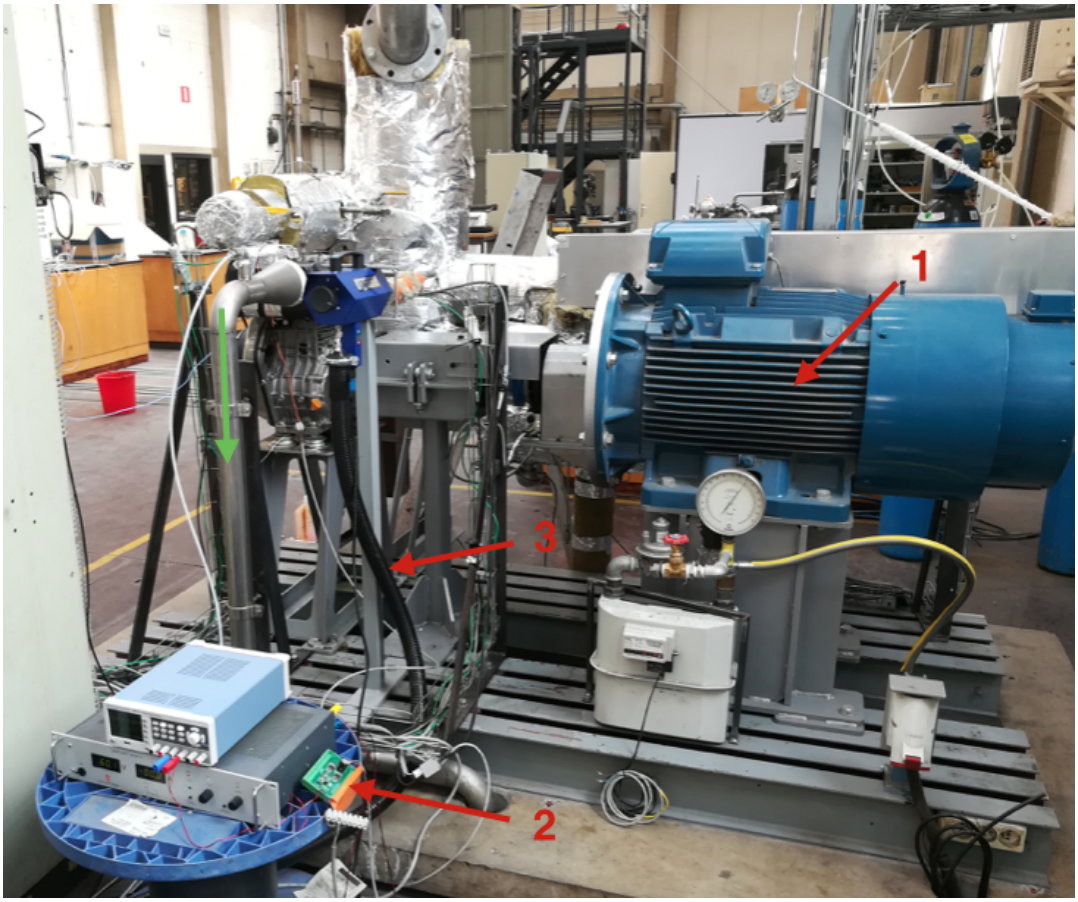

FIGURE 2.12: HCCI test bench, view from the exhaust side : (1) electric generator, (2) injector control electronics, (3) heated sample line, green arrow represents the exhaust flow.

Figure 2.12 shows a view of the test bench from the exhaust side. The exhaust gases flow in the pipe as depicted by the green arrow, which allows their extraction. A portion of these gases is sampled by a heated line, leading to the Tethys exhaust gas analyzer. The HCCI engine is coupled with a 55 kW three-phase induction generator (WEG W22 IE2) which act as a load and thus induces a brake torque. This electric generator can also act as a motor for the start of the engine. The Mitsubishi FR-A741-55k frequency variator allows to control the engine speed and delivers the power generated by the electric motor to the electrical grid. Finally, the voltage sources and the electronic gate controlling the injector can also be seen in Figure 2.12.

2.2.3 Modification of the cylinder head

The cylinder head has to be modified in order to host the injector. It has been decided to buy a new one from Yanmar and to machine it. A schematic of the modified cylinder head is illustrated in Figure 2.13, as well as the clamping part needed to hold the injector in place. A mounting sleeve has also been machined for its guidance function as well as to ensure the sealing of the

inner side of the installation. The air cooling cavity and the cylinder indeed have to be isolated from each other. This sealing is provided by the annealed copper washer which is flattened by the tightening of the bolts. The former Diesel injector hole has been widened to host the mounting sleeve. The role of the clamping part, besides maintaining the injector in place against the cylinder pressure, is to ensure the watertight seal, up to 200 bars, of the outer side of the installation. This is achieved thanks to the o-ring which is stuck by the clamping part. Both the sleeve and the clamping part have been machined from a bloc of stainless steel to avoid rust due to the possible contact with water. Here, the advantage of the simple design of the air-cooled monocylinder engine has been highlighted. To make such modifications on a water-cooled engine would probably have been cumbersome, and the cylinder head might not have been ready on time.

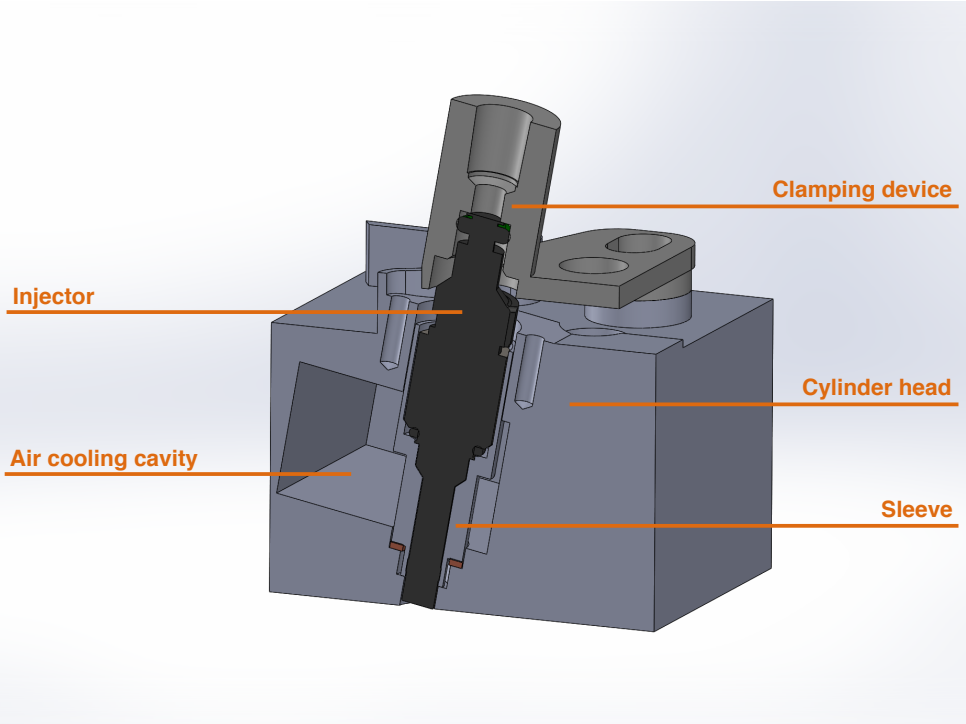

FIGURE 2.13: Schematic of the cylinder head modification.

Also, the hole for the pressure sensor has to be exactly at the same place as on the original cylinder head, in order to be able to make comparisons between previous and recent runs. But above all, the reason for this is that the ringing is a spatially distributed phenomenon. So, the ringing limits which have been observed previously had to remain valid. To that end, the plans concerning the pressure sensor bore have been provided by Breuer Technical Development.

Figure 2.14 shows a comparison between the original cylinder head and the current one, with the WDI system. As a reminder, the former Diesel injector hole was filled by a spark plug. It can finally be noted that the plastic part around the injector connectors, which can be observed in Figure 2.1a, has been cut to fit in the hole.

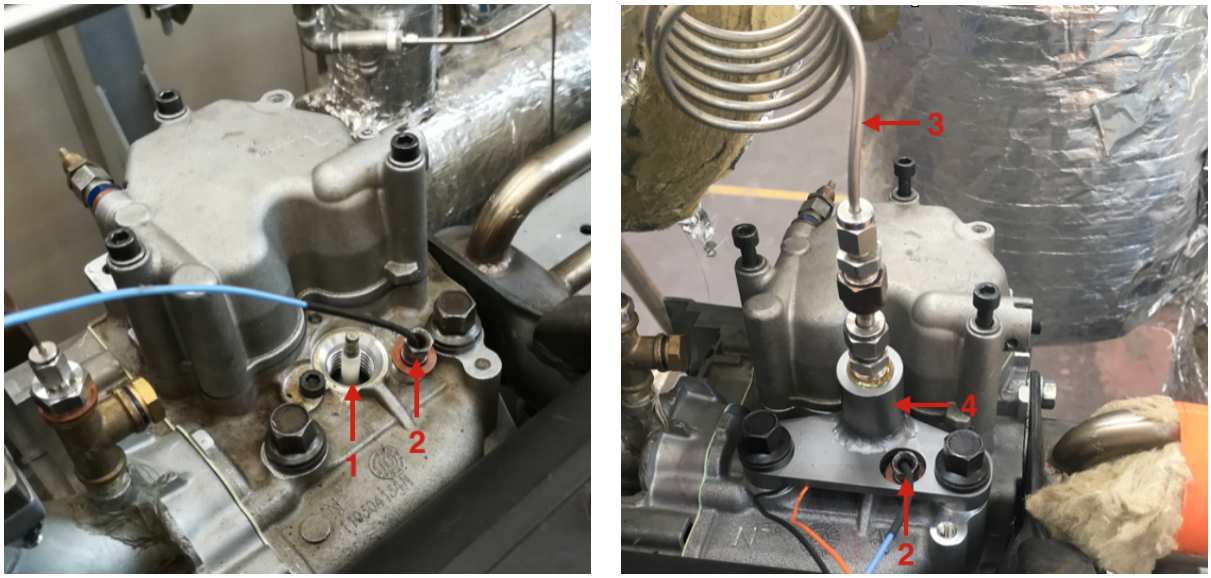

(A) Original cylinder head. (B) New modified cylinder head.

FIGURE 2.14: Pictures of the original HCCI cylinder head and the new "WDI" cylinder head : (1) spark plug, (2) AVL pressure sensor, (3) high pressure water supply, (4) clamping part.

2.2.4 Instrumentation and sensors

The acquisition and control equipment is listed in Table 2.2. A classification can be made between fast and slow instruments on the basis of their operational frequency. All these sensors and control devices were already present for the research works of Bhaduri [13], except the Lambda sensor and the WDI pressure regulator. Also, the Tethys exhaust gas analyzer replaced the former Testo 350 M/XL because the Tethys system is better suited for ammonia measurements, as required by the works of Pochet.

	Quantity	**Instrument**	**Details**
Slow control	Engine speed	Mitsubishi variator	0-1500 rpm ; 55 kW
	Intake temparature	Ohmewatt electric heater	15-200°C + PID control
	Intake mass flows	Brooks nv. MFCs	Air : 0-280 nL/min
			H2 : 0-55 nL/min
	Water pressure	Praxair pressure regulator	0-200 bar
Slow acquisition	Intake pressure	Kistler 4260	0-5 bar
	Exhaust pressure	Kistler 4260	0-5 bar
	Intake temperature	K-type Thermocouple	0-400°C
	Body temperature	K-type Thermocouple	0-400°C
	Exhaust gas composition	Tethys EXM400	NO : 0-200 ppm
	Exhaust oxygen content	Lambda sensor Bosch LSU 4.9	Lambda from 0.65 to >10
Fast acquisition	Crank angle position	Rotary encoder Heidenhain ROD 426	Resolution 0.1 CAD
	In-cylinder pressure	AVL GH15D	0-250 bar
	In-cylinder pressure	AVL FlexIFEM 2P2E	0-14400 pC charge amplifier

TABLE 2.2: Test bench instruments and sensors.

The most crucial sensors for a combustion analysis are the in-cylinder pressure sensor and the rotary encoder. The AVL sensor is a piezoelectric sensor whose diaphragm reacts to in-cylinder pressure changes. The piezoelectric effect is the change of polarization of the crystal structure of a material when a mechanical stress is applied to it. This change in polarization results in the creation of a charge density on the diaphragm surface. The charge amplifier which is coupled with the AVL sensor converts this variation of charge into a voltage signal. These types of sensors are very precise for measuring variations of pressure and are often used for research works and in motorsport. However, they cannot be used for truly static measurements.

The rotary encoder which has been mounted on the crankshaft provides the clock pulse used to sample the pressure signal of the AVL sensor and enables to know the crank angle positions associated with each pressure sample. The frequency of the rotary encoder is 3600 pulses/cycle, that is, a resolution of 0.1 CAD. It outputs two square-wave signals shifted by 90°allowing to know the angular positions as well as the direction of rotation. A third signal is in fact a single pulse for each turn of the shaft. This pulse therefore has to be aligned with the TDC.

2.2.5 NI hardware and software

The implementation of the data acquisition and control system of the test bench is explained by Bhaduri [13]. The NI CompactRIO system has been chosen for this application. This embedded industrial controller contains a real-time processor which is coupled to a Field Programmable Gate Array (FPGA) for the fast computations, and to a wide variety of Input/Output modules. The programming of this system was already done and is out of the scope of this thesis. It can nevertheless be noted that an additional digital output module, the NI9474, has been added to the system in order to control the injector. Indeed, the MyRio used for the calibration part was no longer available for the experiments on the engine test bench. The injector control interface has been joined to the LabView HCCI user interface, as shown in Appendix A.4.

Basically, to control the injector, three parameters have to be entered : the crank angle of the start of injection, θ_{SOI}, the pick-up time T1, and the holding time T2. On the other hand, the nitrogen pressure is given by the user to the system as an indicator. To prevent any risk of engine charge flowing back through the injector, a condition is imposed. There must be a minimum margin between the nitrogen pressure and the cylinder pressure.

As the injection occurs during the compression stroke, the difference between the fixed nitrogen pressure and the cylinder pressure, Δp, can drop down during the injection. To consider the worst case, the comparison is therefore made at the end of injection, i.e. at θ_{EOI} (the cylinder pressure at θ_{EOI} is obtained from the previous cycle). The condition can be written as :

$$\Delta p(\theta_{EOI}) > 20[bar] \tag{2.1}$$

The crank angle at the end of injection is computed as follows :

$$\theta_{EOI} \approx \theta_{SOI} + \frac{T1}{111} + \frac{T2}{111} \tag{2.2}$$

since at 1500 rpm, 1 CAD approximately corresponds to 111 μs.

If the FPGA returns a FALSE for the condition, WDI will not be allowed. This strategy ensures that there is no back-flow through the injector. Finally, it can be noted that the possibility of entering a second injection has also been added to the interface, and that the same safety strategy applies.

2.3 Computation of the heat release

The algorithm allowing to compute the heat release has already been explained in the thesis of Bhaduri [13], but a quick summary of the method might be useful.

As previously derived in section 1.3, the equation of the HRR is :

$$\frac{dQ_{gross}}{d\theta} = \frac{\gamma}{\gamma - 1} \cdot p \cdot \frac{dV}{d\theta} + \frac{1}{\gamma - 1} \cdot V \cdot \frac{dp}{d\theta} + \frac{dQ_{loss}}{d\theta} \tag{2.3}$$

In this equation, the pressure and the crank angle position are data from the AVL sensor and the rotary encoder. Therefore, the terms p, $\frac{dV}{d\theta}$, V and $\frac{dp}{d\theta}$ are known. Indeed, the volume and the crank angle derivative of the volume are obtained through the relation :

$$\frac{dV(\theta)}{d\theta} = \frac{V_d \sin(\theta)}{2} \cdot \left(1 + \frac{\cos(\theta)}{\sqrt{(L/r)^2 - \sin^2(\theta)}}\right) \tag{2.4}$$

where V_d is the displacement volume, L is the length of the connecting rod and r is the crank radius.

First, the heat loss term, $\frac{dQ_{loss}}{d\theta}$, is computed with the Newton's law :

$$\frac{dQ_{loss}}{d\theta} = h \cdot A \cdot (T - T_{wall}) \cdot \omega \tag{2.5}$$

where A is the total area of the combustion chamber, ω the angular speed in CAD/s and h is the convective heat transfer coefficient. The Hohenberg correlation has been chosen to compute this coefficient :

$$h_{Hohenberg} = \alpha_{scaling} \cdot V^{-0.06} \cdot p^{0.8} \cdot T^{-0.4} \cdot (S_p + 1.4)^{0.8} \tag{2.6}$$

Here, S_p is the mean piston speed and $\alpha_{scaling}$ has been chosen to 130 for this engine geometry.

At this point, the term γ needs to be computed. The ratio of the specific heats is a function of the bulk gas temperature and of the molar fractions of the chemical species. Thus, it depends on the state of the combustion itself. By introducing the Mass Burn Fraction (MBF) which illustrates how the reactants change into products, the c_p of the gas mixture can be expressed as follows :

$$c_p = (1 - MBF) \cdot \left[\sum_{i}^{reactants} (cp_i \cdot x_i) \right] + MBF \cdot \left[\sum_{j}^{products} (cp_j \cdot x_j) \right] \tag{2.7}$$

For each chemical species, the c_p is computed using the NASA polynomial :

$$c_p = R \cdot (a_1 + a_2 T + a_3 T^2 + a_4 T^3 + a_5 T^4) \tag{2.8}$$

where the coefficients a_1, a_2, a_3, a_4 and a_5 are proper to each species.
An iterative computation has to be performed. A first estimation of the bulk gas temperature is computed by assuming $T_{in} = T_{IVC}$:

$$T(\theta) = \frac{p(\theta)}{p_{IVC}} \frac{V(\theta)}{V_{IVC}} T_{IVC} \tag{2.9}$$

Now, the c_p of each species is known, and the c_p of the gas mixture is computed by initially assuming a MFB equal to zero (i.e. only reactants). Therefore, a first approximation of *gamma* is obtained :

$$\gamma = \frac{c_p}{c_p - R} \tag{2.10}$$

This leads to a first approximation of the HRR, which is itself used to compute the MBF, and so on. It is assumed that these steps have to be repeated twice [13].

Chapter 3

Injector calibration results

In order to study the impact of water direct injection on the HCCI engine performances, it was necessary to precisely know the amount of water injected per engine cycle. As explained in the previous chapter, a temporary test bench was designed to make the link between the mass of water delivered per injection and the three parameters characterizing the injection: the pick-up time, the holding time and the pressure difference across the injector. This section first shows the calibration results, i.e. the water mass injected per cycle as a function of the pressure and opening or holding time. Then, the uncertainties on previous data are discussed. Finally, results obtained using a high-speed camera are presented.

It must be highlighted that in this whole section, graphs are often presented with the absolute pressure on the x-axis (and not the pressure difference) because calibration tests were performed at atmospheric pressure, which will not be the case in the engine.

3.1 Variation of pressure and pick-up time

Figure 3.1 shows the injected mass in milligrams when varying pressure and pick-up time. For these tests, holding time was set to its minimum value, which is 10 μs. One can observe the decrease in injected mass after a certain peak, occurring at different pick-up times, depending on the pressure difference. Figure 3.2 displays the same data as Figure 3.1 but as a function of the pick-up time.

The choice for those operating ranges was made upon different facts. A pick-up time of less than 200 μs results in negligible masses injected per cycle: between 0 and 0.2 mg/cycle for pick-up times from 160 to 190 μs. Based on the work of Lawler *et al.* [16] and the limited capacity of the water tank, the mass range is expected to be included between 0 and 15-20 mg/cycle. Finally, the pressure range was delimited by engine-related aspects. The lower bound of 20 bars was set to be a safeguard against back-flow, which could occur if the in-cylinder pressure rises too quickly during an injection and eventually exceeds the injection pressure. On the other hand, the upper bound of 120 bars is the maximal pressure difference achievable between the input water pipe and the cylinder: the water pressure is the pressure of the nitrogen bottle (max. 180-200 bars), and the cylinder pressure is assumed at 60 bars (this will be discussed later, as it depends on the crank angle start of injection) . Moreover, the pick-up time and the holding time can only change by an increment of 10 μs which is the period of the PWM, see section 2.1.2.

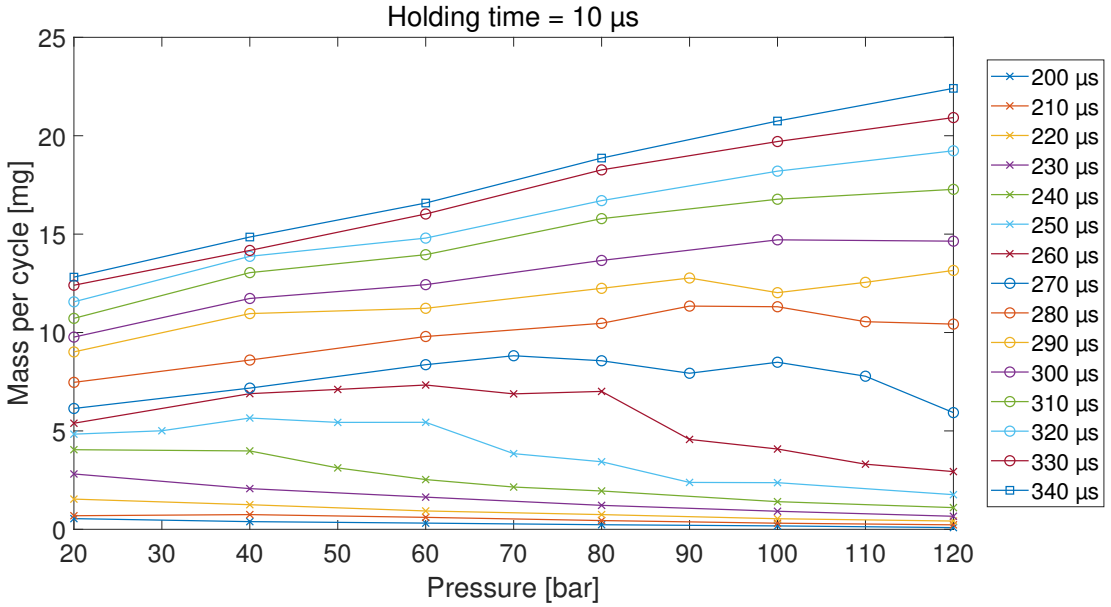

FIGURE 3.1: Injected mass per cycle as a function of the pressure, for different pick-up times.

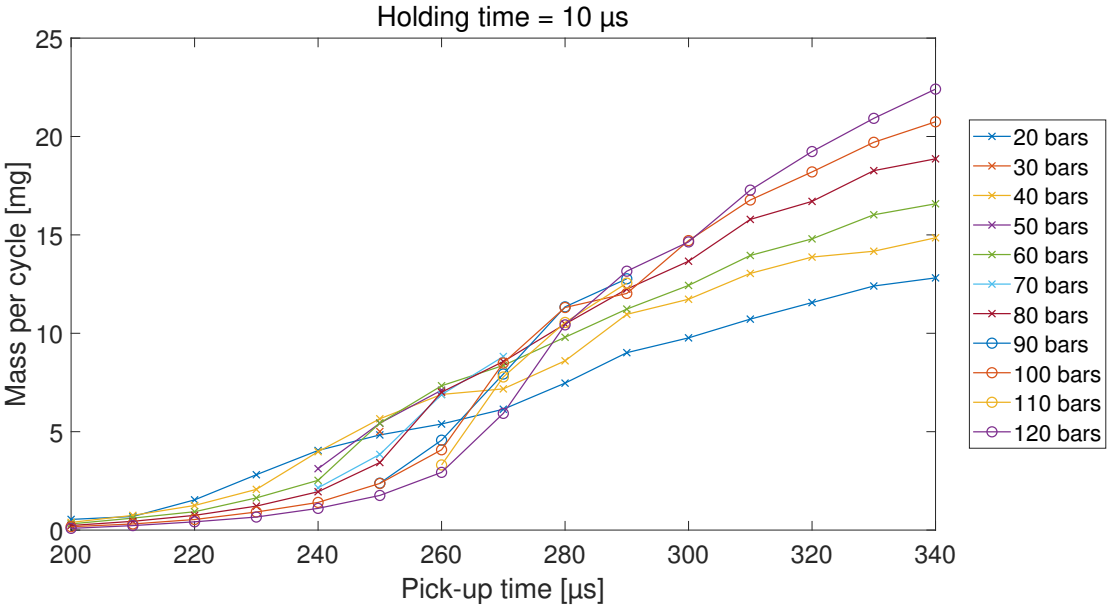

FIGURE 3.2: Injected mass per cycle as a function of the pick-up time, for different pressures.

3.2 Variation of the holding time

Figures 3.3 and 3.4 depict the injected mass as a function of pressure and holding time. For these tests, the pick-up time was set to a suitable value to reach the mass range, i.e. 210 μs. Varying the holding time in addition to the pick-up time gives an additional degree of freedom in the choice of the operating points. Therefore, it is possible to reach previously unattainable mass-pressure pairs.

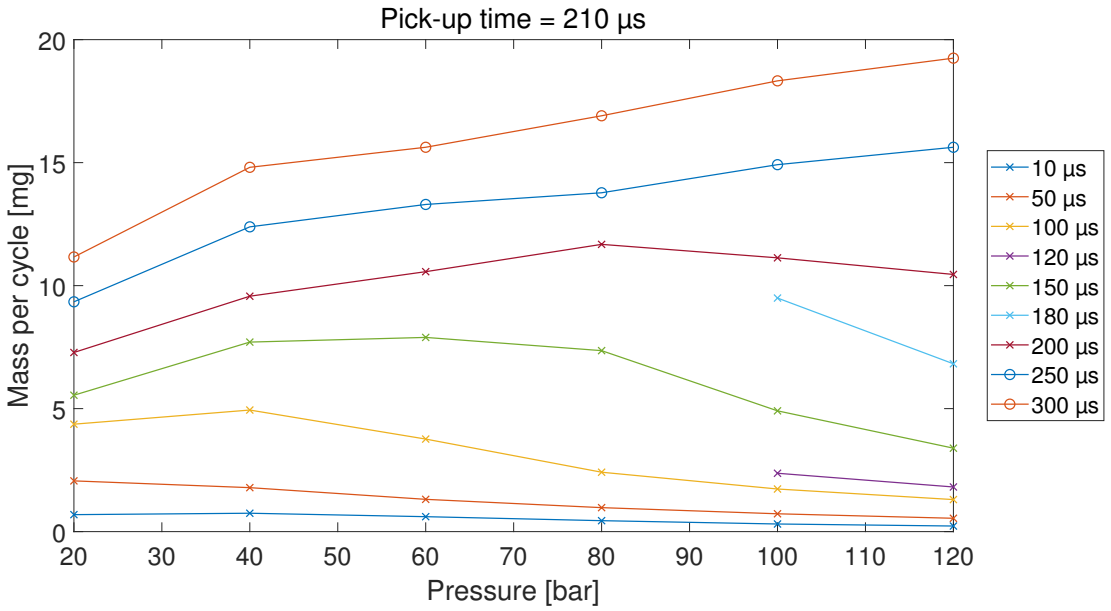

FIGURE 3.3: Injected mass per cycle as a function of the pressure, for different holding times.

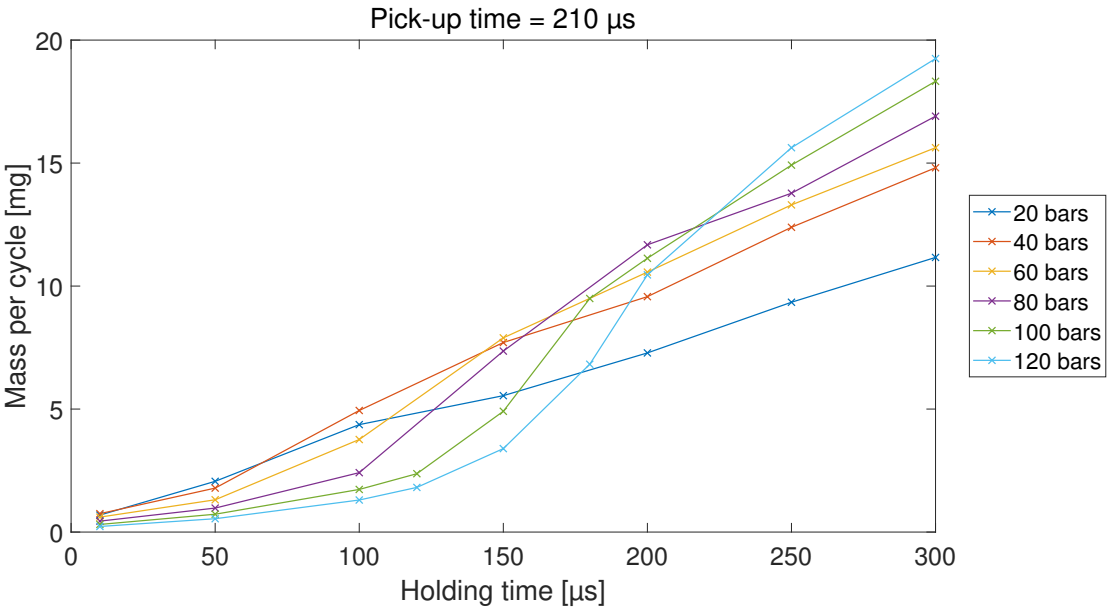

FIGURE 3.4: Injected mass per cycle as a function of the holding time, for different pressures.

3.3 Computation of the uncertainty on the injected mass

Since the aim of this master thesis is to study the impact of water direct injection on the power density of an HCCI engine, it is crucial to precisely know the amount of water injected into the combustion chamber, or at least, to guarantee that the actual injected value does not differ significantly from the expected value.

For this purpose, the uncertainty on the water mass is needed. In the engine, the main uncertainty source will be the pressure difference. Indeed, the injection time may be quite long (several hundreds of microseconds to a few milliseconds) and therefore, the in-cylinder pressure

will undergo a large variation. Furthermore, the uncertainty on the pick-up and holding time is negligible for the reason that it this directly controlled by the electronic circuit. On the basis of the above-mentioned facts, it was clear that the uncertainty had to be computed with respect to the pressure difference. Since the correlation between pressure and mass is non-linear, it will be linearized by segments, with each measurement point being doubled. Therefore, each line segment was characterized by four points.

The 95% confidence interval global uncertainty is computed as follows:

$$U_{global} = \sqrt{U_y^2 + (A_1 U_x)^2 + U_{est}^2} \tag{3.1}$$

Where U_y is the 95% uncertainty on the measured mass, i.e. 95% of the least count of the weighing scale divided by two. Indeed, best practice indicates that the 100% confidence interval of a measuring device is 50% of the least count around the measured value. This is depicted in Figure 3.5.

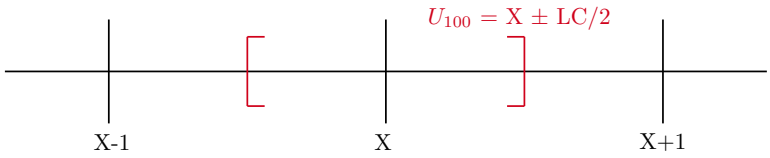

FIGURE 3.5: 100% confidence interval of a measuring device.

In this particular case, the injected mass was measured after 2000 cycles, so U_y had to be divided by 2000 in order to get the uncertainty per injection. In the same way, U_x is 95% of half the least count of the pressure regulator. A_1 is the coefficient from the linear regression $[\tilde{y}] = A_1[x] + A_0$, where $[\tilde{y}]$ are the approximations of the injected mass per cycle and $[x]$ are the pressures corresponding to these masses. Finally, U_{est} is the uncertainty on this linear regression. According to the Joint Committee for Guides in Metrology [22], it is computed as follows:

$$U_{est} = t_{0.025}\ \sigma \sqrt{\frac{1}{df} + \frac{(x - \overline{x})^2}{S_{xx}}} \tag{3.2}$$

where $t_{0.025}$ is the t-coefficient for a 95% confidence interval and df is the number of degrees of freedom, i.e. the number of observations minus the degree of the linear regression augmented by one. S_{xx} and σ are given by :

$$\sigma = \sqrt{\frac{\sum_i^n (y - y_{est})^2}{n - 2}} \tag{3.3}$$

$$S_{xx} = \sum_i^n (x - \overline{x})^2 \tag{3.4}$$

Figure 3.6 shows the uncertainties for two different pick-up times, while Figure 3.7 shows the uncertainties for two different holding times. The uncertainties on the pressure and on the measured mass being constant values, the global uncertainty value is mainly impacted by two

phenomena. First, because of the repeatability error, the global uncertainty will reach high values when the two masses measured at the same pressure are quite different. Secondly, the global uncertainty will increase around a steep slope, see Figure 3.6a. This is due to the fact that a small change in the pressure will induce a consequent change in the injected mass.

Finally, 85% of the measurements present uncertainties values below 10%, which is an acceptable threshold knowing the injector is used outside of its design characteristics. The remaining uncertainties are between 10% and 25%. These higher values are mainly due to the local steep slope or are occurring in very low injected masses regions. For example, the 200μs curve from Figure 3.1, which induces high relative uncertainty, even with low absolute uncertainty. By contrast, the contribution of the repeatability errors on the global uncertainties is negligible.

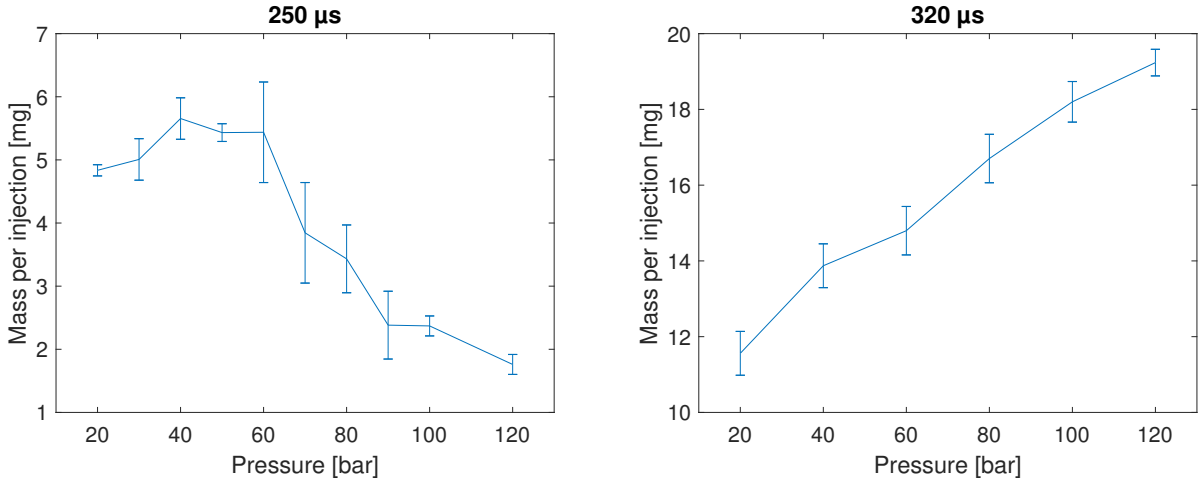

(A) Pick-up time of 250 μs. (B) Pick-up time of 320 μs.

FIGURE 3.6: 95% uncertainty on the injected mass.

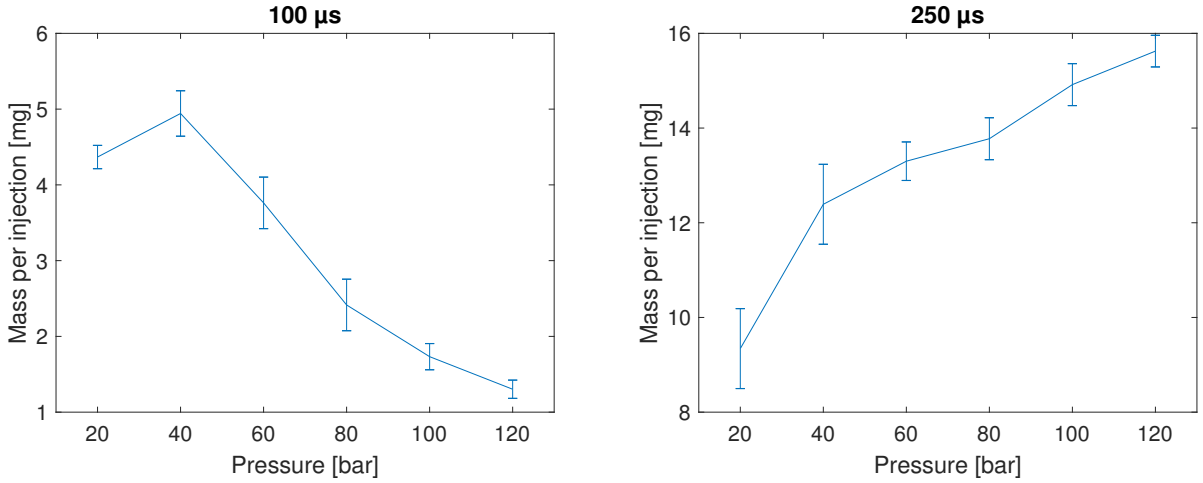

(A) Holding time of 100 μs. (B) Holding time of 250 μs.

FIGURE 3.7: 95% uncertainty on the injected mass.

3.4 High speed camera

To conclude this calibration part, the effect of pressure on the sprays has been observed. To this end, a high-speed camera was used. Recording was made at 15.000 fps, the maximal value allowing to keep an acceptable resolution. Resulting images were then processed in order to get the contour of the spray for every frame. With the intention of doing a clear illustration of the spray chronology, some of these contours were compiled on graphs. Figure 3.9 displays pictures straight from the high-speed camera and spray patterns sequences. With the recording frame rate of 15.000 fps, frames are 66,67 μs apart.

From the pictures, it was possible to estimate the actual time during which the injector is open. These results are presented in Figure 3.8 as a function of the theoretical total opening time, i.e. the sum of the pick-up time (T1) and the holding time (T2). One can observe that the actual injection time is much higher than the input time. It may be surprising at first sight, but according to Stephen Busch and Paul C. Miles [23], it is a perfectly normal behaviour for a fuel injector.

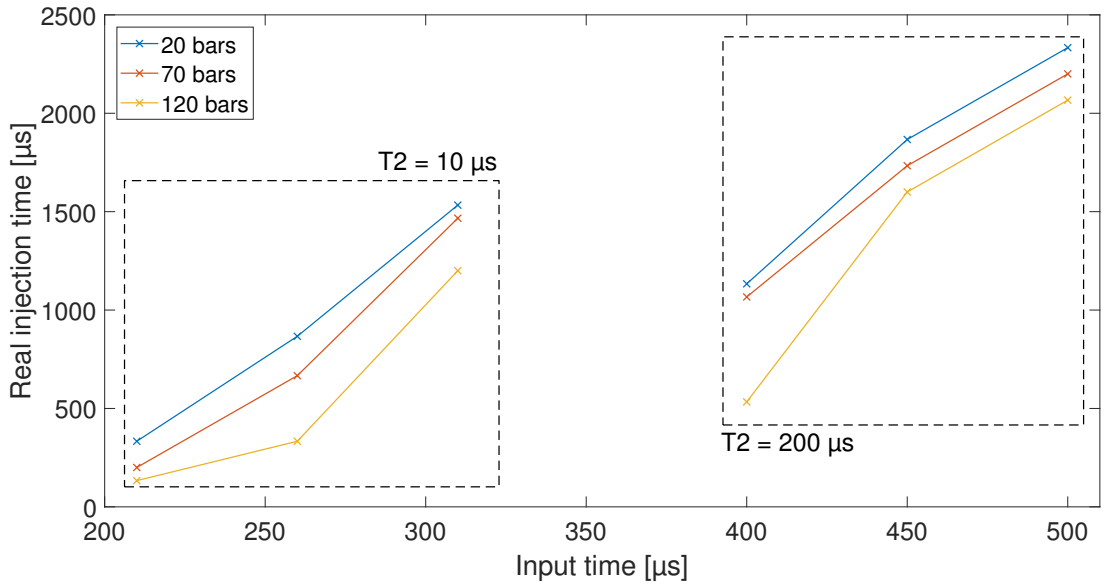

FIGURE 3.8: Comparison between effective injection time and theoretical time.

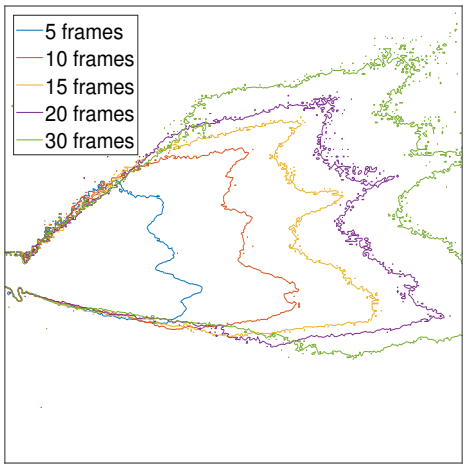

(A) 120 bars.

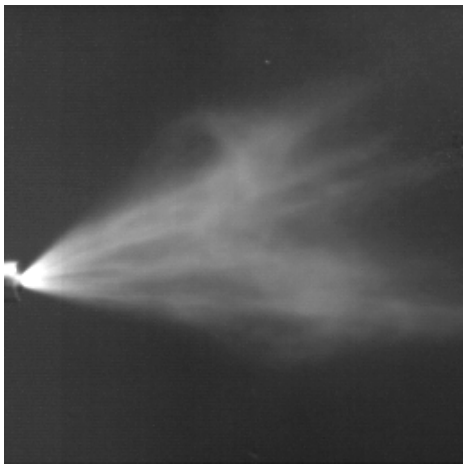

(B) 120 bars.

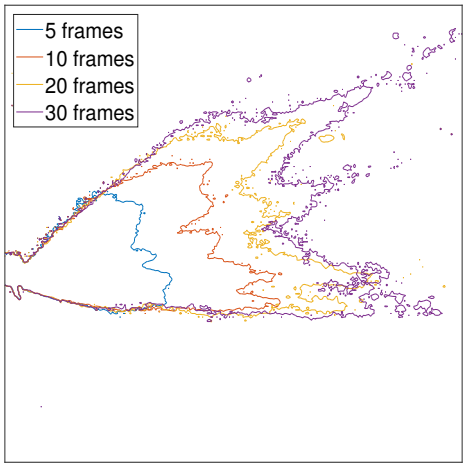

(C) 70 bars.

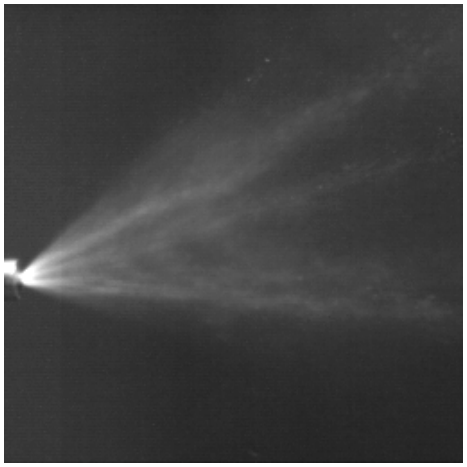

(D) 70 bars.

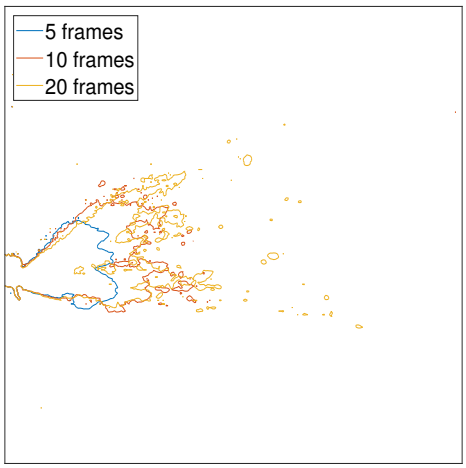

(E) 20 bars.

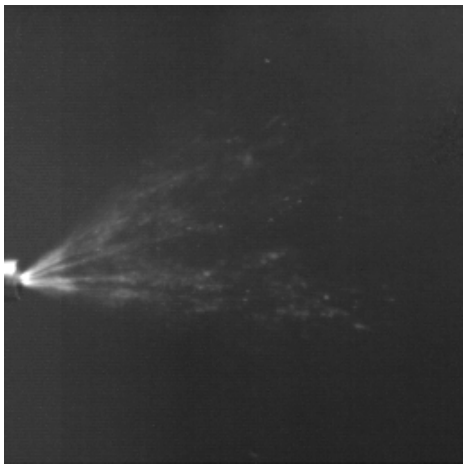

(F) 20 bars.

FIGURE 3.9: Illustrations of sprays at different pressures. The pick-up time was set to 300 μs and the holding time was set to 200 μs. Figures from the left column are the spray patterns at different timings, while Figures from the right column are pictures from the high-speed camera. As an order of magnitude, the injector tip is 7.5 mm wide.

Chapter 4

WDI effect on the engine performances

In the last chapter of this work, the effect of WDI on the engine performances is analyzed. First, the injected water masses that have been calibrated are validated in the engine conditions. Then, a comparison is made between thermal stratification due to WDI and combustion delay due to the variation of the intake temperature. Different injection parameters such as the injected mass, the injection pressure and the crank angle of injection have been investigated. At that point, it has been possible to extend the HCCI operating range thanks to WDI. A small section covers the NOx emissions and finally, the uncertainties of the presented results are discussed.

Results from the test bench consist of 100 consecutive engine cycles. In the following chapter of this work, those 100-cycles records will be referred as experiments or runs. During one engine cycle, i.e. two crankshaft revolutions since experiments are conducted on a 4-stroke engine, pressure is measured 7200 times, that means every 0.1 CAD. For all the experiments, the body temperature and the intake pressure were maintained at 105°C and 1.01 bar.

4.1 Validation of the calibration results

Before doing any engine-related experiences, a validation of the previous calibration was mandatory. Indeed, in the engine, many parameters differ from the calibration environment and may therefore influence the injected mass per cycle. First, calibration experiments were made at room temperature while the cylinder head is expected to be around 100-120°C, depending on the considered part. This implies thermal expansion of the injector tip and thus, a slight increase in the spray holes diameter. The temperature rise also causes the injector coil resistance to increase, thus decreasing the current flowing through it and consequently reducing the pulling force. Finally, calibration tests were operated under constant atmospheric pressure while injections into the cylinder can occur in a variable pressure environment depending on the injection duration and the crank angle of injection. As an example, a relatively short injection starting at the very beginning of the compression will take place under constant pressure while a longer injection starting in the middle of the compression phase will occur in a variable pressure environment.

To do this calibration validation, water was sprayed into the cylinder for a relatively long time (several minutes), resulting in a consequent drop in level in the water tank. The water volume needed to fill the tank was then divided by the number of cycles that occurred during this trial run. This method appears to be questionable but was precise enough to validate or not the different operating points from the previous calibration.

Comparisons between calibration and cylinder injections results are shown in Figures 4.1, 4.2 and 4.3. For those tests, only the pick-up time was modified, the holding time was set to its minimal value, 10 μs. Despite an offset for some time ranges, the engine tests trend sticks to reality. However, two outliers have to be reported for small pick-up times in Figures 4.2 and 4.3. It is important to stress that those two points have a totally different behaviour from their equivalent-mass counterparts from the linear region. Indeed, although the same amount of water is injected, the impact of the outliers on the engine is almost negligible compared to their counterparts fitting the curve.

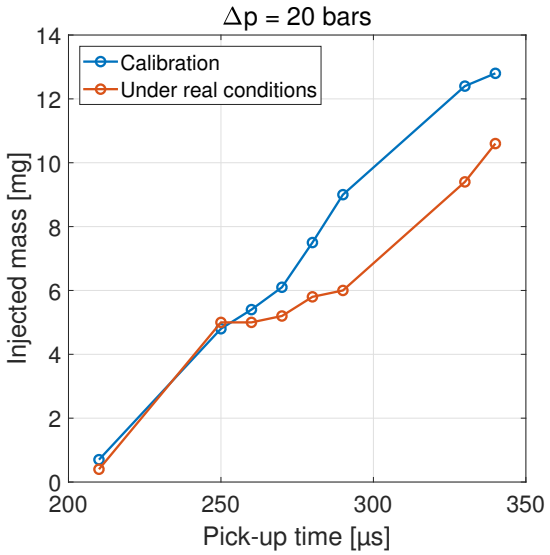

FIGURE 4.1: Comparison between calibration and real conditions with a 20 bars pressure difference.

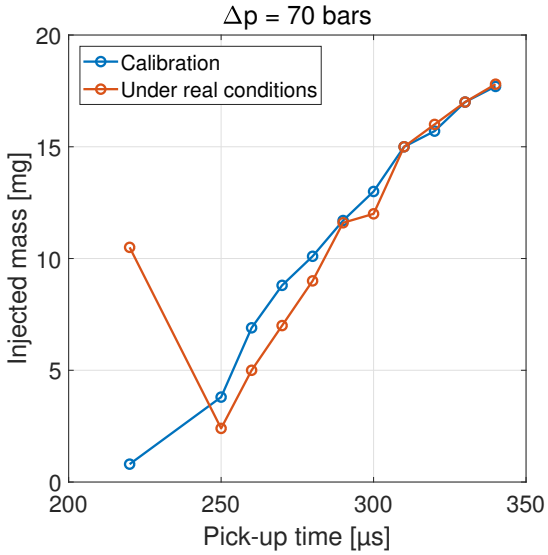

FIGURE 4.2: Comparison between calibration and real conditions with a 70 bars pressure difference.

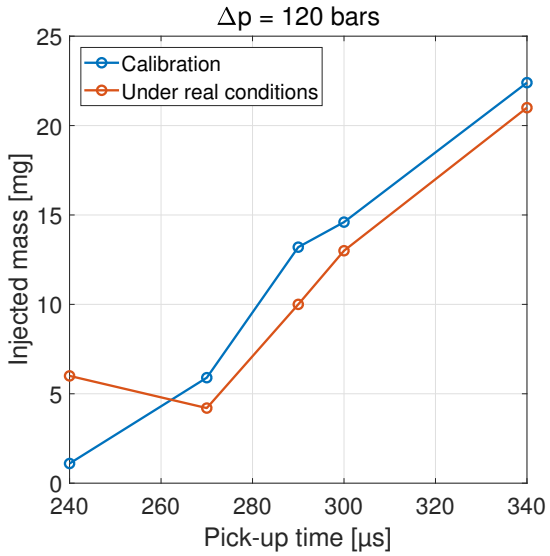

FIGURE 4.3: Comparison between calibration and real conditions with a 120 bars pressure difference.

It should be specified that for the following experiments, the updated calibration was used in order to ensure the best possible knowledge of the injected masses.

4.2 Impact of the intake temperature

As mentioned in Chapter 1, intake temperature is one of the main parameters in HCCI engines because of its great impact on the combustion timing. Figure 4.4 represents different HRR curves for an intake temperature sweep going from 69°C to 82°C while ϕ, the equivalence ratio, is maintained constant and no water is injected. The CA05, i.e. the crank angle corresponding to the moment where 5% of the combustion heat has been released, is marked for each curve with a diamond bullet. One can observe the increase in combustion delay as the intake temperature decreases. Furthermore, as the start of combustion occurs later, the combustion duration increases. This duration is indicated through the CA_{75-05}, i.e. the number of crank angle degrees between CA05 and CA75. This increase in combustion duration is explained by the fact that it is occurring in a lower pressure environment during the expansion phase. It should be noted that the CA_{90-10} is usually used to describe the combustion duration instead of the CA_{75-05}. The reason of this choice will be explained in section 4.3.1. These results will be useful in section 4.4 to compare the increases of combustion duration due to WDI or due to intake temperature changes.

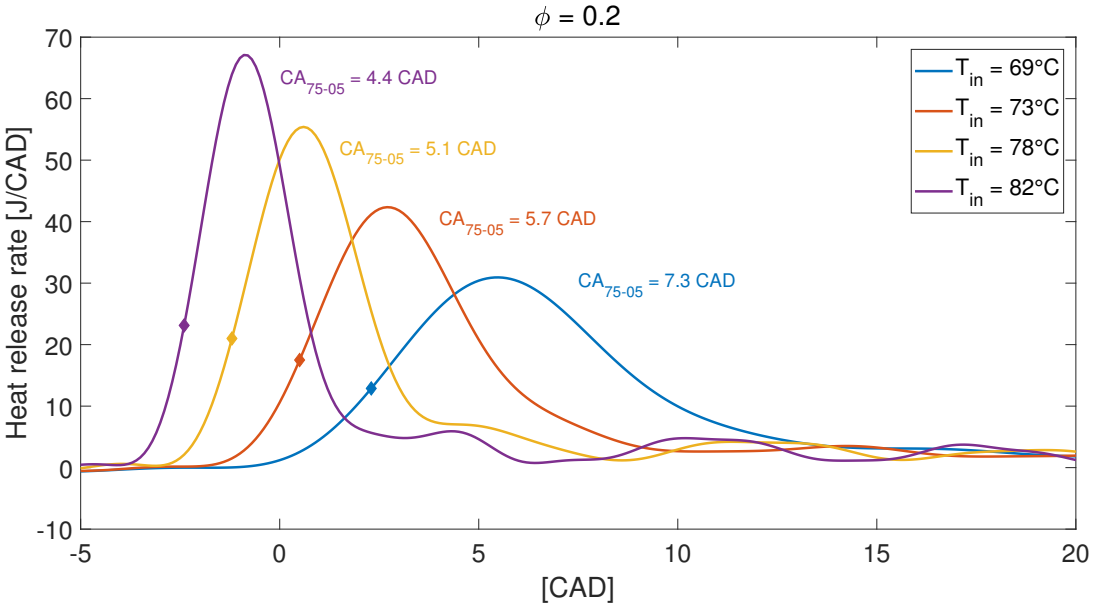

FIGURE 4.4: Impact of the intake temperature on the heat release rate.

One must pay attention to the fact that intake temperature is only recorded once, at the beginning of the 100-cycles record. Therefore, the intake temperature may slightly vary during the record without the variation being recorded. This variation can be seen on the real-time graph of the intake temperature from the LabView user interface in appendix A.4.

4.3 Influence of the injection parameters

This section will describe the impact on the engine performances of the different injection parameters, i.e. m_{H2O}, the injected mass per cycle, θ_{SOI}, the crank angle corresponding to the Start Of Injection (SOI) and Δp, the pressure difference between the cylinder and the water tank.

4.3.1 Mass of water

The injected mass of water has a great impact on the engine perfomances as depicted in Figure 4.5. For this water mass sweep, the equivalence ratio and the intake temperature were maintained constant. Water was injected 50° before TDC. As an order of magnitude, Table 4.1 gives the ratio between ΔH_{vap}, the enthalpy needed to vaporize the injected water and ΔH_{compr}, the change in enthalpy of the mixture during the compression phase, approximated by $\Delta H_{compr} = n_{mixture}\,\overline{c_p}\,\Delta T$.

m_{H2O}	3 mg	7 mg	12 mg
$\Delta H_{vap}/\Delta H_{compr}$	3.2 %	7.5 %	12.8 %

TABLE 4.1: Normalized enthalpy absorption.

One shall notice the similarity between the impact on the HRR caused by a decrease in intake temperature and the impact caused by an increase in injected water mass. The magnitude of these impacts will be compared in section 4.4.

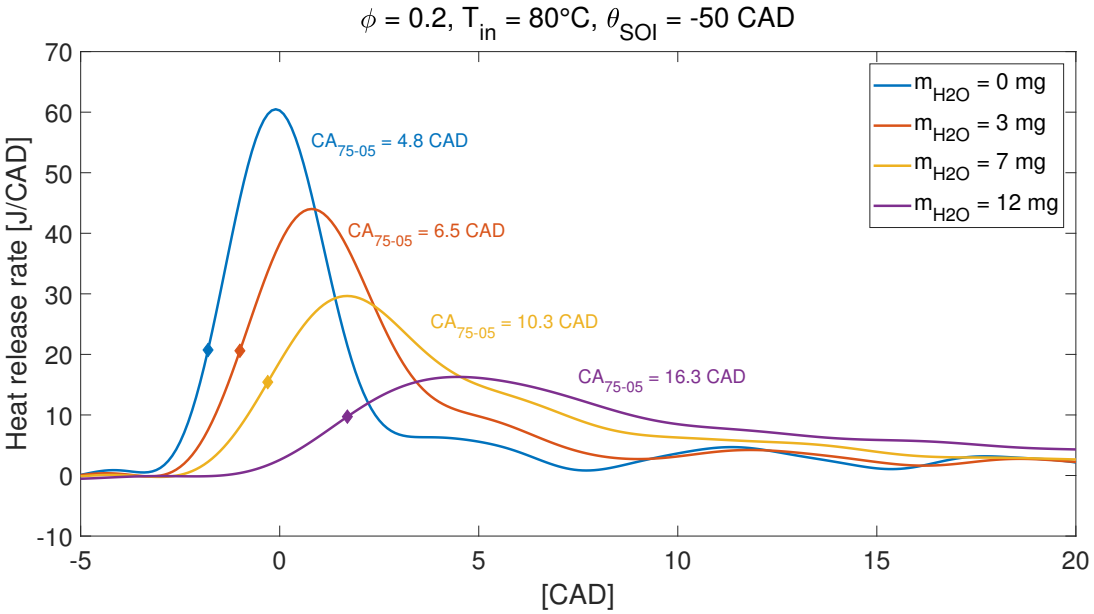

FIGURE 4.5: Impact of the injected mass on the heat release rate.

The different cumulative heat releases corresponding to HRRs from Figure 4.5 are presented in Figure 4.6. It is observable that the more water is injected, the less heat is released, which means that the combustion efficiency is decreasing. This is depicted in Figure 4.7. The reason why the CA_{75-05} was chosen as combustion duration indicator instead of the classical CA_{90-10}

is illustrated in Figure 4.6: as the water amount is increased, the combustion duration is considerably extended. Therefore, the CA90 lies in the nearly flat region of the heat release. In those particular conditions, a small increment in the heat release leads to consequent change in the CA90 position. The end region of the heat release should be flat in order to get a valid CA90, which is not the case here because of the post-processing code not being really adapted to WDI experiments.

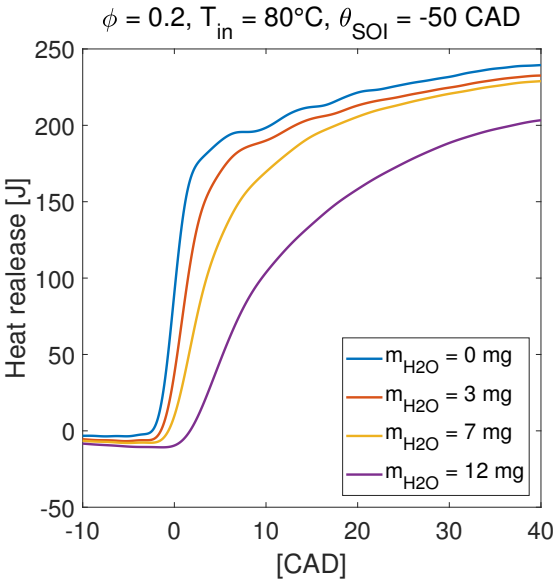

FIGURE 4.6: Impact of the injected mass on the heat release.

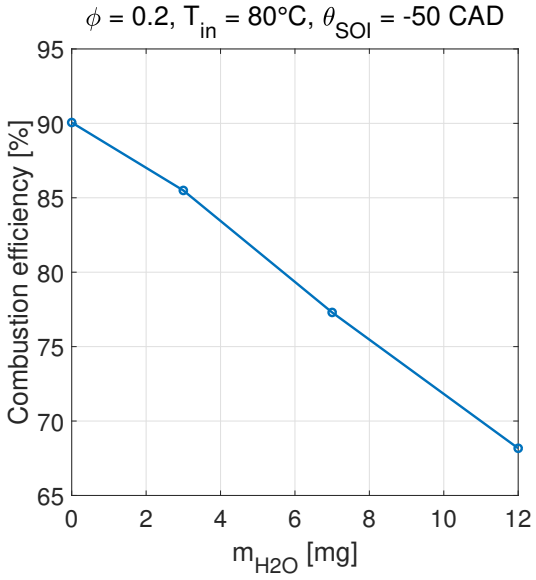

FIGURE 4.7: Impact of the injected mass on the combustion efficiency.

The heat release and the combustion efficiencies for water injections 70° before TDC are shown in Figures 4.8 and 4.9. Although general trends remain the same, an injection at -70 CAD will lead to a lower heat release than an equivalent-mass injection at -50 CAD.

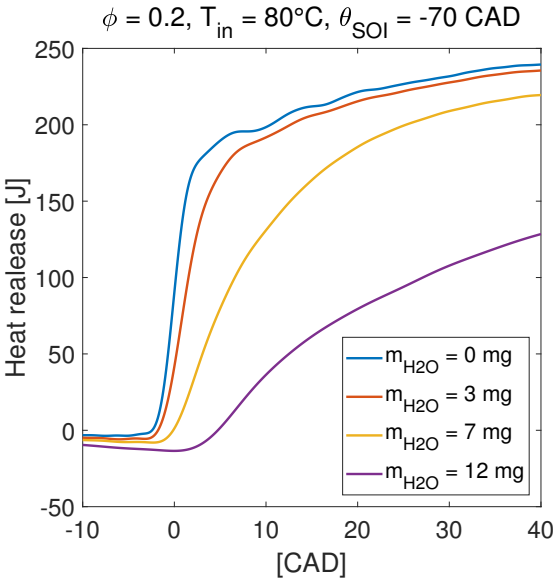

FIGURE 4.8: Impact of the injected mass on the heat release.

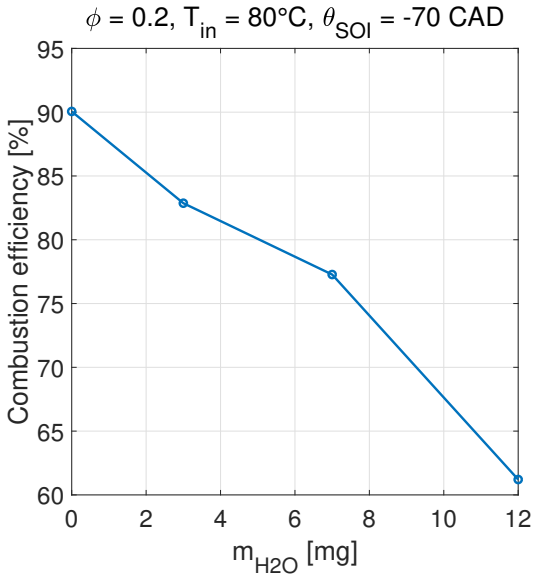

FIGURE 4.9: Impact of the injected mass on the combustion efficiency.

4.3.2 Crank angle of injection

As mentioned at the end of section 4.3.1, crank angle of injection has a non-negligible effect on the combustion. Figure 4.10 illustrates heat release rates for different angles of injection. It can be observed that the effect on the combustion is growing as the injection is occurring further from TDC. However, for very early injection, the combustion duration tends to decreases as depicted on Figure 4.11 for crank angles from 50 to 70 bTDC. The gap between 55 and 60 CAD bTDC seems to contradict this trend, but before drawing hasty conclusions a couple of things should be highlighted. Although all the parameters were kept constant and checked through their real-time measurements, the accuracy of one of them may be questioned. Indeed, the body temperature sensor is not really measuring the cylinder wall temperature but rather the temperature on the outside of the engine body. Nonetheless, it is a good indicator to keep consistency throughout the experiments. Unfortunately for this injection crank angle sweep, experiments took place in a transient phase where the cylinder wall temperature was supposed to be changing due to water injection while the measured temperature was constant. Therefore, until the post-processing phase, there were no clue about this transient body temperature. Due to lack of time, additional experiments on the crank angle of injection could not be carried out to confirm the decreasing part of the combustion duration from Figure 4.11. This decline in combustion duration might be due to a re-homogenization of the mixture since the injection takes place too early during the compression stroke. This effect was also observed by Lawler *et al.* [16].

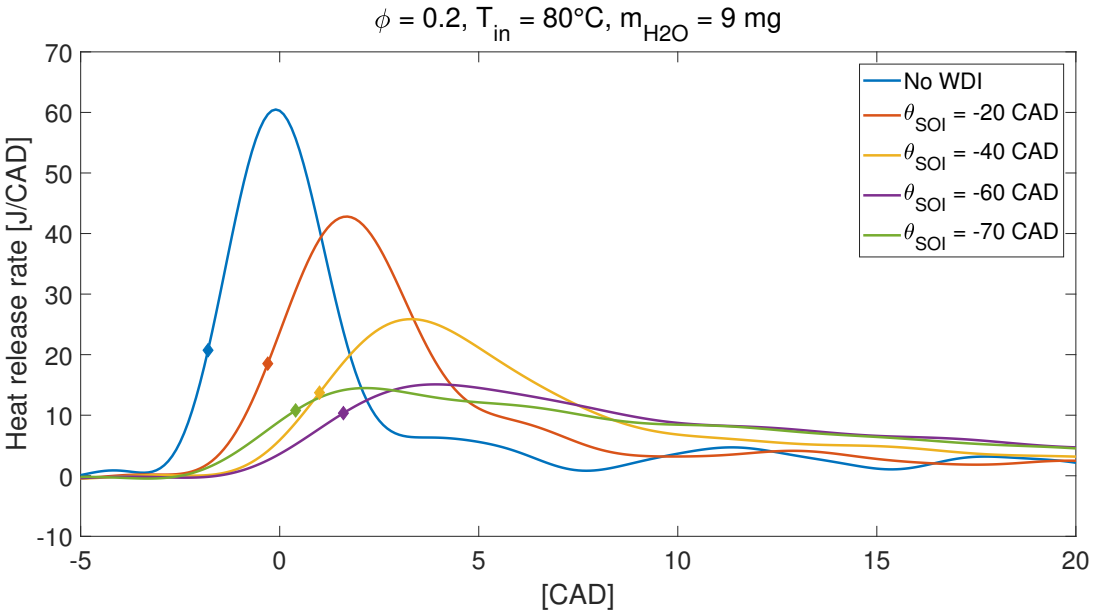

FIGURE 4.10: Impact of the crank angle of injection on the heat release rate.

To provide an insight of the injection geometry inside the chamber, Figure 4.12 represents the piston positions for different crank angles. The spray pattern is derived from the high-speed camera pictures from section 3.4 for a 120 bars injection. As a reminder, the cylinder bore is 86 mm and the piston stroke is 75 mm. The drawing is true to scale.

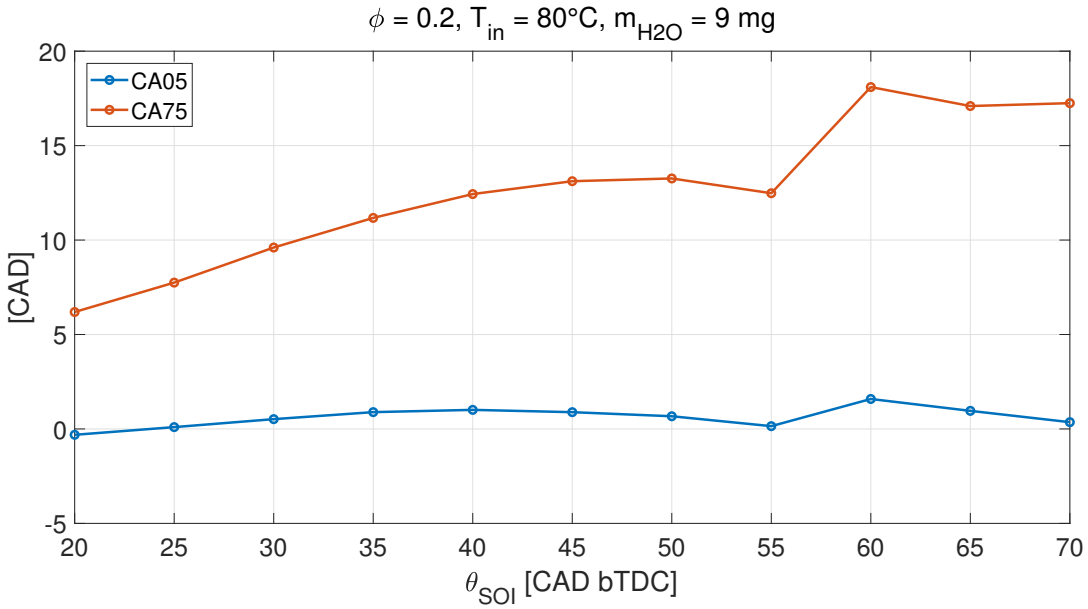

FIGURE 4.11: Impact of the crank angle of injection on the combustion duration.

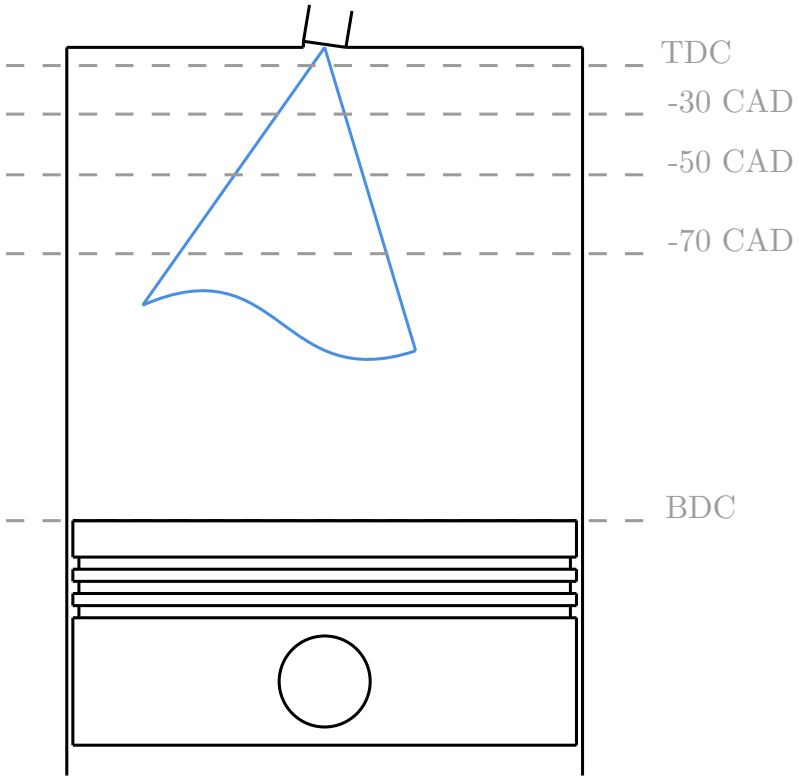

FIGURE 4.12: Piston positions with respect to crank angle.

4.3.3 Injection pressure

The injection pressure is defined as Δp, the difference between the water system pressure and the cylinder pressure when the injection starts. Comparisons have been made for different injection pressures : 20 bars, 70 bars and 120 bars. The equivalence ratio and the intake temperature have been kept constant. These three values have been chosen to cover as reliably as possible

the injection pressure range that had been calibrated. As it can be seen in Figure 4.13, a 20 bar injection has a less considerable effect on the HRR than the 70 and 120 bars injections. The sprays patterns shown in Figure 3.9 for these three different injection pressures confirm this result. The water spray of a 20 bars injection is shorter than for the two other cases. Figure 3.9 also shows that the water droplets become finer and finer when the injection pressure increases. However, between 70 and 30 CAD bTDC, the in-cylinder gas temperature typically lies between 450 and 750 K. Therefore, the water spray is immediately evaporated and the effect of the droplets size has to be kept in perspective. This could explain the resemblance between the 70 bars and the 120 bars injections.

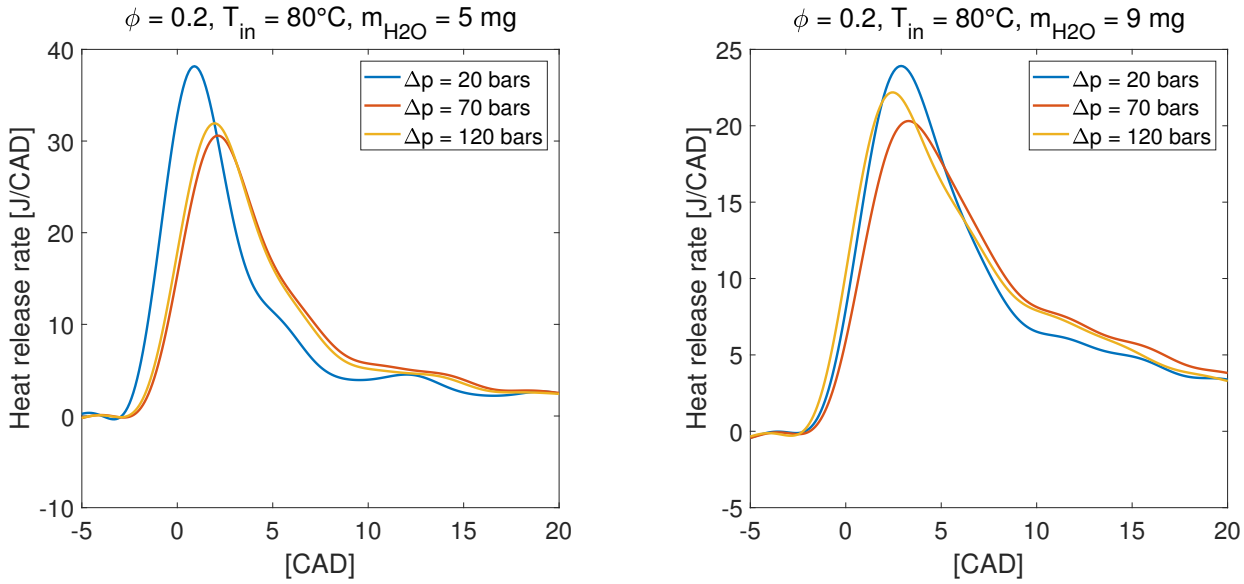

FIGURE 4.13: Impact of the pressure difference on the heat release.

For all that follows, the injection pressure has been fixed to 70 bars. This allows to empty less quickly the nitrogen bottle, and to analyze more in detail the influence of the other interesting parameters.

4.4 Stratification and combustion delay

As discussed earlier, the influence of WDI and intake temperature on the combustion timing is similar. However, they act quite differently. The intake temperature influences the ignition timing, and therefore modifies the burn duration by moving the combustion around TDC. On the other hand, WDI also delays the combustion by cooling the mixture, but at the same time stratifies the mixture, thus increasing the combustion duration. In order to know the importance of the thermal stratification occurring in the cylinder, it is needed to compare two different runs: one with WDI and one without WDI, but with the same CA05 as the previous one. As the ignition timing is the same for both runs, the longer duration of the second run is only due to the effect of WDI. However, this effect can be decoupled in two different phenoma: thermal stratification and dilution, as in EGR operations. This HRRs comparison is depicted in Figure 4.14, where CA05 and CA50 are marked with a diamond bullet and a round bullet, respectively.

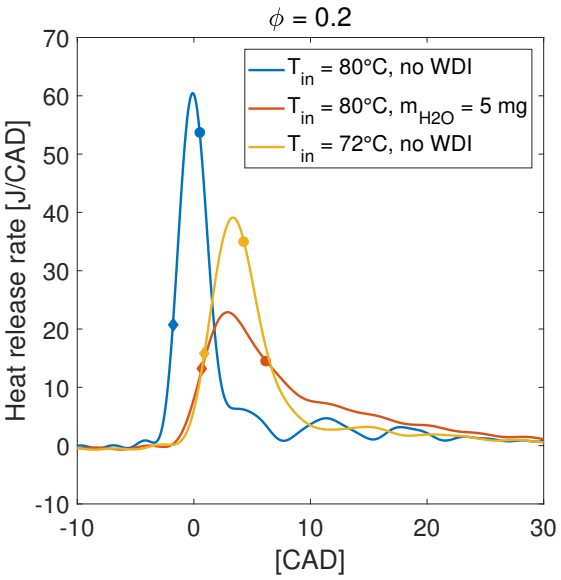

FIGURE 4.14: Heat release rate comparison between thermal stratification and combustion delay.

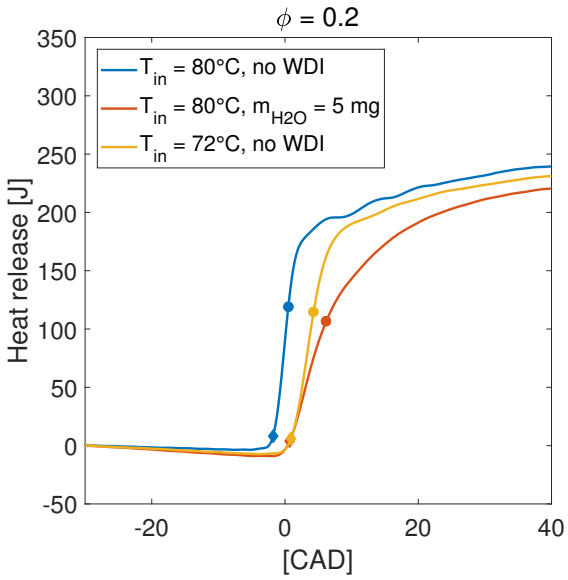

FIGURE 4.15: Heat release comparison between thermal stratification and combustion delay.

The comparison between those two ways of modifying the combustion timing is illustrated in Figure 4.16, where the CA_{75-05} is displayed as a function of the CA05, for the intake temperature sweep and for the injected mass sweep. One can observe that the increase in combustion duration with WDI is far more important than with a lower intake temperature for an equivalent ignition timing.

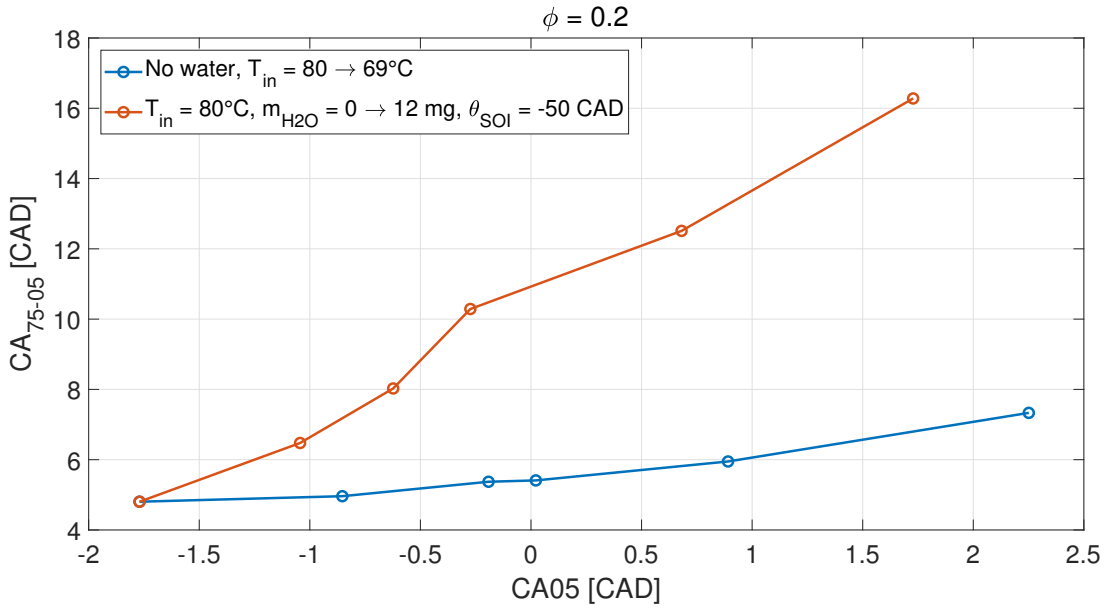

FIGURE 4.16: Combustion duration as a function of the start of combustion.

4.5 Increase of the power density

Now that the influence on the combustion of all controllable parameters has been investigated, it becomes possible to achieve the goal of this work : increasing HCCI power density. The base functioning point of the engine is displayed in Figures 4.17 and 4.18 by the blue curve, i.e. with $\phi = 0.2$, no WDI and an already high PRR. From this state, water has been injected to reduce the PRR, allowing for an increased fueling. To first reach an equivalence ratio of 0.3 for an acceptable PRR, 30 mg/cycle of water is needed (at 50 CAD bTDC). From this point, it has been necessary to use the double injection feature. Indeed, even if the injection duration continues to increase, the injected mass begins to saturate. So, for an equivalence ratio of 0.43, the injected water corresponds to two 18 mg injections (the first one at 75 CAD bTDC and the second one at 40 CAD bTDC). To finally reach an equivalence ratio of 0.5, two injections of 36 mg each have been used. From now on, 75 CAD bTDC and 40 CAD bTDC will be the fixed injection timings for every double injection experiment.

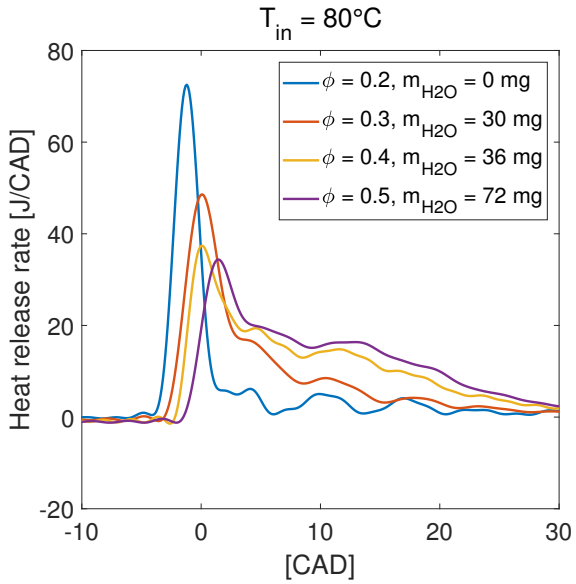

FIGURE 4.17: HRR curves for different values of the equivalence ratio.

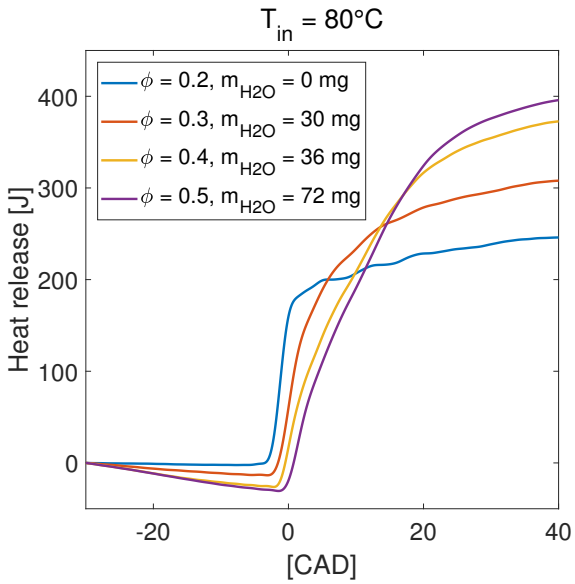

FIGURE 4.18: Gross heat release for different values of the equivalence ratio.

The combustion efficiency, η_{comb}, is the ratio between the total heat release and FuelMEP. This combustion efficiency decreases drastically when ϕ is increased from 0.2 to 0.3. This can be seen in Figures 4.20 (the top graph) and 4.18. The combustion efficiency then levels off when the fueling rate increases. One may expect a decrease of the combustion efficiency when a lot of water is injected. However, the evolution of η_{comb} presented in Figure 4.20 is not logical. Indeed, the stabilization for very high amounts of water remains unclear. Furthermore, those values of η_{comb} do not correspond to typical values of combustion efficiency. These values suggest that the combustion is incomplete while it is not the case. The following reasoning explains this inconsistency. The maximum value of $Q_{gross}(\theta)$ is needed to compute η_{comb}. Yet, this value is not reached in the 30 bTDC to 40 aTDC interval where the heat release is computed by the post-processing code. The computing algorithm is not taking that into account. This becomes even more critical for high fuel-air ratios (and therefore high values of injected water mass) because the slope of $Q_{gross}(\theta)$ at 40 CAD aTDC is more and more

significant. Therefore, the combustion efficiency presented in Figure 4.20 is not a good indicator. It is for the same reason that the CA_{75-05} combustion duration has been preferred to the CA_{90-10}.

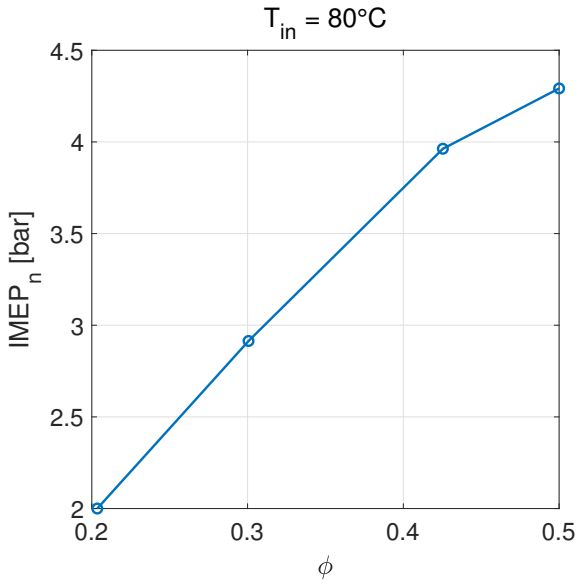

FIGURE 4.19: $IMEP_n$ for different values of the equivalence ratio.

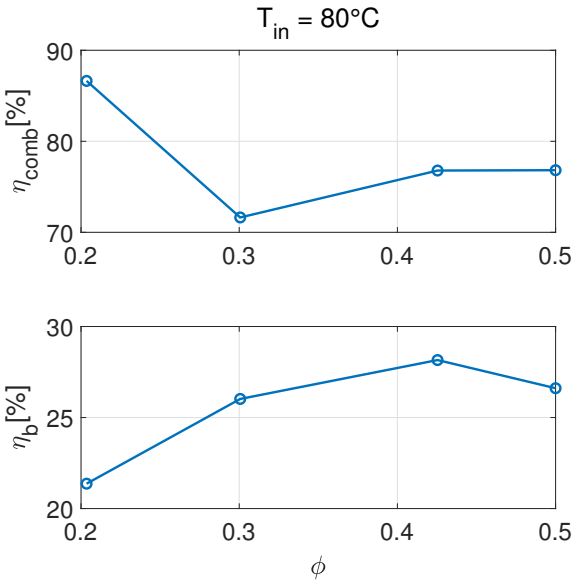

FIGURE 4.20: Combustion efficiency (top) and brake efficiency (bottom) for different values of the equivalence ratio.

Nevertheless, a 215% increase of the power density has been achieved, as shown in Figure 4.19. From an $IMEP_n$ of 2 bars without WDI, it has been possible to reach 4.3 bars. The $IMEP_n$ is computed as follows :

$$IMEP_n = \frac{\oint p \cdot dV}{V_c} \tag{4.1}$$

Therefore, the error in the computation of the total heat release has no impact on the value obtained for the $IMEP_n$. As expected, when the equivalence ratio is increased, more mechanical work is produced by the bulk gas on the piston. The evolution of η_b, shown in the bottom of Figure 4.20, confirms this tendency. Indeed, η_b is the ratio between BMEP and FuelMEP, while BMEP = $IMEP_n$ - FMEP. Throughout the load sweep, FMEP did not significantly change. It has been possible to increase the brake efficiency from 21% to 29% thanks to WDI.

Figures 4.21 and 4.22 clearly show the effect of WDI on the pressure rise rate. These results confirm the shape of the HRR curves. Combustion duration has been effectively increased, leading to a lowered MPRR. The equivalence ratio could have been even more increased given the quite low MPRR at $\phi = 0.5$. But the risk of entering a high ringing state due to a slight increase of the fueling rate has not been taken. Indeed, as it will be explained in section 4.5.2, HCCI combustion is pretty unstable, especially at high load.

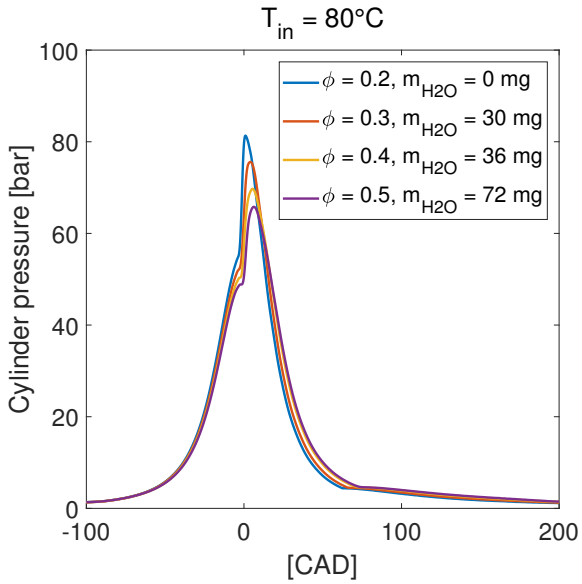

FIGURE 4.21: Cylinder pressure curves for different values of the equivalence ratio.

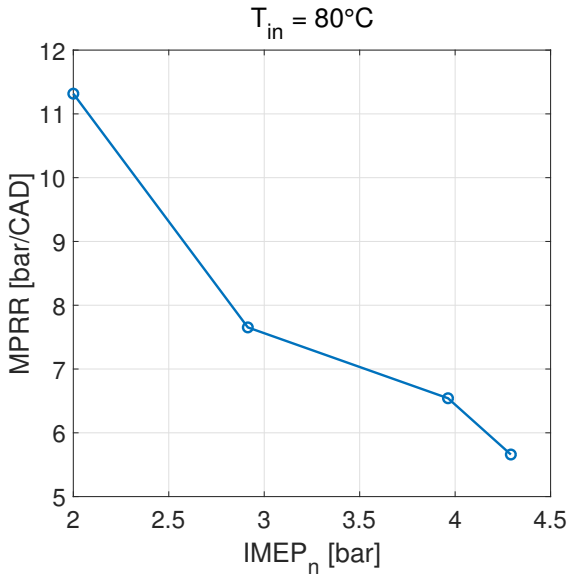

FIGURE 4.22: MPRR for the load sweep.

4.5.1 Limitations

As suggested by the decrease of the slope of the $IMEP_n$, the maximum work that can be obtained has a limit, even if the injected mass continues to increase. A first explanation comes from the combustion retard imputable to WDI, as shown in Figure 4.23. Indeed, as the combustion becomes more and more intense with the fuel-air equivalence ratio, the amount of water that needs to be injected to maintain an acceptable MPRR drastically increases. This will shift the combustion phasing further from TDC in the expansion stroke, reducing the maximum obtainable work.

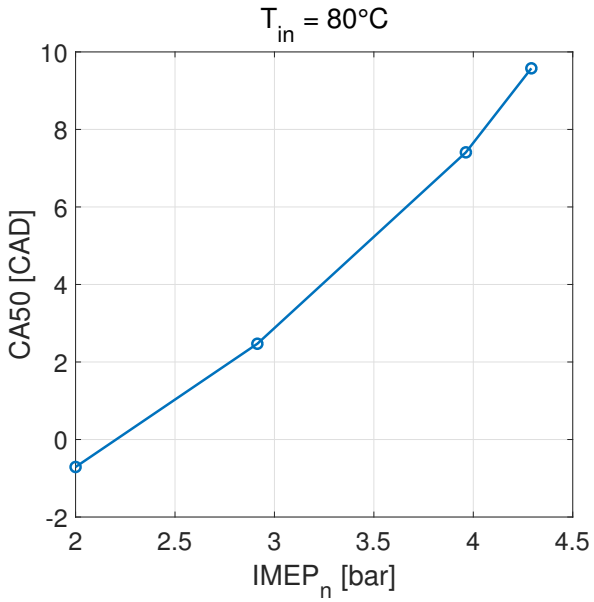

FIGURE 4.23: Evolution of the CA50 for the load sweep.

A more visual interpretation of the injected water mass corresponding to each point of the whole load sweep is given in Figure 4.24. As mentioned above, to reach an equivalence ratio of 0.5, and therefore an $IMEP_n$ of 4.3 bars, the injected mass has been increased to 72 mg/cycle. This is a huge leap in comparison with the previous points of the load sweep. Figure 4.25 shows that the burn duration begins to settle down despite the high amount of injected water, which suggests that the effect of thermal stratification is lessening. This may be explained by the fact that the injection zone is already cooled to a point where an additional amount of water would not lead to a significant decrease in temperature. However, the MPRR has continued to decrease. This can be explained by the combustion retard which, for its part, is still growing.

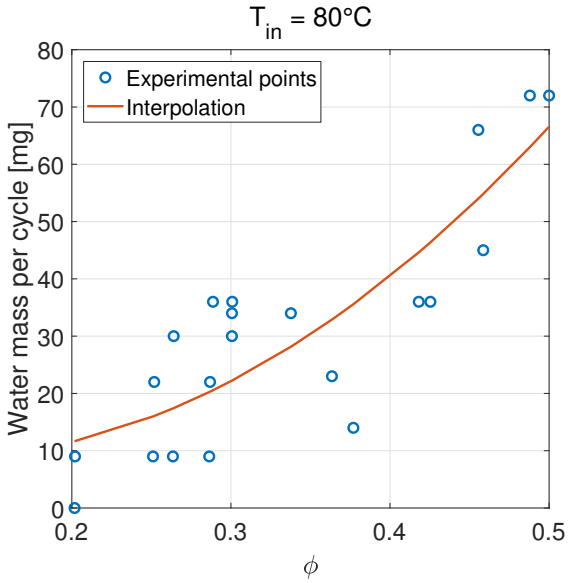

FIGURE 4.24: Mass of injected water for the load sweep.

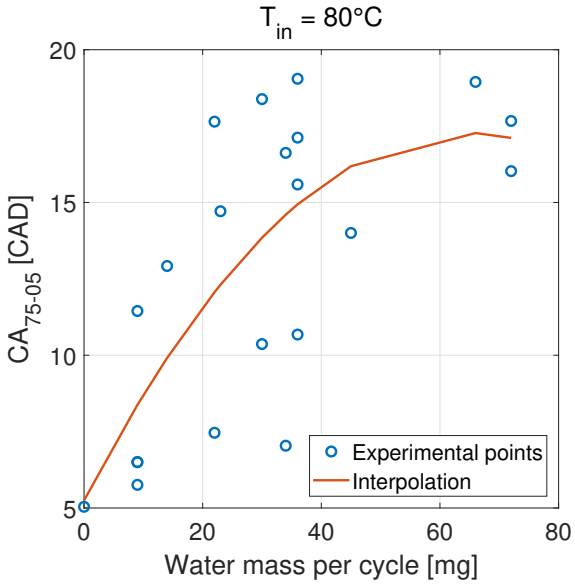

FIGURE 4.25: Combustion duration as a function of the water mass.

As explained in the beginning of this section, during this $IMEP_n$ increase phase, the equivalence ratio and the water amount were adapted one by one to reach acceptable functioning points. Therefore, equivalent-$IMEP_n$ operating points can be reached with different equivalence ratio - water amount pairs. It is for this reason that Figures 4.24 and 4.25 illustrate the whole data set of the load sweep instead of only a few points. Indeed, a four points set could have shown a totally different behaviour from the general tendency.

4.5.2 Influence of WDI on ringing

For all the runs of this load sweep, care has been taken to avoid crossing the ringing limit. But there was no direct indication on the ringing intensity, except the MPRR value displayed on the user interface, and the characteristic knocking noise. The equivalence ratio has therefore been progressively and cautiously increased. The ringing intensity has been computed for the points of the load sweep (corresponding to Figures 4.17 to 4.23), based on Eq. 1.9, and the result is displayed in Figure 4.26.

The concern of a possible ringing increase at high loads, despite high amounts of injected water and relatively low values of the MPRR, is thus confirmed. Indeed, the ringing intensity has shown an upward trend from an equivalence ratio of 0.3, although the MPRR has continued

to decrease. Therefore, the ringing phenomenon depends on several parameters and is rather unpredictable. This is why the load sweep has been stopped to an $IMEP_n$ of 4.3 bars.

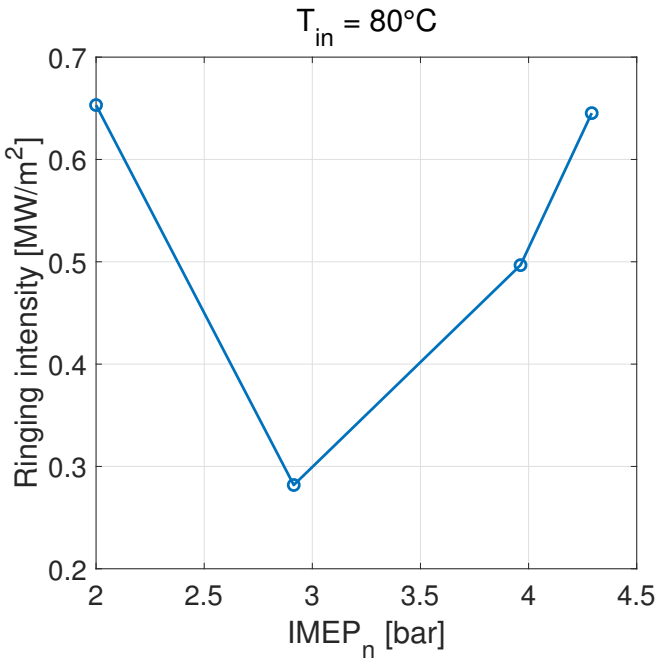

FIGURE 4.26: Ringing intensity for the load sweep.

The effect of WDI on the ringing intensity can however be highlighted. Figure 4.27 shows a comparison between the pressure curves of two cycles : one without WDI and one with a 9 mg injection. For all previous experimental results, the mean of the 100 cycles record was presented, but in this case, the goal is to show the pressure oscillations so only one cycle is displayed. WDI clearly reduces the MPRR, and the pressure waves have disappeared.

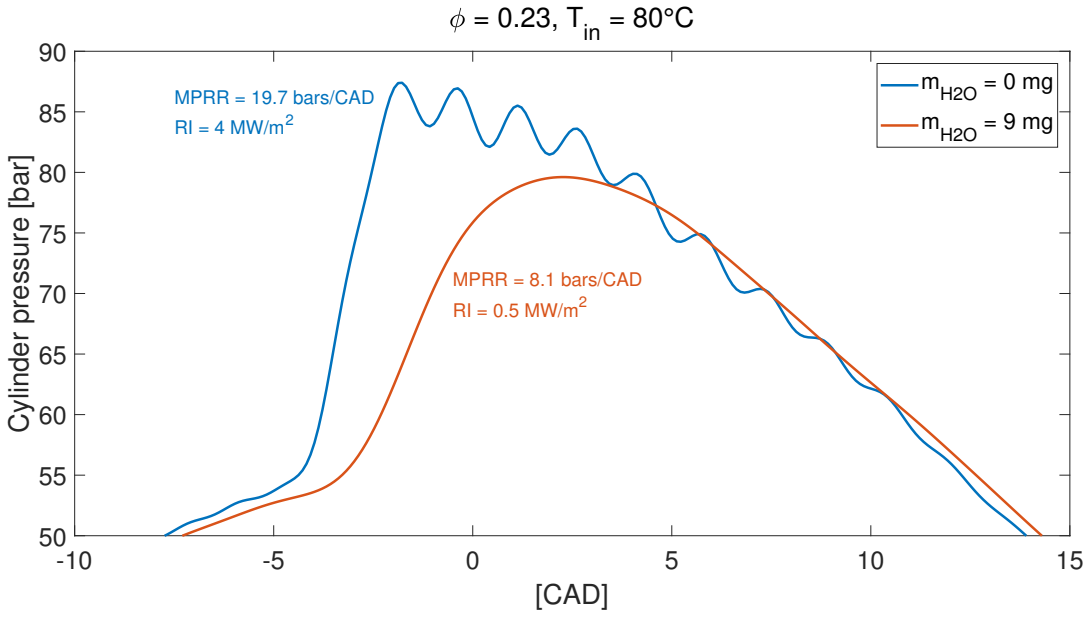

FIGURE 4.27: Effect of WDI on the the ringing intensity, at moderate load.

To conclude this section about the power density increase, the load limits with and without WDI are illustrated in Figure 4.28. The blue points show that the operating range of the HCCI engine without water direct injection is very limited. The MPRR reaches 19 bars/CAD for an $IMEP_n$ slightly above 2 bars. The red points represent the power densities that have been achieved thanks to WDI. The MPRR has been kept reasonable for $IMEP_n$ values up to 4.3 bars.

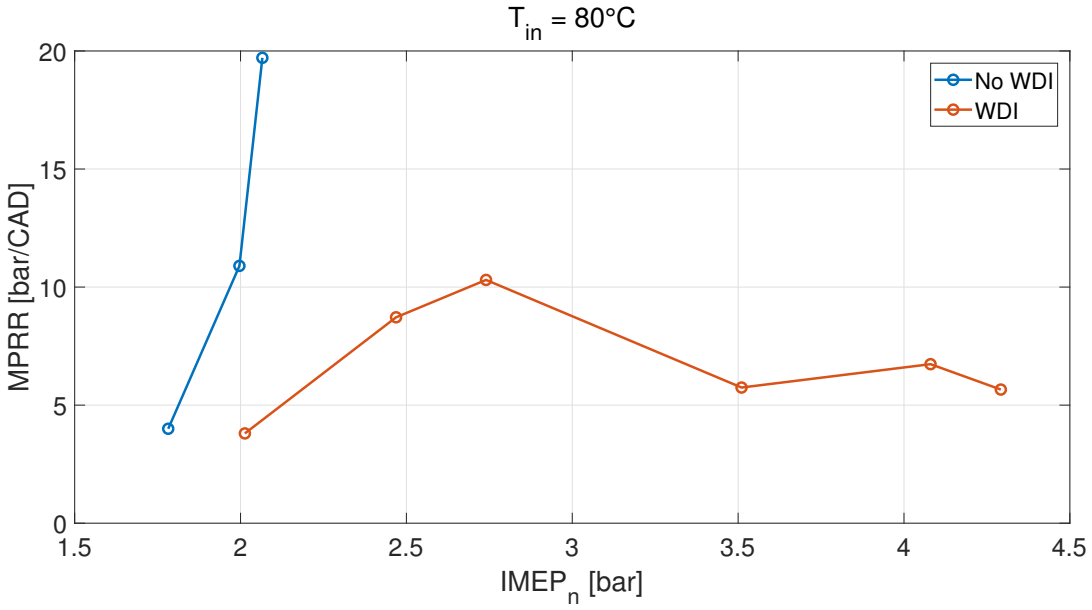

FIGURE 4.28: Effect of WDI on MPRR.

4.6 Formation of NO

With the increase in equivalence ratio, it could be tempting to expect an increase in NOx emissions. Figure 4.29 represents the evolution of NO emissions and the maximal cylinder temperature with respect to the equivalence ratio. Those data are represented with their 95% confidence interval. The maximal cylinder temperature never approaches the threshold for NOx formation and the NO proportion in exhaust gases remains negligible.

However, it should be highlighted that the cylinder temperature is computed from the cylinder pressure, which is homogeneous across the cylinder. The cylinder temperature presented in this section is thus an average value of the mixture temperature. Therefore, the maximum value of this cylinder temperature is not an accurate representation of the real maximum cylinder temperature with WDI because some zones are hotter than others. Despite this, it is a good indicator to have an idea of the situation.

The Tethys analyzer was calibrated to measure the proportion of NO and NO_2 in the exhaust gases. However, NO_2 measuring was rather imprecise and led to inexplicable major fluctuations between similar experiments, even when the Tethys was analyzing the ambient air. For this reason, only NO data are presented. Those NO_2 variations will be presented in section 4.7.2.

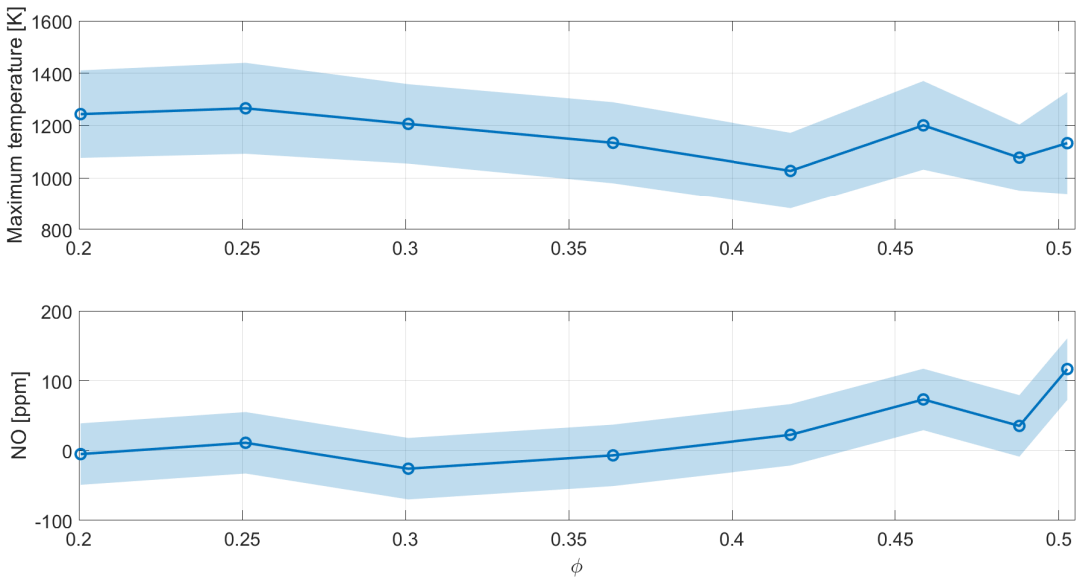

FIGURE 4.29: Maximal cylinder temperature and NO formation.

Figure 4.30 represents the 95% confidence interval of the maximal cylinder temperature for all the conducted experiments. Broadly speaking, the threshold for NOx formation is never reached. The only cases where the upper limit of the 95% confidence interval reaches the NOx formation zone occurred in the same set of experiments. After post-processing of this set, an abnormality was detected on the pressure measurements. The results of these experiments were not taken into account.

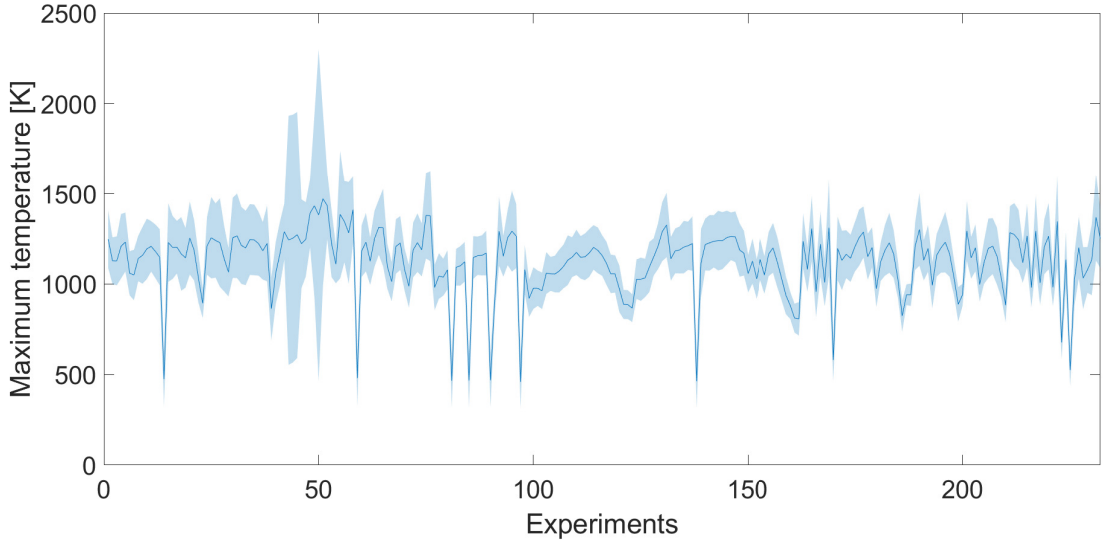

FIGURE 4.30: Maximal cylinder temperature.

4.7 Results uncertainties

This section gives an order of magnitude of the above results accuracy. First is presented the variability between the 100 cycles composing an experiment. Then are compared different experiments operated under the same conditions. No mention is made therein of the type-B uncertainty, i.e. the error due to the measuring devices calibration, the uncertainty of the sensors, etc. The reason is that the type-B uncertainty remains low compared to type-A uncertainty, i.e. the repeatability uncertainty, at least in absolute values. As an example, the cylinder pressure type-B uncertainty may reach high relative values, but only in zones where the cylinder pressure is low, e.g. during the admission and exhaust strokes. This is due to the fact that piezoelectric pressure sensors are rather unreliable for static measurements, as it was already mentioned in section 2.2.4. However, high accuracy measurements are not required in these low pressure zones.

4.7.1 Cycle-to-cycle variability

As explained in this chapter introduction, experiments consist in a record of 100 consecutive engines cycles. This results in low repeatability uncertainties. However, some experiments may demonstrate a different behaviour. It is depicted in Figure 4.31, where the 95% confidence interval of the cylinder pressure are shown for two different experiments. The blue curve is a classical low equivalence ratio without WDI experiment, while the orange curve is the experiment with an equivalence ratio of 0.5 leading to an IMEP of 4.3 bars. One can easily observe the larger variability of the high equivalence ratio experiment. Actually, this not the case for every WDI experiment, but only for high IMEP records. Indeed, in those cases, the injected amounts were so high that the water tank was emptying in minutes, so records had to be taken promptly. Therefore, the cylinder wall temperature could not be maintained at the constant temperature of 105°C and was slowly decreasing due to the cooling effect of WDI. Experiment records were then taken in transient state. This transient behaviour is illustrated in Figure 4.32 where the CA05 evolution is displayed for every cycle of the records.

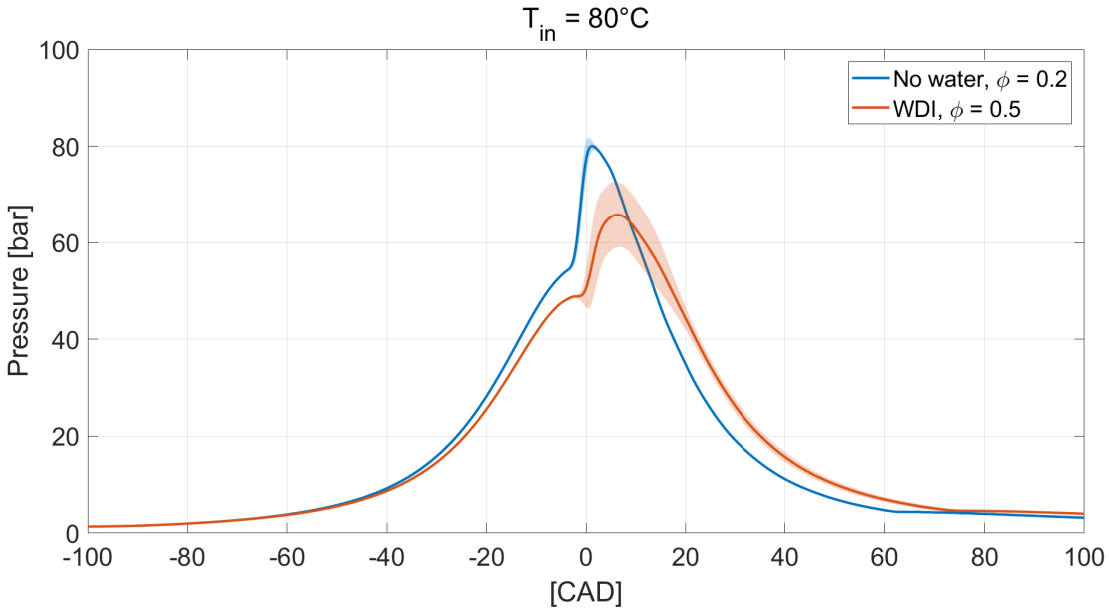

FIGURE 4.31: 95% confidence interval of the cylinder pressure.

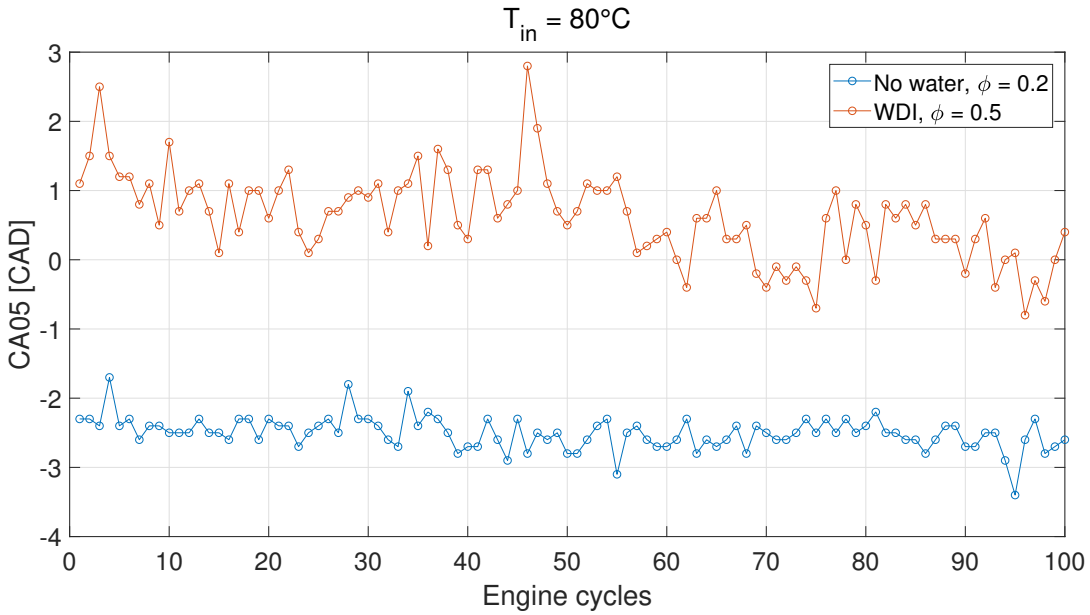

FIGURE 4.32: CA05 variability within 100-cycles records.

4.7.2 Variability among similar experiments

Although all secondary parameters, such as cylinder wall temperature and intake pressure, were kept constant, a certain variability was observable between similar experiments. Figure 4.33 shows the CA05 95% confidence interval for three different sets of data. Within each group, all the experiments were conducted under the same conditions. Data set A is characterized by the absence of WDI, while set B and C are experiments with water injections occurring at -50 CAD and -70 CAD respectively. It should be highlighted that the group C 95% confidence interval is only large due to the lack of experiments composing the group. Actually, the standard deviation of group A and C are similar.

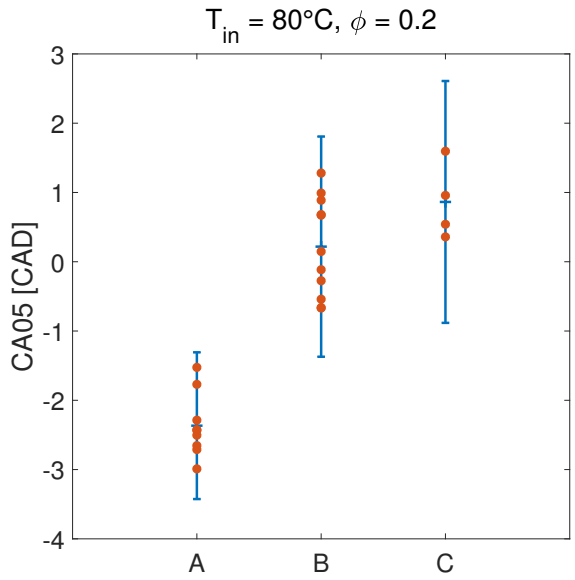

FIGURE 4.33: CA05 95% confidence interval for similar experiments: - **Data set A:** no WDI - **Data set B:** $m_{H2O} = 9$ mg, $\theta_{SOI} = -50$ CAD - **Data set C:** $m_{H2O} = 9$ mg, $\theta_{SOI} = -70$ CAD

As announced in section 4.6, NO_2 measurements are rather variable. Figure 4.34 represents this variability for three different sets of data. Data sets A and B are the same groups A and B from Figure 4.33, despite the fact that data set B contains less experiments here, because the Tethys gas analyzer was not connected for some experiments. From this figure, it can be understood why NO_2 measurements were not taken into account, although no major distinction can be observed between the different data groups.

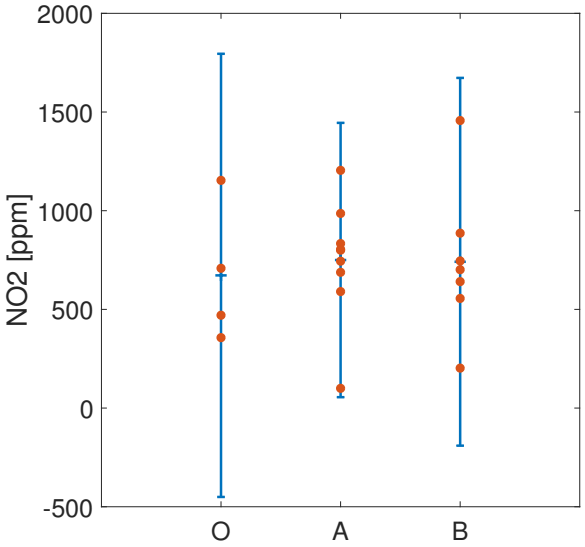

FIGURE 4.34: NO_2 95% confidence interval for similar experiments: - **Data set O:** Open air measurements - **Data set A:** no WDI - **Data set B:** $m_{H2O} = 9$ mg, $\theta_{SOI} = -50$ CAD

Conclusion

This master thesis unveils an innovating technique which aims to extend the upper load limit of the HCCI operating range : Water Direct Injection. In this context, a WDI system has been developed and integrated into the HCCI test bench. The experimental study has illustrated the potential of WDI on the engine performances.

The first chapter of this work presents in detail the advantages of HCCI engines which justify their interest in the frame of energy transition. Current limitations linked with HCCI combustion are also explained. Then, it is shown that the naturally occurring thermal stratification allows a lower pressure rise rate than what is expected by chemical-kinetics for a thermally uniform charge. WDI is thus introduced as a technique which tends to enhance this concept of thermal stratification.

The second chapter is divided in three parts. First, the methodology used to calibrate the injector is depicted. This step is required as no theoretical model enables to predict the injected water mass as a function of the user parameters. The HCCI test bench used for the experiments of this work is then described as well as the modifications which have been carried out on the cylinder head. The heat release computation algorithm is finally summarized. Third chapter displays the results of the aforementioned injector calibration and discusses the associated uncertainties.

The fourth and last chapter presents the experimental results that show the effect of WDI on HCCI combustion. The influence of the injected mass, the injection pressure and the crank angle of injection has been analyzed for a constant equivalence ratio. After this investigation at moderate load, the $IMEP_n$ has been increased while keeping acceptable values of the MPRR. The limitations on the power density that WDI enables to achieve are foreshadowed. Two hypotheses have been given to try to provide explanations about that phenomenon. However, the positive effect of WDI on the ringing intensity has been highlighted. Despite non-negligible levels of uncertainties, the potential of WDI for reducing pressure rise rates in HCCI combustion while maintaining the combustion phasing in a reasonable region has been confirmed.

The WDI system that has been designed as part of this work performs properly, and a 215% increase of the $IMEP_n$ has been validated. Therefore, the objectives of this thesis have been met, while at the same time offering interesting perspectives. Indeed, the effect of WDI could have been magnified with a side-mounted injector, or with a larger angle of injection. Furthermore, to have a deeper understanding of the thermal stratification created thanks to WDI, without investing in an expensive chemiluminescence setup, a post-processing methodology could be developed, inspired by the works of Lawler *et al.* [24].

Bibliography

[1] V. Dias. LELME2003 - Project in energy, slides on energy storage. Université Catholique de Louvain, 2017.

[2] François Boveroux and Amaury Gramme. Développement expérimental d'un moteur HCCI au gaz naturel. Master thesis in engineering science, under the supervision of Prof. Hervé Jeanmart, Université Catholique de Louvain, 2015.

[3] H. Jeanmart. LMECA2220 - Internal Combustion Engines. Université Catholique de Louvain, 2018.

[4] Adam B. Dempsey, Scott J. Curran, and Robert M. Wagner. A perspective on the range of gasoline compression ignition combustion strategies for high engine efficiency and low NOx and soot emissions : Effects of in-cylinder fuel stratification. *International Journal of Engine Research*, 2015.

[5] T. Kitamura, T. Ito, J. Senda, and H. Fujimoto. Mechanism of smokeless diesel combustion with oxygenated fuels based on the dependence of the equivalence ration and temperature on soot particle formation. *International Journal of Engine Research*, 2002.

[6] L. Kyeonghyeon, C. Seokwon, K. Namho, and M. Kyoungdoug. A study on combustion control and operating range expansion of gasoline HCCI. *Energy*, 2015.

[7] Hua Zhao. *HCCI and CAI engines for the automotive industry*. Woodhead Publishing Limited, Cambridge, England, 2007.

[8] Harisankar Bendu and S. Murugan. Homogeneous charge compression ignition (HCCI) combustion : Mixture preparation and control strategies in diesel engines. *Renewable and Sustainable Energy Reviews*, 2014.

[9] G. Haraldsson, P. Tunestål, B. Johansson, and J. Hyvönen. HCCI Closed-Loop Combustion Control Using Fast Thermal Management. *SAE Transactions, Journal of Engines*, 2004.

[10] Rudolf H. Stanglmaier, Thomas W. Ryan III, and Jason S. Souder. HCCI operation of a dual-fuel natural gas engine for improved fuel efficiency and ultra-low NOx emissions at low to moderate engine loads. *SAE technical paper series*, 2001.

[11] J. A. Eng. Characterization of Pressure Waves in HCCI Combustion. *SAE technical papers series*, 2002.

[12] Magnus Sjöberg, John E. Dec, and Nicholas P. Cernansky. Potential of Thermal Stratification and Combustion Retard for Reducing Pressure-Rise Rates in HCCI Engines, Based on Multi-Zone Modeling and Experiments. *SAE technical papers series*, 2005.

[13] Subir Bhaduri. Experimental Studies on HCCI Combustion of Biomass Syngas Towards Tar Tolerant Operation. Doctoral thesis in engineering science, under the supervision of Prof. Hervé Jeanmart, Université Catholique de Louvain, 2015.

[14] A.E. Lutz, R.J. Kee, and J.A. Miller. SENKIN: A FORTRAN program for predicting homogeneous gas phase chemical kinetics with sensitivity analysis. 1988.

[15] R.J. Kee, F.M. Rupley, E. Meeks, and J.A. Miller. CHEMKIN-III: A FORTRAN chemical kinetics package for the analysis of gas-phase chemical and plasma kinetics. 1996.

[16] Benjamin Lawler, James Szybist Derek Splitter, and Brian Kaul. Thermally stratified compression ignition: A new advanced low temperature combustion mode with load flexibility. *Applied Energy*, 2017.

[17] Robert Bosch GmbH. *Bosch Automotive Electrics and Automotive Electronics*. Springer Vieweg, 2014.

[18] Robert Bosch GmbH. *Gasoline direct injection: Key technology for greater efficiency and dynamics*. 2013.

[19] Richard P. Kennan and Gerald L. Pollack. Pressure dependence of the solubility of nitrogen, argon, krypton, and xenon in water. *American Institute of Physics*, 1990.

[20] Francesco Contino, Benjamin Berger, Fabrice Foucher, Jean-Baptiste Masurier, Subir Bhaduri, Anil Singh Pika, and Hervé Jeanmart. Analysis of a syngas HCCI engine for CHP biomass gasification facilities. In *The 11th International Conference on Combustion and Energy Utilization*, Coimbra, Portugal, 2012.

[21] Maxime Pochet, Ida Truedsson, Fabrice Foucher, Hervé Jeanmart, and Francesco Contino. Ammonia-Hydrogen Blends in Homogeneous-Charge Compression-Ignition Engine. *SAE technical papers series*, 2017.

[22] JCGM. Evaluation of measurement data — Guide to the expression of uncertainty in measurement. 2008.

[23] Stephen Busch and Paul C. Miles. Parametric study of injection rates with solenoid injectors in an injection quantity and rate measuring device. *Journal of Engineering for Gas Turbines and Power*, 2015.

[24] B. Lawler, M. Hoffman, Z. Filipi, O. Güralp, and P. Najt. Development of a Postprocessing Methodology for Studying Thermal Stratification in an HCCI Engine. *Journal of Engineering for Gas Turbines and Power*, 2012.

Appendix A

Test bench

A.1 Engine datasheet

Model	**L100V**
Engine Type	Air Cooled, 4 cycle, Vertical Cylinder
Fuel	Diesel
Number of Cylinders	1
Bore x Stroke	86mm x 75 mm
Combustion Type	Direct Injection
Total Displacement	435 cc
Aspiration	Natural Aspiration
Valves per Cylinder	2
Rated Speed	3600 rpm
Net Intermittent	9.1 Hp[6.8kW]/3600rpm
Net Continuous HP	8.3hp [6.2kW]/3600rpm
Direction of Rotation	Counter Clockwise, Viewed from PTO Side
Crankshaft Type	Straight Keyed, Tapered or Threaded
Starting System	Recoil or Recoil/12 V Electric
Decompression System	Manual Type with Auto-return Lever
Charging System	12 Volt, 15 Amps (for Electric Start Models)
Electric Stop Device	Optional, Fuel Stop Solenoid (for Electric Start Models)
Cold Start Aid	Optional, Intake Air Heater (for Electric Start Models)
Fuel Tank Capacity	4.7 liters
Brake Specific Fuel Consumption at Rated Output	279 g/kW-hr
Lubrication System	Pressure Lubrication with Trochoid Pump
Oil Capacity	1.60 Liters [0.60 Effective]
Exhaust System	Expansion Silencer with Cover
Air Cleaner	Dry-Type with Paper Element
Balancing System	Single, Counter-Rotating Balance Shaft
Length	16.2 in (412mm)
Width	18.6 in (472mm)
Height	19.4in (493mm)
Dry Weight (Recoil Start)	106.9 Lbs (48.5 kg)
Dry Weight (Electric Start)	117.9 Lbs (53.5 kg)
Noise Output @ Continuous Rating, Mean of Four Directions at 1 Meter	97 dB(A)

A.2 Test bench P&ID

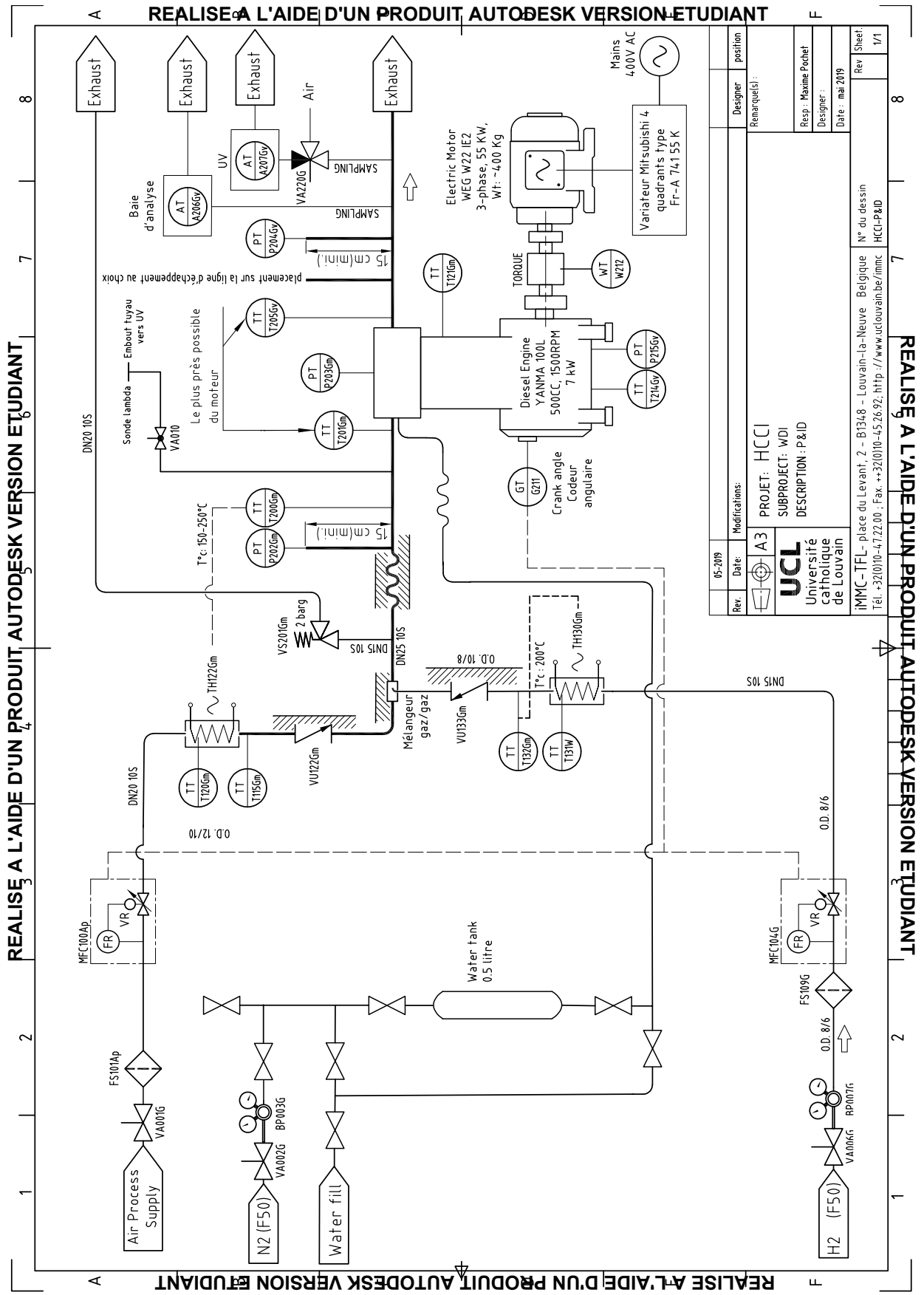

A.3 Technical drawing of the cylinder head modification

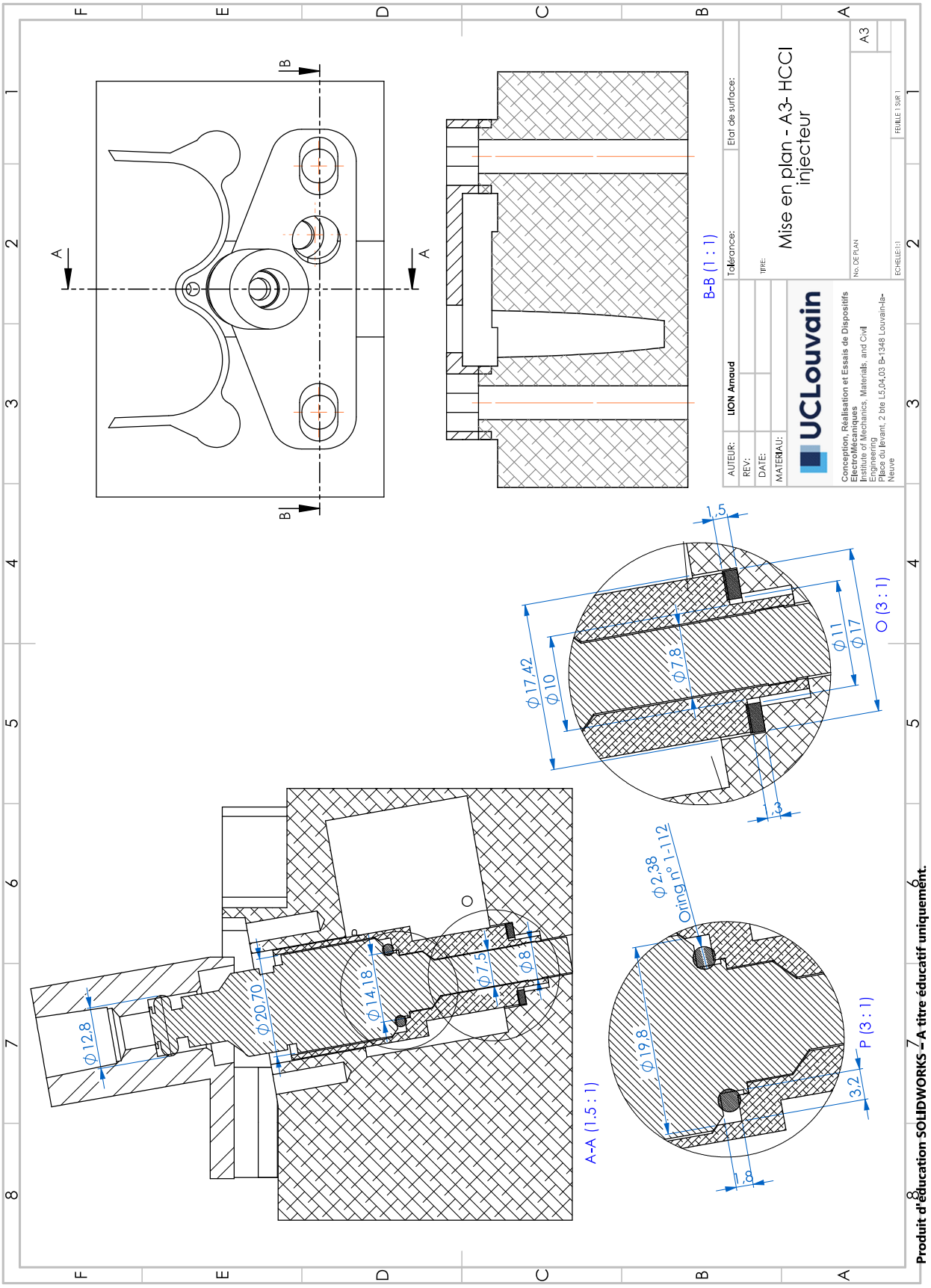

A.4 Labview user interface

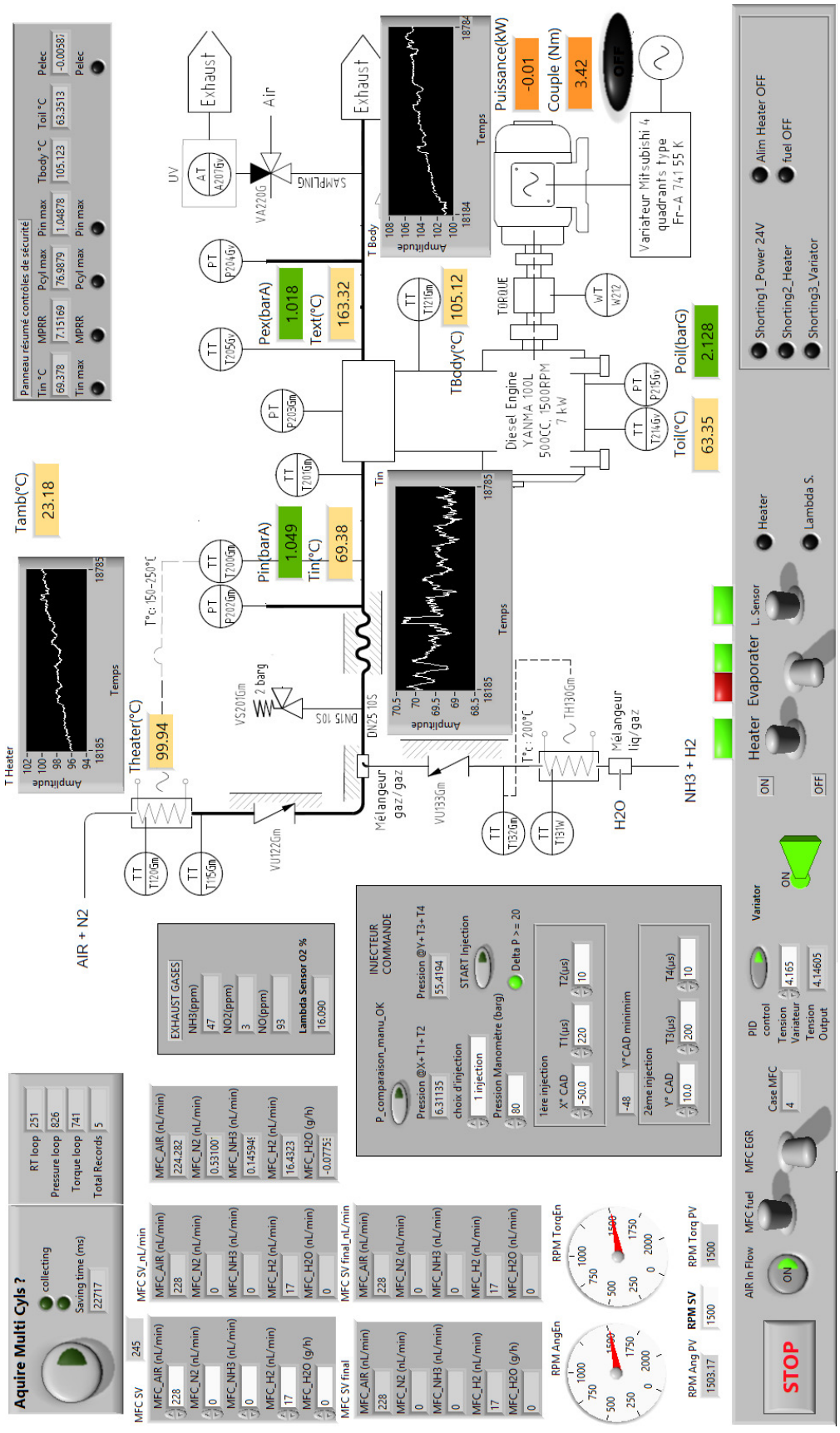

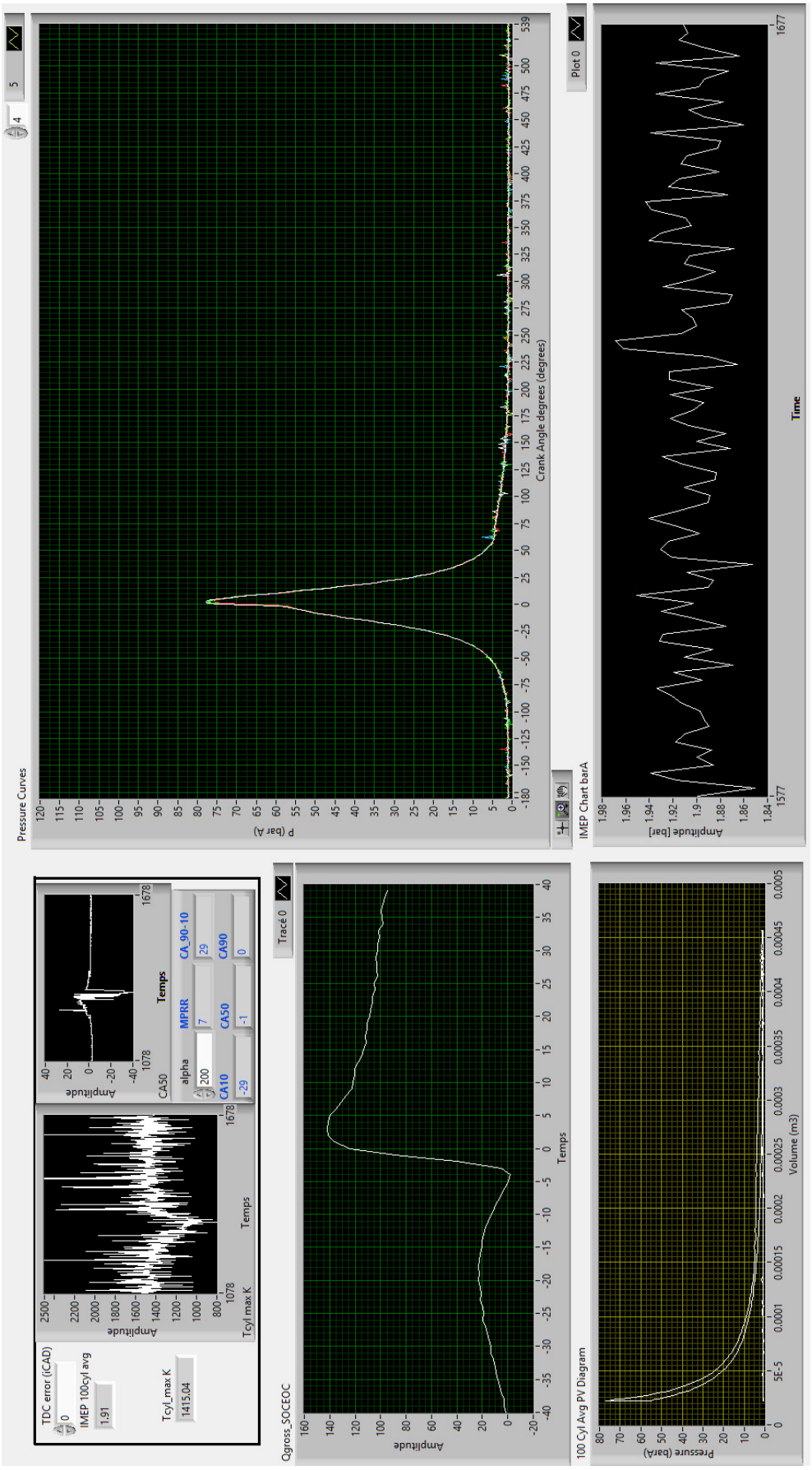
Pressure Curves
P (bar A)
Crank Angle degrees (degrees)
IMEP Chart barA
Plot 0
Amplitude [bar]
Time
TDC error (iCAD)
IMEP 100cyl avg
1.91
Tcyl_max K
1415.04
Amplitude
Tcyl max K
Temps
CA50
Temps
alpha
MPRR
CA_90-10
CA10
CA50
CA90
Qgross_SOCEOC
Trace 0
Amplitude
Temps
100 Cyl Avg PV Diagram
Pressure (bar A)
Volume (m3)

UNIVERSITÉ CATHOLIQUE DE LOUVAIN
École polytechnique de Louvain
Rue Archimède, 1 bte L6.11.01, 1348 Louvain-la-Neuve, Belgique | **www.uclouvain.be/epl**